Resonance Energy Transfer within and to optical Nanoparticles for Bioimaging and Biosensing Applications

Peremobowei Iyanu Diriwari

Normandie Université

UNIVERSITÉ DE ROUEN NORMANDIE

THÈSE

Pour obtenir le diplôme de doctorat

Spécialité **CHIMIE**

Préparée au sein de l'**Université de Rouen Normandie**

Resonance Energy Transfer within and to optical Nanoparticles for Bioimaging and Biosensing Applications

Présentée et soutenue par

PEREMOBOWEI IYANU DIRIWARI

Thèse soutenue le 28/03/2024

devant le jury composé de :

M. NIKO HILDEBRANDT	Professeur des Universités - Université de Rouen Normandie	Directeur de thèse
M. HASSAN OULYADI	Professeur des Universités - Université de Rouen Normandie	Président du jury
MME NATHALIE BERTHET	Maître de Conférences - Universite Grenoble Alpes	Membre du jury
M. THIBAULT GALLAVARDIN	Chargé de Recherche - Université de Rouen Normandie	Membre du jury
MME MARTA MARIA NATILE	Chargé de Recherche - PADOUE -UNIVERSITA DEGLI STUDI DI PADOVA	Membre du jury
M. LOIC CHARBONNIERE	Directeur de Recherche - Université de Strasbourg	Rapporteur du jury
M. OLIVIER MAURY	Directeur de Recherche - Ecole Normale Sup Lyon Ens de Lyon	Rapporteur du jury

Thèse dirigée par **NIKO HILDEBRANDT** (CHIMIE ORGANIQUE, BIOORGANIQUE, REACTIVITE, ANALYSE)

ED 508 NC Normande de Chimie

Laboratoire Cobra — Chimie organique, Bioorganique, Réactivité et Analyse.

Acknowledgement

I wish to extend my deepest gratitude to Prof. Niko Hildebrandt, my supervisor, for granting me the opportunity to delve into research within the esteemed nanoFRET group. Despite the geographical separation, Prof. Hildebrandt's unwavering availability and willingness to share his vast reservoir of knowledge and experience proved invaluable. His patient explanations of intricate concepts and unwavering encouragement instilled in me a resilient outlook on research, for which I am profoundly thankful.

I am equally indebted to my co-supervisor, Dr. Thibault Gallavardin, whose steadfast support and guidance, both within and outside the laboratory, were indispensable. Dr. Gallavardin's expertise in optical spectroscopy and gold nanomaterials greatly enriched my understanding and contributed significantly to the progress of my research.

Gratitude also extends to our collaborators, whose dedication and collaboration have already borne fruit in the form of a publication.

My sincere thanks go to Dr. Loïc Charbonniere and Dr. Olivier Maury for being the reviewers of my thesis and Prof. Hassan Oulyadi who has been my referent supervisor from the first year of this journey. Special thanks to Dr Nathalie Berthet and Dr. Maria Natile for accepting to be members of my thesis jury.

I am immensely grateful to both former and current members of the nanoFRET group for their invaluable support and expertise. I appreciate Dr. Mariia Dekaliuk, Dr. Laura Francés Soriano, Dr. Huijun Fu, Dr. Ruifang Su, Dr. Federico Pini, Dr. Carmen Gonzalez-Gracia, Dr. Anne Nsubuga, and Nour Fayad for their contributions, which have made my PhD journey truly memorable.

A heartfelt mention is reserved for my “friend and much more”, whose unwavering support has been a constant source of strength. Lastly, I extend profound appreciation to all those who have stood by me from the outset to the culmination of this endeavour – my brothers, friends and family. Your unwavering belief in me has been truly invaluable.

Not all heroes are sung, not all “lights” are seen. The entire wavelengths of light are not visible to us but we can always harness them for our use. Likewise, your potential may not be evident to all but your role is vital when properly harnessed. Stay consistent and let your “Light” shine.

P. Iyanu DIRIWARI

Table of Contents

Publications and Communications

List of Publications:

1. P. Iyanu Diriwari, N. Connor Payne, Thibault Gallavardin, Ralph Mazitschek and Niko Hildebrandt. Application of CoraFluor Tb complex in Lanthanide to Quantum Dot FRET Biosensing (in preparation)

2. L. Haye, P. I. Diriwari, A. Alhalabi, T. Gallavardin, A. Combes, A. S., Klymchenko, N. Hildebrandt, X. Le Guével, A. Reisch, Adv. Opt. Mater. 2023, 11, 2201474

Conferences and Posters

1. P. Iyanu Diriwari, N. Connor Payne, R. Mazitschek, and N. Hildebrandt. Lanthanide-to-quantum dot FRET bioassays with CoraFluor Tb Complexes. 21st ISBC & XIX ISLS, Gijon, Spain 30th May – 3rd June 2022. **Poster presentation**

2. P. Iyanu Diriwari, N. Connor Payne, R. Mazitschek, and N. Hildebrandt. Lanthanide-to-Quantum Dot FRET Bioassays with CoraFluor Tb Complexes. Journées Nord-Ouest Européenes Des Jeunes Chercheurs 9-10/06/2022 . **Oral presentation**

3. P. Iyanu Diriwari, N. Connor Payne, R. Mazitschek, and N. Hildebrandt. Evaluation of Time-Gated FRET Biosensing of Quantum Dot with CoraFluor Tb Complexes. Chemistry Summer School on f-elements, Aussois, France, 12-16/06/2022. **Poster presentation**

4. P. Iyanu Diriwari, N. Connor Payne, R. Mazitschek, and N. Hildebrandt. Lanthanide-to-Quantum Dot FRET Bioassays with CoraFluor Tb Complexes. Journée de l'Ecole Doctorale Normande de Chimie 23/06/2022 . **Poster presentation**

5. P. Iyanu Diriwari, N. Connor Payne, Thibault Gallavardin, Ralph Mazitschek and Niko Hildebrandt. Application of CoraFluor Tb complex in Lanthanide to Quantum Dot FRET Biosensing. 11th international conference on f-elements (ICFE-11), Strasbourg, France, 22-26/08/2023 **Oral Presentation**

List of Abbreviations

ACQ Aggregation caused quenching

AIE Aggregation induced emission

AuNC Gold nanocluster

AuNC-NP Polymer-encapsulated gold nanoclusters

AuNP Gold nanoparticle

CRF Corafluor

DDT dodecanthiol

EGFR Epidermal growth factor receptor

EI Edinburg Instruments

FRET Förster Resonance Energy Transfer

IC internal conversion

ISC Intersystem crossing

L4Tb Lumiphore Terbium complex

LLC Luminecent lanthanide complex

LMCT Ligand to metal charge transfer

LOD Limit of detection

LTC Luminescent Terbium complex

MCS Multichannel scalling

MLCT Metal to Ligand Charge Transfer

NSET Nano Surface Energy Transfer

PEMA Polyethylmethacrylate

PL Photoluminreescence

R_0 Förster radius

SPB Surface plasmon band

SPR surface plasmon resonance

SWIR Short wave infrared

TADF Thermally activated delayed fluorescence

TCSPC Time-correlated single-photon counting

TG Time-gating

VHH single-domain antibody

Dedicated to my dad, P. John DIRIWARI

……thank you for your love and sacrifice…..

Chapter One

1.0 Resonance Energy Transfer within and to Optical Nanoparticles for Bioimaging and Biosensing Applications

The development of fast and extra-sensitive diagnostic techniques is crucial in the early detection of diseases and point-of-care medicine. Hard-to-treat diseases, particularly cancer, if quickly detected, can be controlled before they get out of hand. In the case of highly infectious diseases such as the global coronavirus disease 2019 (COVID-19), early detection helped isolate infected patients and curb the further spread of the disease. Developing such diagnostic tools requires the detection of biomarkers specific to the disease. A biomarker is a chemical compound (usually a protein, metabolites or nucleic acid) present in the blood, urea, saliva, cerebrospinal fluid, sweat and so on, at certain concentration limits in certain disease conditions.[1–3] Conventional diagnostic analyses in the laboratory can be complicated, requiring bulky instrumentation and being time-consuming; thus, they are not very practical in point-of-care medicine. Therefore, quickly detecting the biomarker at minute concentration improves early diagnosis and point-of-care treatment.[4,5] Since M. Cremer first demonstrated the concept of electrochemical sensing in 1906, biosensors have become ubiquitous as there have been numerous studies and advancements in applying biosensors in different diseases and toxin detection.[6–9] A biosensor is a device that measures biological responses by producing signals proportional to the concentration of the analytes in the reaction. A typical biosensor consists of the analyte (the substance of interest to be detected), the bioreceptor (a molecule usually of biological origin which specifically recognises the analyte), the transducer (converts one form of energy to another as signal), the electronics (that amplifies and processes the signal into digital form) and the display (which shows the signal in printable numeric, graphic, tabular form or image).[7,8] The different types of sensors are categorised according to their signal transduction, receptors and general function. The first ‘true’ biosensor was an electrochemical-

transduction-based oxygen biosensor invented by Leland C. Clark, Jr in 1956, which laid the foundations for Clark and Lyons to develop the glucose sensor in 1962. Optical, magnetic, thermoelectric and calorimetric are other categories of biosensors of interest.[8,10–13] Optical-based biosensors are particularly interesting because they make molecular analyses more rapid, sensitive and convenient. Optical-based biosensors are further sub-classified into colourimetry, fluorescence, phosphorescence, reflection, refraction, dispersion, Raman scattering, infrared absorption, chemiluminescence and surface plasmon resonance biosensors, of which the fluorescence biosensors are the most exploited of recent. Medical diagnostics, drug discovery and delivery, environmental monitoring and food safety are examples of possible applications of Fluorescence-based biosensing. An advantage of fluorescence biosensors is the possibility to explore many parameters, such as fluorescence intensity, anisotropy, lifetime, quenching efficiency, and quantum yield.[14]

The intrinsic fluorescence properties (called autofluorescence) of biomolecules (such as proteins, Flavins, NAD^+, nucleotides), which change upon interaction with other ligands or molecules, make detecting these analytes by fluorescence technique possible. Researchers label non-fluorescing analytes with fluorophores via different conjugation methods to study them. A fluorophore is a general term used to describe compounds that emit light after excitation. It is often necessary to examine one analyte in the presence of other fluorescing biomolecules; thus, researchers use fluorescence probes with excitation and emission wavelengths different from the autofluorescence. However, the downside to autofluorescence is that it is often brighter than the desired fluorophore signal intensity. Therefore, measuring and subtracting the signal of a non-labelled autofluorescence control is necessary while carrying out traditional fluorescence studies. The native fluorescence decay time of biomolecules, which decays faster than the luminescence of probes used in fluorescence biosensors, provides the avenue to apply time-

gating to eliminate fast-decaying autofluorescence signals, thus eliminating the extra step of subtracting autofluorescence signal.[15–18] Time gating is a technique where the detector can only start recording the luminescence decay after the decay of the excitation pulse and background signal. It employs the use of fluorophores with a long luminescence lifetime. We can observe the luminescence lifetime after cutting off the background signal. An example of such a fluorophore is the Corafluor Tb complex (CRF) used in this study. CRF is a new family of Tb complexes with desireable photophysical properties for biological studies [19–22].

Bioimaging, just like biosensing, is vital in medical diagnosis and disease management. Bioimaging generally refers to using non-invasive methods to observe biological processes at the cellular and molecular level within living cells, tissues and fixed intact specimens in real-time. It uses light, fluorescence, ultrasound, X-rays, magnetic resonance and positrons as energy sources for imaging. Many clinical imaging techniques like MRI (magnetic resonance imaging), OCT (optical coherence tomography), and computed tomography use the entire energy spectrum for multi-modal imaging. Multi-modal imaging combines two or more imaging methods within a single examination setup. For instance, MRI and fluorescence microscopy detected the uptake of Cy5.5-SPIO-chlorotoxin, a multi-modal nanoprobe, by glioma cells in brain tumours.[23–26] Fluorescence microscopy and macroscopy are sub-classes of optical bioimaging that involve using genetically encoded fluorescent reporters or fluorophores to facilitate the visualisation of molecular events in living cells. During tumour removal, fluorescence imaging helps to distinguish tumour cells from healthy cells. A significant advantage of fluorescence optical imaging is the possibility of multiplexing. [24] The literature review chapter of this thesis discusses the concept of multiplexing in biosensing and bioimaging. Another benefit of fluorescence optical imaging is using low-energy photons that are safer for living organisms than high-energy gamma rays detected by PET (positron electron

tomography). With a cheap and easy charge-coupled device (CCD) camera setup and a filtered light source, optical fluorescence imaging can reach unprecedented sensitivities and detect sub-nanomolar concentrations.[24,27] However, absorption and autofluorescence of biomolecules, shallow light penetration in tissues, light scattering of biological materials and water absorption are some of the limitations of fluorescence bioimaging. Researchers in the past decades have developed various means of tackling these limitations. For example, autofluorescence in fluorescence microscopy, similar to biosensing, can be reduced by time-gating or setting suitable excitation and emission wavelengths where interfering intrinsic fluorescence can be avoided.[28] Understanding the biological optical window helps choose the appropriate excitation and emission wavelength for bioimaging applications. Bioimaging in the near-infrared-II (NIR-II) window (900-1700 nm) is preferred for living organisms, as there is deeper tissue penetration due to less light scattering. High-resolution images at μm depths are possible due to the negligible autofluorescence and, by implication, a high signal-to-noise ratio in the region. Excitation in the NIR window is generally more tolerable for living organisms than ultraviolet light, which damages the cells and visible light that cannot penetrate the tissues effectively.[29–31]

Optically active nanomaterials have greatly improved the speed, resolution and sensitivity of fluorescence-based bioanalysis over the years.[32] Optically active nanomaterials are materials between 1-100 nm in size and can exude specific characteristics when they interact with light. These materials can absorb, emit, quench or convert light into other forms of energy like heat. Fluorescent nanomaterials like quantum dots (QD) have vast applications in biosensing and bioimaging studies[33–38] The discovery and synthesis of QD earned Moungi G. Bawedi, Louis E. Brus and Aleksey Yekimov the 2023 Nobel Prize in Chemistry.[39] The brightness, photostability and monochrome emission of QD make them valuable for biosensing and

bioimaging applications. On the other hand, photothermal therapy and bioimaging are significant applications of gold nanoparticles (AuNPs). They have been widely applied for their unique plasmonic properties rather than fluorescence properties, as the plasmon effect in AuNPs helps improve biosensor sensitivity. Hybrid AuNPs are attractive for fluorescence bio-imaging due to their high brightness level and resistance to photobleaching.[40–43] Nanomaterials are generally more photostable than organic fluorophores. Incorporating nanomaterials into fluorescent biosensors increases the biosensor's sensitivity due to the increased specific surface area for ligand-receptor interaction. Various biosensing methods have been combined with optically active nanomaterials to test biological substances. Nanoscale proximities expose nanomaterials to near- and far-field interactions in energy transfer processes. [44–47]

Förster Resonance Energy Transfer (FRET) is one of the possible relaxation processes of an excited fluorophore. FRET is a physical process where an excited energy donor transfers non-radiative energy to a ground state acceptor by long-range dipole-dipole coupling. The resonance condition is met when the donor emission and acceptor absorption spectra overlap. When an atom or molecule interacts with light at high enough frequencies, its electrons populate the excited state and then relax back to the ground state. The relaxation process can be radiative or non-radiative. The radiative relaxation process occurs when the energy of the electronic transition is converted into light upon relaxation, and the non-radiative process occurs when the energy is dissipated to the surroundings or transferred to nearby atoms that can be excited by this energy. These nearby acceptor atoms are said to resonate with the relaxing energy donor, hence the resonance in FRET. Though FRET depends on the donor-acceptor distance to the sixth power, applying large nanoparticles like AuNP can reduce this distance dependence to the fourth power, thereby increasing the energy transfer range. This phenomenon is not called FRET but is instead referred to as nano-surface energy transfer, NSET. Excited donor atoms

can also exchange electrons with surrounding atoms by Dexter interaction. FRET, especially with luminescent lanthanides and nanoparticles, provides unprecedented resolutions and sensitivity when applied in bioimaging and biosensing, hence the interest of this study.[48–51]

1.1 Thesis Objective

My thesis aims first to study energy transfer within gold nanocluster (AuNC) loaded polymer nanoparticles (AuNC-NPs) developed for bioimaging applications in the NIR-II window. Then, characterise CRF and apply it as a donor in FRET to optical nanoparticles (AuNP and QD) for biosensing applications

First, I carried out the spectroscopic analysis of AuNC-NPs designed to enhance NIR-II luminescence for bioimaging. Xavier Le Guével (IAB Grenoble) synthesised the AuNCs and applied the AuNC-NPs in imaging. Andreas Reisch (Universite de Strasbourg) characterised the NP formation and size. As reported in Chapter 3 of this work, the unique behaviour of the luminescence of the NPs necessitated an inquiry into the suspected energy transfer phenomenon. In this study, I could point out the origin of the two luminescence lifetimes reported for AuNCs and then hypothesise the homo-FRET or metal to ligand charge transfer (MLCT) as the energy transfer mechanism.

My second objective is to study and apply a new Tb complex (Corafluor Tb, CRF) in time-gated FRET to NPs (QD and AuNP) for biosensing applications reported in Chapter 4. As few affordable commercial Tb complex options suitable for biosensing and bioimaging applications exist, it was necessary to carry out a photophysical characterisation and biosensing application of CRF. The absorption, emission, lifetimes, quantum yields, and photostability of CRF were studied in several buffers and under different conditions for several days. The Tb complexes were conjugated and applied in QD and AuNP biosensing via streptavidin-biotin interaction.

Finally, I used CRF in biosensing the epidermal growth factor receptors EGFR, a biomarker implicated in many kinds of cancer.

Chapter Two

2.0 Bioimaging in the SWIR Region

Though extensively developed over the years, applying fluorescence techniques in non-invasive optical imaging can be challenging. Light scattering, absorption and autofluorescence limit high spatiotemporal resolutions, high contrast and deep tissue penetration, which are essential for quality optical imaging. Recently, there has been a growing interest in fluorescence imaging in the second biological window. The second biological window, also known as the NIR-II or short-wave infrared (SWIR), spans 1000 – 1700 nm wavelengths. Fluorescence imaging in the SWIR window opens new frontiers in biomedical studies as it breaks the limitations of imaging in the ultraviolet-visible (UV-Vis) region of the spectrum (190-700 nm), and it stretches the advantages of the NIR-I (700-900 nm) imaging.[52–54]

There has been significant progress in the development of SWIR windows for biomedical studies since the ground-breaking works of Hongjie Dai's team in the early 2010s.[55–58] The considerable advances in indium–gallium–arsenide (InGaAs) camera technology and associated optics enabled the development of very sensitive and affordable detection systems between 900 nm and 2100 nm with efficient thermoelectric cooling systems to reduce thermal noise.[59] Several bright SWIR probes of organic and inorganic materials further facilitate the current SWIR imaging advances.[54,60,61] Imaging processing and reconstruction based on Monte Carlo restoration of SWIR images are used to enhance the spatial resolution of the image by 59% and the contrast by one order of magnitude.[54]

The set-up for in-vivo fluorescence imaging requires the assembly of image-forming optics in between an excitation light source and an emission light detector to generate a visual representation of the imaged object based on the spatiotemporal distribution of fluorescent

labels, which are either exogenously introduced or endogenously expressed to give contrast to anatomical structures, biological molecules and physiological functions (Figure 2.0).

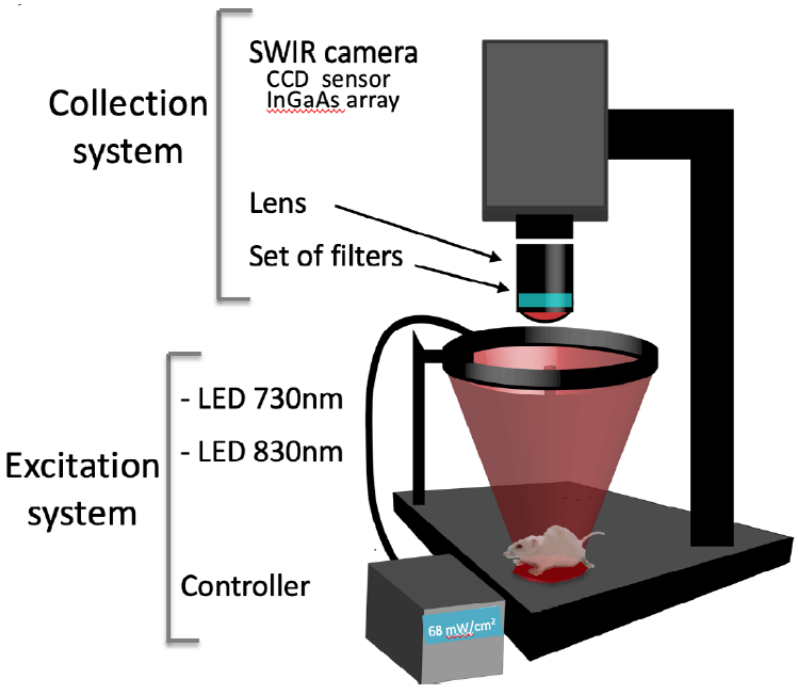

Figure 2.0 Schematic side view of SWIR imaging set-up for artificial and in vivo models.[54]

These fluorescent labels are distributed in three dimensions in biological tissues. The third dimension, the depth, can range from a few millimetres to tens of centimetres in experimental animals and human subjects. Therefore, for the excitation light to reach each fluorescent label and excite it and for the emitted light from each fluorescent label to reach the detector to be collected for image formation, both excitation and emission photons need to travel extensively through biological tissue, where the interactions between these photons and the surrounding biological environment become increasingly crucial at greater depths. The photon travel through biological tissues is affected by four factors related to light–tissue interactions: interface reflection of the excitation light, in-tissue scattering of excitation and emission photons, in-tissue absorption and tissue autofluorescence (Figure. 2.1a).[30]

2.1 Challenges of Photon Interference in SWIR Imaging

2.1.1 Interface Reflection

From the onset of the measurement, the monochromatic excitation light undergoes interface reflection, which reduces the number of photons that get through the tissue surface. Interface reflection occurs when a substantial part of incoming monochromatic excitation light is reflected into the air as it touches the object's surface. It depends on the incidence angle of the excitation light and the difference in the refractive index between air and the object's surface. Still, it is independent of the wavelength of the light. Usually, the interface reflection does not cause a loss of signal or image distortion if the surface roughness and curvature are smaller than those of the image of interest. When the surface roughness and curvature are too high, it could also lead to randomised reflections of the fluorescence emission at the interface. However, this can be managed by applying a refractive-index-matching medium. High-resolution in vivo brain and eye imaging applies such a matching medium.

2.1.2 Photon Scattering

The second limitation of fluorescence imaging is the scattering of both the excitation and emission photons. Animal tissues have different components (lipid membranes, subcellular organelles and water) with varying refractive indexes that cause photons to scatter and pass from one medium to another in-through or out-through the tissue. The scattering effect limits how deep excitation photons can get into the tissue and the image's resolution generated from the fluorescent label's emission photons. For most biological tissues, the degree of scattering follows an inversely proportional relationship with the wavelength of the photons (Figure 2.1b). Hence, with reduced scattering at longer wavelengths (NIR/SWIR regions), photon penetration into the tissues is deeper.

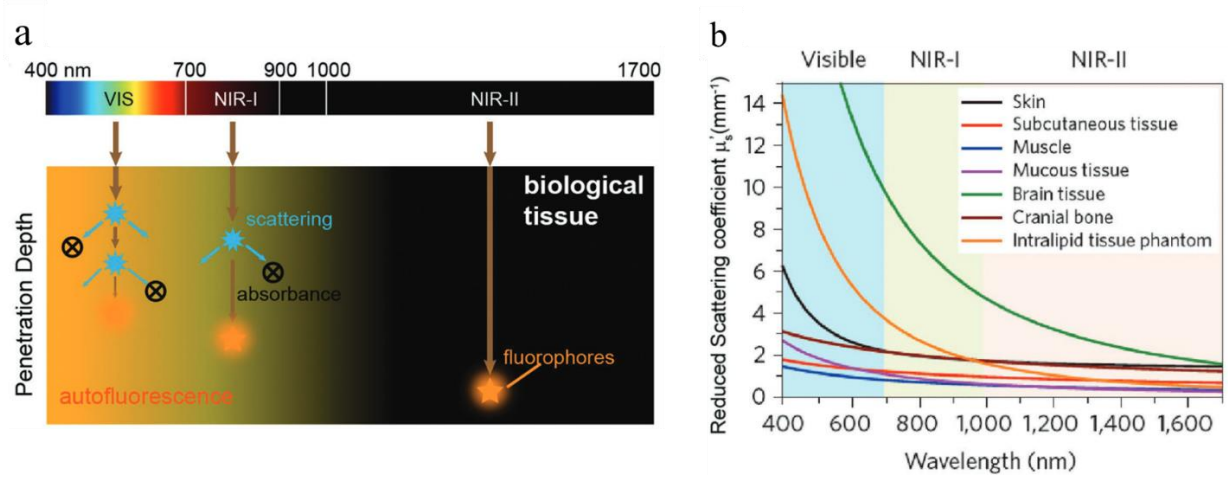

Figure 2.1 (a) Schematic of tissue penetration depth, absorption, autofluorescence, and scattering of light with different wavelengths. (b) Reduced scattering coefficients of different biological tissues and of intralipid tissue phantom. Reproduced with permission.[30] Copyright 2017, Nature Publishing Group.[62]

Reduced scattering at longer wavelengths also reduces the background signals generated from scattered emission photons, thereby improving the spatiotemporal resolutions of images observed at the SWIR region. A study on the impact of light-scattering effects on spatial resolution in different SWIR sub-regions reported an even more significant reduction of scattering from endogenous tissues at longer wavelengths in the SWIR window. The study analysed two SWIR emissive phantoms made of polydimethylsiloxane (PDMS)-gold nanoclusters (AuNCs) composite covered with mice skin or capillary tubes filled with Au NCs or IRDye 800CW at different depths in intralipids and finally AuNCs intravenously administered in mice.[54] A phantom (orange line in Figure 2.1b) is an object designed to mimic the properties of animal tissue when developing or studying new medical imaging options. The most commonly used phantoms are liquid tissue, solid silicone or polymer, gelatine/agarose, and animal phantoms.[63] The scattering optimisation study used a liquid phantom made of a capillary tube containing the AuNCs of IRDye 800CW, which was immersed in a 2% intralipid solution at increasing depths between 1 and 8 mm and solid silicone composite of AuNCs-PDMS. The study highlighted the need to develop fluorescent labels with strong brightness in the SWIR window that can be exited in the NIR region.[54]

2.1.3 Photon Absorption

The third limitation of fluorescence imaging is in tissue absorption. Many biological molecules that are present in biological tissues are chromophores. These chromophores can absorb and convert excitation and fluorescence emission photons into heat dissipation. A typical class of such chromophores in vertebrates are haemoglobins, responsible for the transportation of oxygen in blood circulation through the chromophoric - heme groups. Despite the difference in absorption spectra of oxygenated and deoxygenated haemoglobins, they both significantly contribute to the light absorption of human blood in the <600 nm range, which gives blood its red colour (Figure 2.2a). Several other biomolecular chromophores that absorb UV-Vis light include aromatic amino acids, reduced nicotinamide adenine dinucleotide (NADH), and heterocyclic flavins.[49] Liquid water, an essential component of all animal cells and tissues, has some vibrational overtone bands in the NIR regions: 970 nm, 1250 nm, 1450 nm and beyond 1800 nm (Figure 2.2b)[64,65]. Considering all the wavelengths of all biological chromophores, the entire 700-1700 nm spectral region (besides the narrow 1450 nm water absorption band) is suitable for deep-tissue imaging with low absorption and scattering of excitation and emission photons.

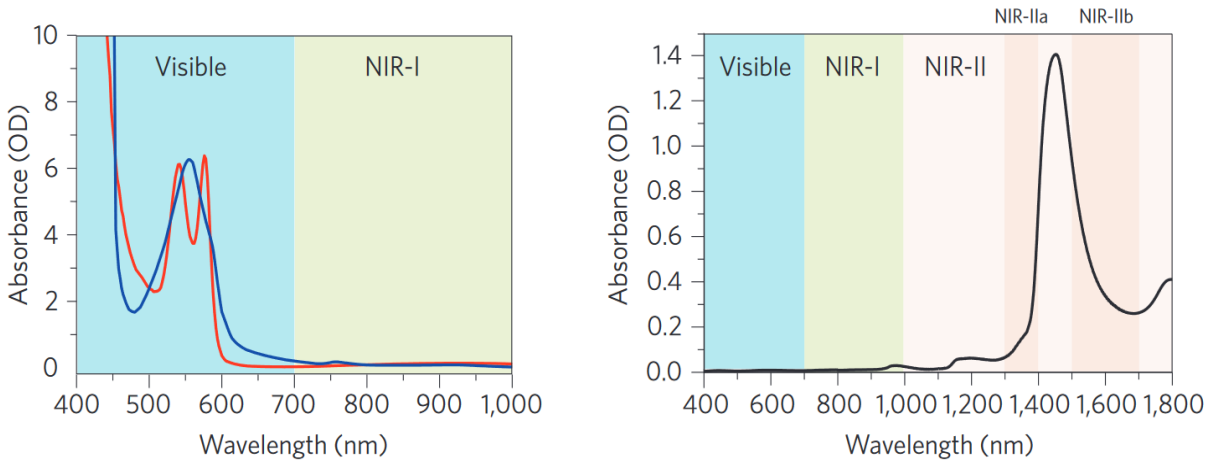

Figure 2.2 a Absorption spectra of oxyhaemoglobin (red) and deoxyhaemoglobin (blue) through a 1-mm long path in human blood[66]. b, Absorption spectrum of water through a 1-mm-long path. OD, optical density.

Before delving into the fourth limiting factor of fluorescence imaging (autofluorescence), it is noteworthy that the excitation light source can significantly affect living cells or tissues usually studied with this technique. Though specific wavelengths of light are vital for some essential life processes in plants and animals, they can be considered harmful depending on the intensities, the duration of exposure and the organism. For example, UV exposure of the skin drives the formation of pre-vitamin D3 from pro-vitamin D3 to synthesise Vitamin D3. However, further UV exposure will convert surplus vitamin D3 into inert substances and can cause sunburn.[67,68] Long exposure of live cells to UV radiation causes DNA damage and cell death. A study also reported the lethal effects of visible light on insects.[69] Therefore lower energy NIR excitation sources are considered safer for imaging live organisms and less likely to cause photobleaching of the fluorescent labels.[15,70,71]

2.1.4 Autofluorescence

Similar to scattering, the autofluorescence of vital organs and bodily fluids decreases significantly and progressively with longer detection wavelengths in the SWIR. Autofluorescence is the native fluorescence of biomolecules which spans from the UV to the NIR region. Many of the previously mentioned biomolecules like flavins and proteins contribute strongly to background tissue autofluorescence in the visible region (400-700 nm) (Figure 2.3 left).[15] Autofluorescence is more pronounced in the visible region and increasingly negligible towards the SWIR region (Figure 2.3 right). The intensity of autofluorescence is usually brighter than that of the fluorophore signal, causing a low signal-to-background ratio and, consequently, low image resolutions and sensitivities. Finding an autofluorescence-free window at the tail end of the NIR region will facilitate the fluorescence imaging of endogenous fluorescence-rich organs like the liver.[30]

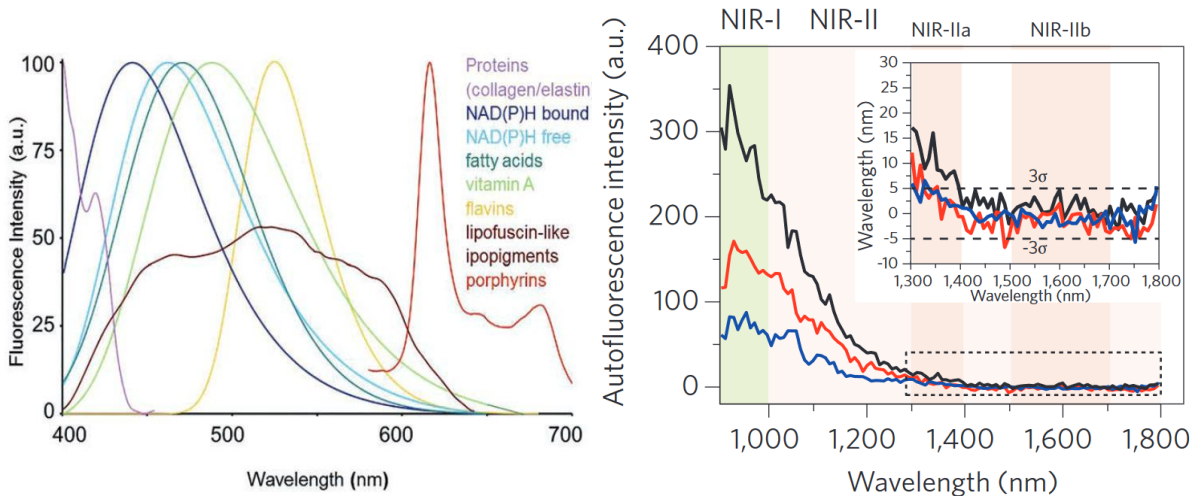

Figure 2.3 Left: Autofluorescence spectra of ex vivo mouse liver (black), spleen (red) and heart tissue (blue) under 808-nm excitation light, showing the absence of autofluorescence in the >1,500 nm NIR-II window123. Right: Autofluorescence spectra at high wavelengths. The dashed lines denote the values at three standard deviations from the baseline.[66,72,73]

2.2 Probes Used for SWIR Imaging

It is essential to consider several factors, such as the photophysical and chemical properties and biocompatibility, when choosing fluorophores for in vivo fluorescent imaging in the SWIR region. Researchers have developed several SWIR-emitting fluorophores since a mouse model's first in vivo SWIR imaging in 2009.[74,75] In vivo SWIR imaging is a relatively newer field of research compared to NIR-I imaging because biocompatible SWIR fluorophores are a recent innovation. These fluorophores include but are not limited to organic dyes, lanthanide nanomaterials, QDs, single-walled carbon nanotubes (SWCNTs), and AuNCs. The photoluminescent properties of SWIR probes have substantially improved over the last 10 years, though they are way behind visible fluorophores with 80-100% quantum yield.[52]

High quantum yield of fluorophores is generally desireable in in biosensing especially in the NIR region where signal to background ration is often low. The quantum yield (QY) of a fluorophore is the ratio of the number of photons emitted to the number of photons absorbed by it. High QY imples that more light is emitted for each absorbed photon thereby increasing the sensitivity of the biosensor. It also helps to detect signals that are close or below the

background threshold which is particularly important in the NIR region where the the signal to background ratio can be very weak. Unfortunately, most NIR-II fluorophores are plagued with low QYs because their long-wavelength photons require low bandgap materials in which non-radiative decay processes dominate radiative photon emission.[76,77]

2.2.1 SWIR Emitting Organic Dyes

Small organic molecule-based probes are highly desirable and mature for clinical applications because of their high biocompatibility, rapid metabolism and excretion, and quality control under the current good manufacturing practice conditions, well-defined architecture, and tuneable spectral properties[78–83] However, generating SWIR emission in small-molecule organic dyes that are similar in structure to those used for NIR-I imaging, is notoriously difficult due to generally low quantum yields, poor aqueous solubility and multiple synthetic steps required to produce suitable molecules with ideal bandgaps in the NIR-II window. SWIR-emitting organic dyes, such as IR-26, IR-1048 or IR-1061, are stable but highly hydrophobic and suffer from extremely low quantum yield – less than 0.05%. [84–87]

SWIR emitting organic probes, though small, are bulky and hard to synthesise. The synthesis of a SWIR absorbing fused tetraanthracenylporphyrin demonstrated the complexity of synthesising a SWIR fluorophore.[88] The most common design strategy of SWIR fluorophore is based on the modification of polymethine dyes where a reduction in energy gap is attained by extending the polymethine chain. Though this strategy increases the absorption coefficient of the dye, there is a significant decrease in the photostability of the resulting SWIR emitting fluorophore.[89] FDA approved NIR-I fluorophore, indocyanine green (ICG) and its derivatives can serve as SWIR probes for fluorescence imaging.[54,90] Researchers reported the synthesis and use of aza-BODIPY dyes derivatives for two-photon absorption to optical performances in the SWIR region.[83]

As shown in the structure (Figure 2.4), many SWIR emitting organic probes are hydrophobic and require some form of assistance such as encapsulation or PEG-coating for proper dispersion in water for optimal biocompatibility.[91,92]

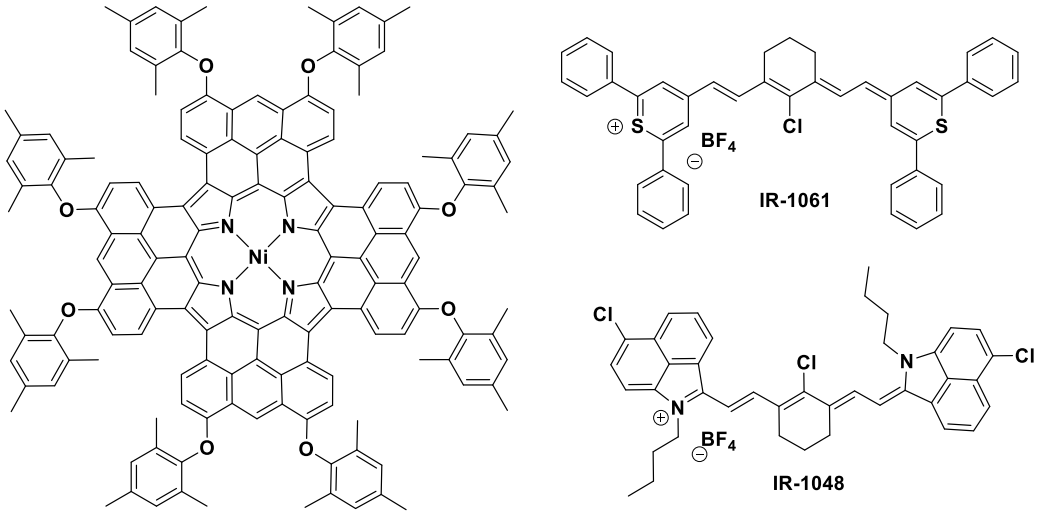

Figure 2.4 Chemical structure of fused tetraanthracenylporphyrin, [88] IR-1048 and IR-1061

In addition to their low energy gap and susceptibility to quenching by vibrational states of surrounding solvent molecules, the emission of SWIR organic dyes is strongly solvatochromic, and they generally have small Stokes shifts.[87]

2.2.2 Lanthanide-Based SWIR Fluorophores

Lanthanides can generate SWIR emissions with a large Stokes shifts when they are sensitized by organic antenna or other d-ions.[93] Figure 2.5 shows the emission of some lanthanide ions in the SWIR region. Common SWIR emitting Ln^{3+} include Nd^{3+}, Yb^{3+}, Er^{3+}, Ho^{3+}, Tm^{3+} and Pr^{3+}.

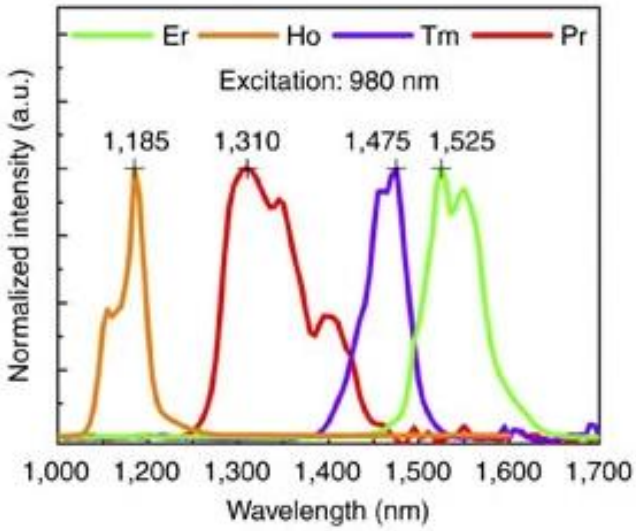

Figure 2.5 1185, 1310, 1475, and 1525 nm emissions of Ho-, Pr-, Tm-, and Er-doped NPs [94]

The drawback of lanthanide is their low intrinsic absorption; therefore, they are often used as complexes with ligands playing the role of antenna. These systems will be described in ***section 2.5***.

Over the years, there has been several reports on SWIR emitting lanthanide complexes. In 2011, Zhang and his colleagues reported a water soluble NIR emitting Yb complex specific for the mitochondria.[95] A monocyclic complex based on triazacyclononane was afterwards applied in imaging slices of mouse brainusing two-photon excitation. However, low resolution was achieved due to low signal recording. Metallacrown sensitizers were also reported as good sensitizers for Ln^{3+} with remarkable photophysical properties in the NIR region.[96,97] NIR emitting Ln complexes have also been used in detecting cell necrosis in living cells.[98,99]

Lanthanides can also be used in metal organic frameworks (MOF),[100] which are materials built by organic ligands which bridge ions or clusters such as lanthanides in three dimensional arrays. In luminescent lanthanide MOF the ligand plays both the role of stabilizer and antenna.[101]

Another possibility is to use them as nanoparticles; in these systems, they can be used in downshifting SWIR but also in upconversion or downconversion. Upconversion is an anti-

Stokes phenomenon where a fluorophore absorbs two or more low energy photons (NIR) and emits a photon of higher energy (Vis) whereas downconversion (also called quantum cutting) involves the absorption of one high energy photon to release two or more low energy photons.[102] Lanthanides usually serve as the sensitisers (Nd^{3+}, Yb^{3+} or Er^{3}) or emitters (Nd^{3+}, Er^{3+}, Ho^{3+}, Tm^{3+} or Pr^{3}) that are doped on a host matrix. The commonly used emitters in bio-imaging are Er^{3+}, Ho^{3+}, Tm^{3+} and Pr^{3}, with $NaYF_4$ as the host matrix. A good SWIR persistent phosphor comprises a suitable emitter and a proper host that stores excitation energy and then transfers it to the emitters after excitation. Researchers have used Ca_2SnO_4 as a host for the Ln^{3+} to generate SWIR persistent luminescence.[94,103,104] Though Ln-based SWIR probes favour low photobleaching, nonblinking, absence of autofluorescence, long luminescence lifetimes, minimal long-term cytotoxicity, large Stoke's shift and unprecedented penetration depths, they are plagued with relatively low quantum yield and difficult large-scale synthesis.[62]

2.2.3 Single Walled Carbon Nanotubes (SWCNT) for SWIR Imaging

SWCNTs are a class of carbon nanomaterials with intrinsic SWIR emission. They are illustrated as a single graphene sheet rolled up into a 2D honeycomb nanocylinder with diameters from less than 1 nm to a few nanometres (Figure 2.6). The dependence of the band gap on the diameter and chirality of SWCNTs allows researchers to tune the optical properties of SWCNTs. SWCNTs hold great promise as effective cell imaging probes due to their excellent optical properties such as relatively low cytotoxicity (though dose dependent [105,106]), high photostability, absence of quenching, and photobleaching in cells if functionalized properly.[56,107,108]

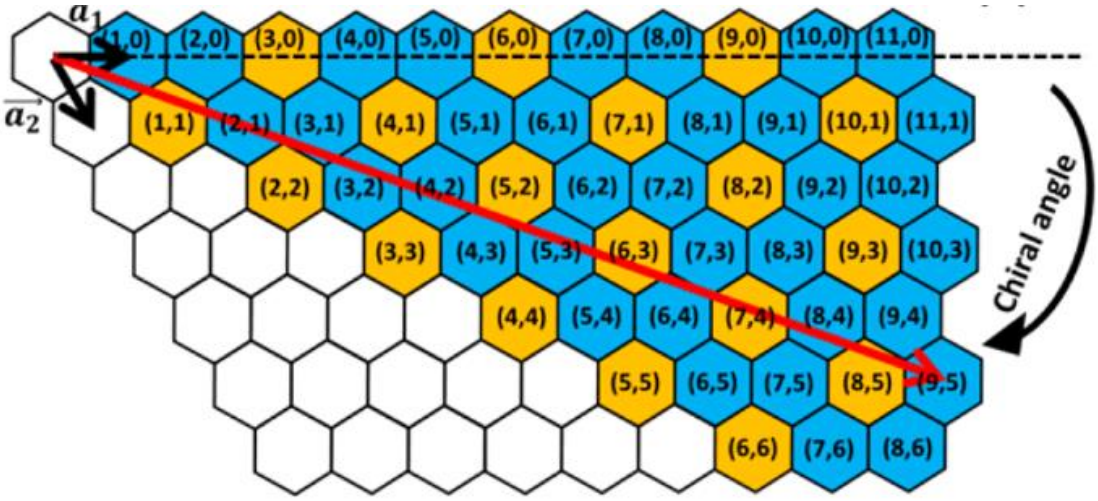

Figure 2.6 Honeycomb structure of graphene showing different roll-up vectors (red arrow) result in different (n,m) indices, or chiralities (numbers labeled in each hexagon)[66]

However, due to many quenching factors, SWCNTs exhibit a low quantum yield (0.1 – 1 %)[109–111] that is significantly lower than organic synthetic dyes, fluorescent proteins and QDs in Vis and NIR-I and SWIR regions.[66]

2.2.4 SWIR Emitting Quantum Dots

SWIR emitting QDs have significantly higher quantum yields (up to 15 %) and are brighter than SWCNTs and SWIR organic dyes. However, these quantum yields are still considered as low in the context of bioimaging applications.[30,87] The brightness of QDs partly emanates from their high extinction coefficients into the UV region. SWIR emitting QDs are made up of quite toxic metal chalcogenide such as PbS, Ag_2Se and the less toxic Ag_2S. Hence QDs are normally coated with polymers for improved biocompatibility.[112,113] While the absorption of QDs is dependent on the constituting elements, their narrow emission band is dependent on their sizes due to quantum size effect thus enabling emission tunability via size control. A group researchers reported the synthesis of SWIR emitting InAs QDs with excellent in vivo stability and no signs of toxicity for six days.[114]

2.2.5 Gold Nanoclusters

AuNCs are ultra-small clusters of tens to hundreds of gold atoms per core and a maximum diameter of 3 nm.[115–118] Unlike gold nanoparticles (AuNPs) with larger diameters and having continuous band of electronic energy, AuNCs have discrete electron excitation levels due to the small size of the gold core. Their intrinsic SWIR emission is due to electron transitions between their electron energy levels upon light activation. The photoluminescence (PL) of AuNCs widely spans the Vis to SWIR wavelength (Figure 2.7).[119] They have large Stokes shift and long luminescence lifetime. In addition, AuNCs are generally more water soluble, more biocompatible than other nanomaterials and are more photostable than SWIR emitting organic dyes. [120–125] Yu *et al.*, 2020, reported the synthesis of bright water-soluble SWIR AuNCs and applied it in the imaging of the vascular network in mice with high super-spatial resolution at > 4 mm depth. They were able to distinguish vascular disorders in mice non-invasively.[126] In 2013, Tahir and his team used the quenching of AuNCs in the sensing of toxic metal species in aqueous solution.[127] The major limitation of applying AuNCs in biomedical imaging is their low quantum yield and low brightness which have many enhancement strategies proposed.[128–130]

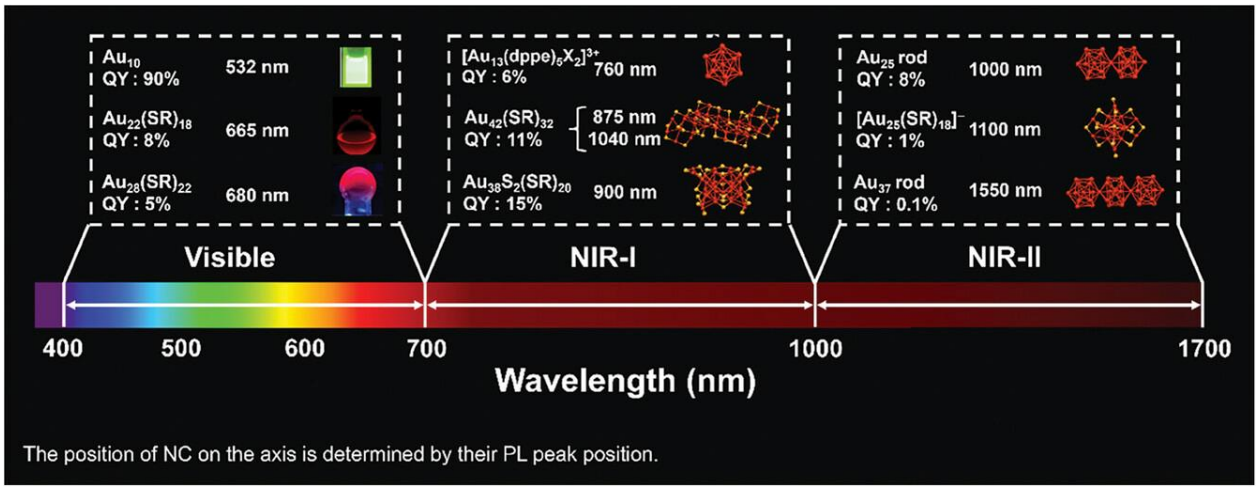

Figure 2.7 Selected luminescent homogold NCs and their PL properties (QY and peak position). The ligands on the NCs are omitted for clarity. NIR = near-infrared, I: 700–1000 nm, II: 1000–1700 nm.[119]

Asides from in vivo bioimaging applications, AuNCs can be used in the detection of ionic analytes, small molecular bioanalytes, pathogens, enzyme monitoring, and several theranostic applications.[131–133] This is because AuNCs also show some other physicochemical properties such as magnetism, intrinsic chirality, and catalytic activities.[134,135].

2.2.5.1 Structure of AuNCs

Since the photophysical and physiochemical properties of AuNCs are highly dependent on their size and monodispersity,[136] it is common practice to control their PL properties by tuning their size and structure during synthesis. It is therefore important to understand the relationship between their structure and optical properties.

The common way of synthesizing AuNCs is by the chemical reduction of chloroauric acid in the presence of thiolated ligands like glutathione, dihydrolipoic acid, DNA oligonucleotides, dendrimer, polymers, or proteins like bovine serum albumin.[137–139] The choice of ligand plays a crucial role in the determination AuNC PL properties.[125,140] Another way of synthesizing AuNCs is by etching AuNPs with sonication in water and in the presence of amino acids. Zhou and his team used this method to synthesize fluorescent Au_8 NCs.[141] Thiolate AuNCs are the most commonly studied and modelled due to the facile synthesis and optical properties. They have a metal core with Au-Au bonds and surface Au-S staple motifs (e.g., S–Au–S–) which enables a thorough study of their molecular structure and atomic composition. [135,142,143] Zhu and his colleagues in 2008, explained the correlation between the optical properties and the crystal structure of thiol-capped AuNCs. They reported $Au_{25}(SR)_{18}$ a nanocluster of Au_{13} core caged with Au_{12} shell that is linked with 18 thiolate ligands (Figure 2.8). They came to the conclusion that the quantum size effects dominates the absorption spectrum profile of these

kinds of AuNCs.[144] Heaven *et al.,* 2008, also reported a detailed crystal structure of Au_{25} NC.[145]

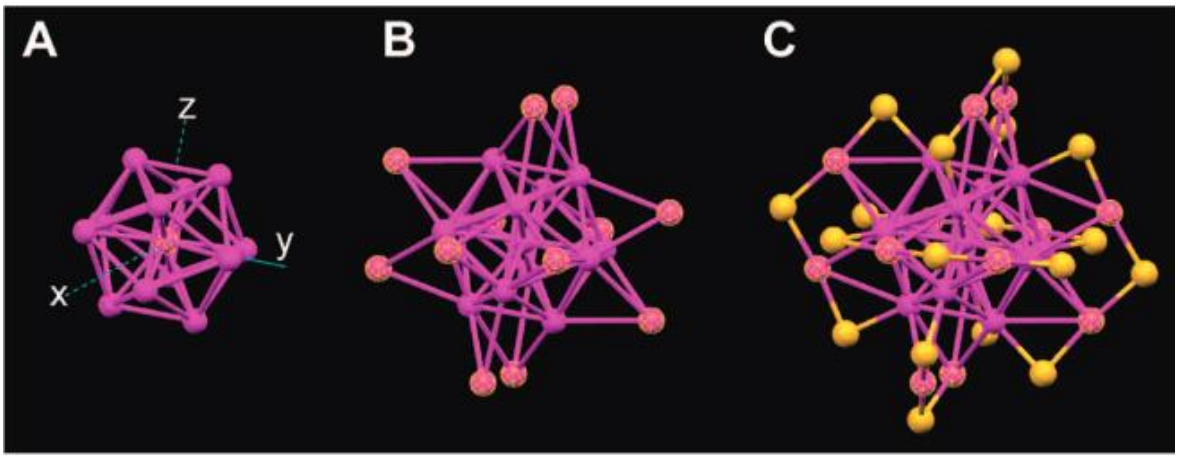

Figure 2.8 Crystal structure of a Au25(SR)18 cluster (R is phenylethyl group): (A) the icosahedral Au13 core; (B) the Au13 core plus the exterior 12 Au atoms; (C) the whole Au25 cluster protected by 18 thiolate ligands (for clarity, only S was shown, magenta, Au; yellow, S)

2.2.5.2 Optical properties of AuNCs

The photophysical and chemical properties of AuNCs result from quantum confinement due to their small size. The free electron model of bulk conductive metals describe free moving valence electrons in their conduction band. Quantized electronic states and energy levels begin to form as the size of the metal starts to reduce until it diminishes into a few atoms. Therefore, the system can be considered as a molecule with optical properties that are mainly determined by photon induced electrons transitions between electronic states. [142,146–148] Zhou *et al.* 2019, compared the photophysical properties of small organic molecules, gold complexes (no explicit core), nanoclusters (with a core and surface Au–S staples), and metallic-state nanoparticles and reported that AuNCs behave as an interface between small organic molecules and metallic nanoparticles. The difference in the electronic structures of AuNC and AuNPs is mainly due to this size related quantum effects and energy levels in AuNCs.[149]

The yellow colour of bulk gold originates as a result of the absorption of blue light in the region 350 nm to 416 nm originating from d → sp transitions. However, in addition to these

absorptions, gold nanoparticles also feature a large surface plasmon resonance (SPR) band centred around 500 nm for small spherical nanoparticles but which can red shift depending on their size and their shape.[149–151] Unlike gold nanoparticles, AuNCs do not have significant SPR, rather they luminesce like small molecules with a rapid internal conversion (IC) and long excited state lifetime.[144,149] The multiple absorption bands of AuNCs in the UV-Vis region originate from interbands (d → sp) and intrabands (sp → sp) (Figure 2.9)

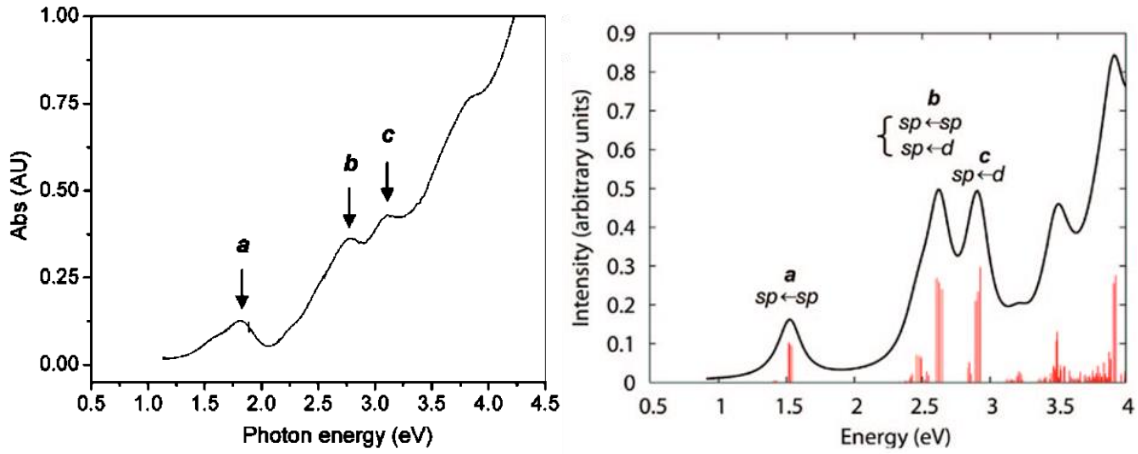

Figure 2.9 Absorption peaks of AuNCs (left) The UV-Vis spectrum of Au25 clusters (single crystals redissolved in toluene) (Right) The theoretical absorption spectrum of Au25(SH)18-. Peak assignments: peak a corresponds to intraband observed, peak b & c correspond to interband transitions. [144]

Photoluminescence in AuNCs is still in debate to know if it can be classified into fluorescence, phosphorescence and thermally activated delayed fluorescence (TADF). Fluorescence (Figure 2.10A) is the spontaneous emission of radiation from an excited molecular state while maintaining the same spin multiplicity, S=1 (singlet state).[49,152] Since AuNCs were initially considered as similar to QDs, they were generally considered to be fluorescent.[153] The presence of heavy atoms in AuNCs should results in heavy intersystem crossing (ISC) which transfers most of the singlet state (S_1) population to the triplet state (T_1). This makes phosphorescence to be more likely to happen in AuNCs than fluorescence (Figure 2.10B).[154,155] TADF occurs when T_1 populations are transferred back to the S_1 through thermally assisted reverse intersystem crossing (RISC) before finally relaxing to the ground state (S_0) as shown in Figure 2.10C. This

phenomenon can only occur when the energy difference between singlet and triplet state is minimal. The wavelengths of TADF emission and fluorescence are similar with longer emission lifetime in TADF due to excited electrons lingering in the T_1.[156–159] Since TADF relies on thermal energy, a decrease in temperature will lead to a decrease in TADF intensity and an increase in phosphorescence. Phosphorescence emissions have longer lifetimes than fluorescence emission which helps to differentiate between them. However, phosphorescence of 40 ns for gold complexes have been reported due to the strong spin-orbit coupling induced by gold,[160] which makes it more complicated to differentiate between fluorescence, TADF and phosphorescence emission.[161,162] Therefore, the PL lifetimes of AuNCs can span from 100 ns to microseconds as reported in literature and confirmed in our findings.[122,130,163]

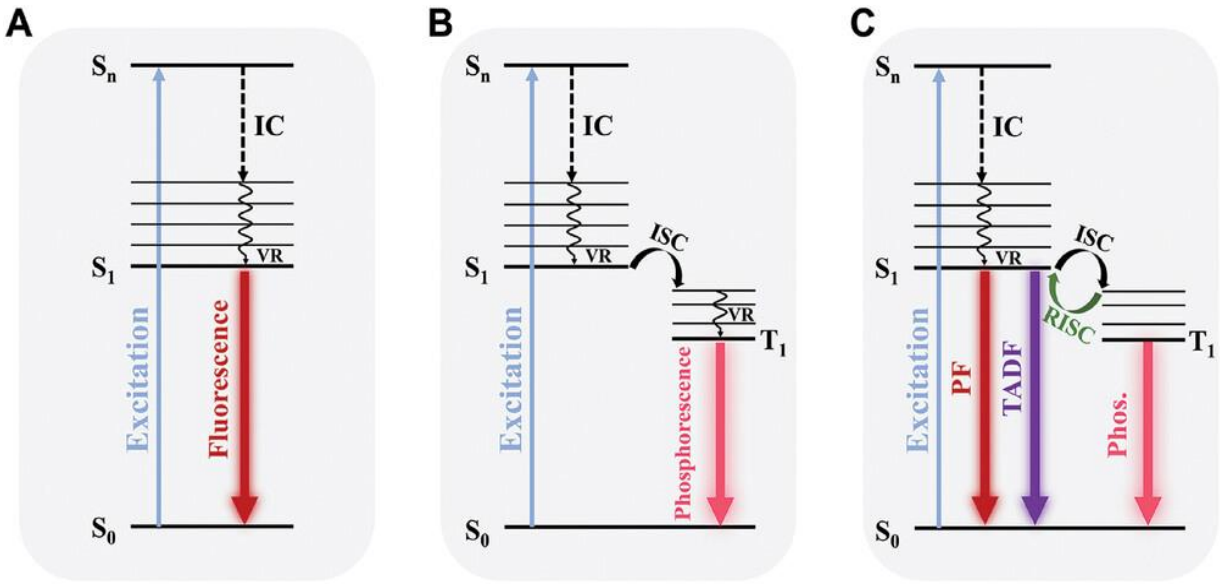

Figure 2.10 Emission pathway of A) fluorescence B) phosphorescence and C) thermally activated delayed fluorescence. (PF= prompt fluorescence, IC = internal conversion, VR = vibrational relaxation, ISC = intersystem crossing).[119]

The nature of the emission of AuNCs is very debated. Link *et al.*, 2002, proposed that the visible emissions of $[Au_{25}(SG)_{18}]^-$ are fluorescence while the NIR emissions are phosphorescence emissions. They also proposed that the visible emission is an sp ← d interband (shell) transition while NIR emission is an sp← sp intraband (core) transition.[128] Meanwhile Meng and Yongo, 2021, ruled out the possibility of the NIR emission being a phosphorescence emission because

of their shorter lifetimes in comparison with those of the visible emission, which would be counter-intuitive. However, they both agreed that the visible emission originates from the shell while the NIR emission originates from the core (Figure 2.11).[164] To come to this conclusion, they compared thiol coated Au_{25} nanoclusters with and phosphine Au_{13} nanoclusters. The X-ray structure of thiol coated Au_{25} nanoclusters showed that these nanoclusters are constituted by a Au_{13} core and 6 $(Au)_2S_3$ staples, while Au_{13} phosphine nanoclusters is only a core so they can distinguish core and surface emission by comparing these two nanoclusters.

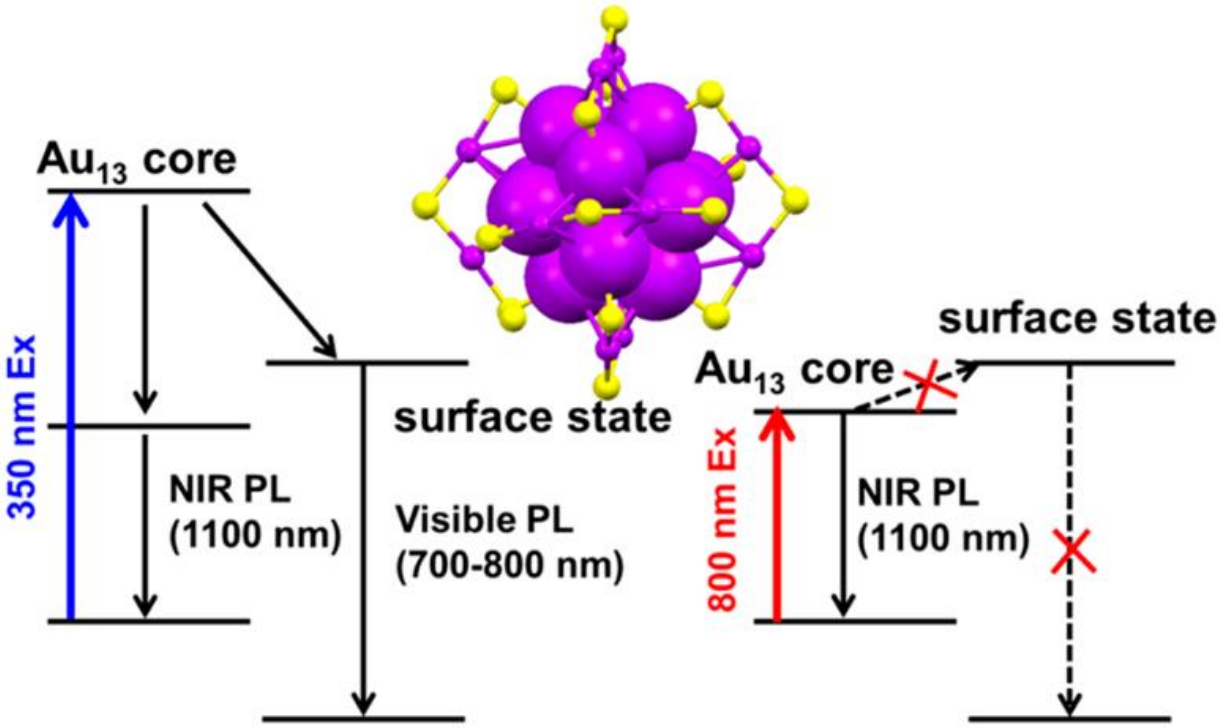

Figure 2.11 Mechanism of emissions in $[Au_{25}(SR)_{18}]^-$ nanoclusters[164]

The fact that some AuNCs can exhibit dual emission of fluorescence and phosphorescence makes them suitable for multi-colour imaging, ratiometric sensing and the development of novel optoelectric devices.[148,165,166]

2.2.5.3 PL enhancement of AuNCs

The PLQY of a fluorophore can be improved by enhancing the radiative rate or supressing the non-radiative rates. Hence, many of the methods applied to improve AuNC PL seeks to reduce

the non-radiative rates. One of such is the report of Pyo *et al.*, 2015. They found that the PL of AuNCs originates from ligand-metal-metal charge transfer of the shell-gold and also discovered very high QY triplet state in frozen media. Therefore, they rigidified the ligand on the shell with tetraoctylammonium (TOA) and realised a blue shift and an increase to 60 % QY at room temperature in the Vis region. This way, the non-radiative rate is reduced as there is limited movement of the ligand molecules. This phenomenon is well document for organic molecules. [125,167,168] Taking a cue from this, Xavier Le Guevel *et al.*, 2021, enhaced the PL of SWIR emitting AuNCs by surface ligand rigification. They reported high sensitivity of PL band at 1200 nm to polarisation and rigidification of the AuNCs' microenvironment. [136,169] Yue Chen et al., 2020 up to 3.8 % PLQY (significantly higher than the typical 0.1 %) for SWIR AuNCs by using zwitterionic ligands for capping.[121] Despite all the work done on SWIR emitting AuNCs and their great potential for biomedical application, their QY yield does not exceed 10%.[136] Hence researchers have taken other means to improve their PL. These include, doping metals into AuNCs,[170] ligand surface engineering, aggregation induced emission (AIE), confinement enhanced emission.[135]

In our work, we took the route of polymer encapsulation for the enhancement of the AuNCs PL intensities in the SWIR region. Though we had a reduction in the PLQY, we had a 4-fold higher brightness than the standard SWIR emitting probes due to multiple absorption of encapsulated AuNCs.[130]

2.3 Resonance Energy Transfer

When a fluorophore absorbs light, the electrons move from the ground state to the excited state. Excited state electrons undergo internal conversion to the lowest energy vibrational state before relaxing back to the ground state. The relaxation path of excited state electrons can be by radiative (photon emission) or non-radiative processes. Excitation energy transfer can occur as a result of photon reabsorption, excitation complex (exciplex) formation, or non-radiative energy transfer processes like Dexter electron exchange (occurring at 0 – 1 nm) and FRET.

FRET is a non-radiative physical process where excitation energy is transferred from an excited donor to a proximal acceptor molecule in the ground state. FRET is distance dependent and would usually occur at a distance around 1 – 20 nm (though NSET stretches this further). This distance is the typical interaction and size range of subcellular materials thus making FRET a major tool for biology and biochemistry. Because FRET is distance dependent, we often apply FRET as an optical technique to obtain information on molecular conformation with nanometer resolution, measuring inter/intra-molecular interactions thereby serving as a spectroscopic ruler and for in vivo diagnostics.

In this section, I will discuss the basics of FRET and factors to consider when setting up a FRET experiment.

2.3.1 FRET Theory

Theodor Förster used his understanding of classical and quantum physics to establish the notion of resonance energy transfer back in the 1940s. The effect bears his name (Förster) as a tribute to his effort. According to FRET theory, electronic energy can be transmitted from an excited donor (D) to a ground-state acceptor (A) by dipole-dipole interactions in a non-radiative

manner. His works linked the experiments and theoretical concept of FRET. In simple practical terms, three conditions need to be considered for efficient FRET to occur.

- Spectral overlap between donor (D) emission and acceptor (A) absorption.
- The relative orientation between the dipole moments of the donor and the acceptor.
- The distance between the donor and acceptor [171–173]

2.3.1.1 Spectral Overlap (The Resonance in FRET)

One can think of the donor and acceptor molecules as a collection of connected electrical oscillators. Energy transfer will occur only if the acceptor oscillators are responsive to the electromagnetic field of the donor oscillators and "share" electronic transitions, which allow the excitation of the acceptor molecule from its ground state to the excited state. At this instance, the relaxation energy of the donor molecule is equal to the excitation energy of the acceptor. (Figure 2.12 left) illustrates the fundamentals of FRET with a simplified Jablonski diagram to explain these electronic transitions. The donor absorbs excitation light (hv) to transition from an electronic ground state (D) to an excited state (D*) followed by inner conversion/inner relaxation (black dotted arrow) to lowest electronic excited state then finally to the ground state by radiative decay (k_D), non-radiative decay ($k_{D\text{-}NR}$), or FRET (k_{FRET}, dashed lines referring to possible resonant transitions. FRET (the horizontal lines connecting the coloured relaxation arrows) occurs when the relaxation energy of D* to D is in resonance with the energy needed to excite A to A*. The excited acceptor (A*) then undergoes radiative decay (k_A) and non-radiative decay ($k_{A\text{-}NR}$) to reach its ground state (A) following FRET. The spectroscopic summary of this point is that the donor emission needs to overlap with the acceptor absorption

spectra (Figure 2.12 right). The spectral overlap (J(λ)) is dependent on the extinction coefficient of the acceptor and can be described with the equation.

$$J(\lambda) = \int \bar{I}_D(\lambda)\varepsilon_A(\lambda).\lambda^4\, d\lambda \qquad (1)$$

Where: $\bar{I}_D$ is the area-normalized donor emission,
ε_A is the extinction coefficient (molar absorption) of the acceptor and
λ is wavelength in nm.

Therefore, choosing a suitable FRET pair is the first requirement for a successful FRET experiment. The donor must be a fluorophore while the acceptor can be a fluorophore or a quencher. The choice of donor or acceptor depends on the nature of investigation, the specimens to be investigated and the available instrumentation and technique applied to measure FRET.

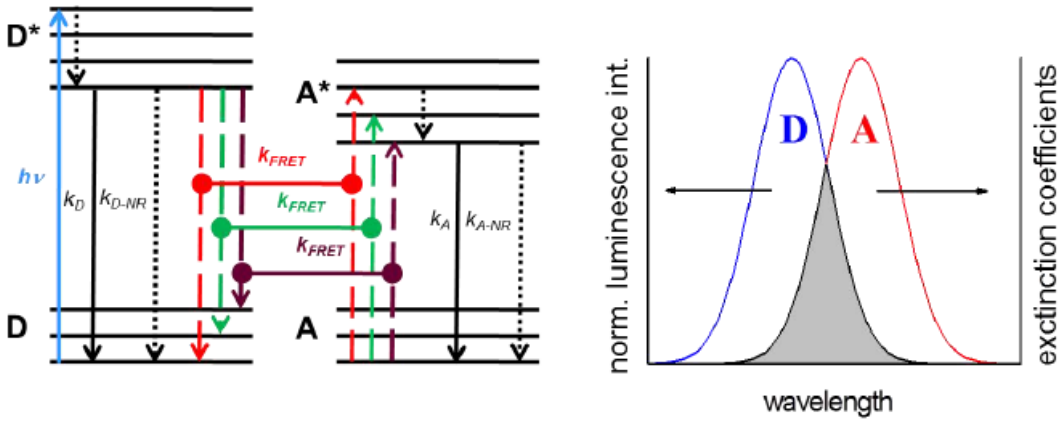

Figure 2.12 (Left) Simplified Jablonski diagram representing the energy levels of the donor (D) and acceptor (A) molecules. (Right) Spectral overlap between the donor emission and the acceptor absorption. [51]

2.3.1.2 Orientation Factor of Transition Dipole Moments (κ^2)

κ^2 describes the orientation of the transition dipole moments of donor and acceptor and can be calculated with the following equation:

$$\kappa^2 = (cos\Theta_R - 3cos\Theta_D cos\Theta_A)^2 \qquad (2)$$

Where θ_R is the angle between the donor and acceptor transition dipole moments,
θ_D and θ_A are the angles between the respective dipole moments and the line connecting the donor and the acceptor (Figure 2.13A).

In solutions where the donors and acceptors typically do not align themselves in a fixed orientation, the average value of κ^2 is assumed to be 2/3 (dynamic averaging), based on the assumption that at the moment of energy transfer, the fluorophores randomly orient themselves via rotational diffusion. However, under certain circumstances the donor and acceptor dipoles are in a fixed orientation which necessitates the computation of a case dependent orientation factor using equation (2). κ^2 may have a value between 0 to 4. When the acceptor and donor dipoles are perpendicular to one another, the value of κ^2 equals 0, meaning that there shouldn't be any potential energy transfer. The highest value of κ^2 for head-to-tail parallel orientation is 4, whereas the value of 1 applies to parallel dipoles (see to Figure 2.13 (B) for a list of all the orientations) The rate of energy transfer is linearly dependent on the orientation factor making it a key parameter in FRET theory.

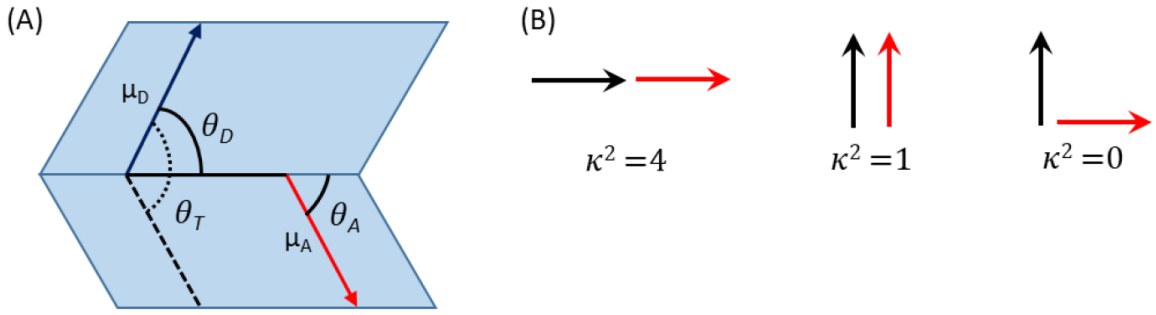

Figure 2.13 (A) orientation between the donor (μD) and acceptor (μA) dipoles, (B) donor-acceptor relative dipole orientations and their corresponding κ^2 values

2.4.1.3 Distance Dependence of FRET

Förster demonstrated that the energy transfer efficiency between two molecules is inversely proportional to the sixth power of the distance (r) between them. The FRET efficiency and the FRET rate are related by the equation

$$\eta_{FRET} = \frac{k_{FRET}}{k_{FRET}+k_D} = \frac{1}{1+\left(\frac{r}{R_0}\right)^6} = \frac{R_0^6}{R_0^6+r^6} \qquad (3)$$

Where k_{FRET} is the FRET rate;
k_D is the radiative decay rate of the donor (inverse of donor lifetime)
R_0 is the Förster distance representing a transfer efficiency of 50 %;
r is the donor-to-acceptor distance.

The rate of energy transfer (or FRET transfer rate), k_{FRET}, illustrated in Figure 2.12 left is given by

$$k_{FRET} = \frac{1}{\tau_D}\left(\frac{R_0}{r}\right)^6 \qquad (4)$$

Where τ_D is the excited-state lifetime of the donor in absence of the acceptor;
R_0 is the Förster distance representing a transfer efficiency of 50 %;
r is the donor-to-acceptor distance.

The Förster (R_0) distance is the distance at which half of the energy is transferred and is dependent on the spectral overlap (J) of the molecules. The Förster distance can be calculated by the equation

$$R_0 = \left(\frac{9(\ln 10)\kappa^2\Phi_D}{128\pi^5 N_A n^4} J\right)^{\frac{1}{6}} \qquad (5)$$

where κ^2 is the orientation factor between D and A,
Φ_D is the quantum yield of the donor,
NA is Avagadro's constant, n is the refractive index of the medium, and
J is the spectral overlap between donor emission and acceptor absorption in equation (1)

The data in Figure 2.14 demonstrates that FRET efficiency is highly responsive in the range of $0.5R_0$ to $2.0R_0$ because of the r^{-6} distance dependence. This range is known as the dynamic range where we plot the calibration curve of the FRET ratio against the concentration of the acceptor. At distances shorter than this, FRET becomes too efficient, while at longer distances

the efficiency is negligible. The FRET technique is therefore optimal for measuring distances that fall within the $0.5R_0$ to $2.0R_0$ window.

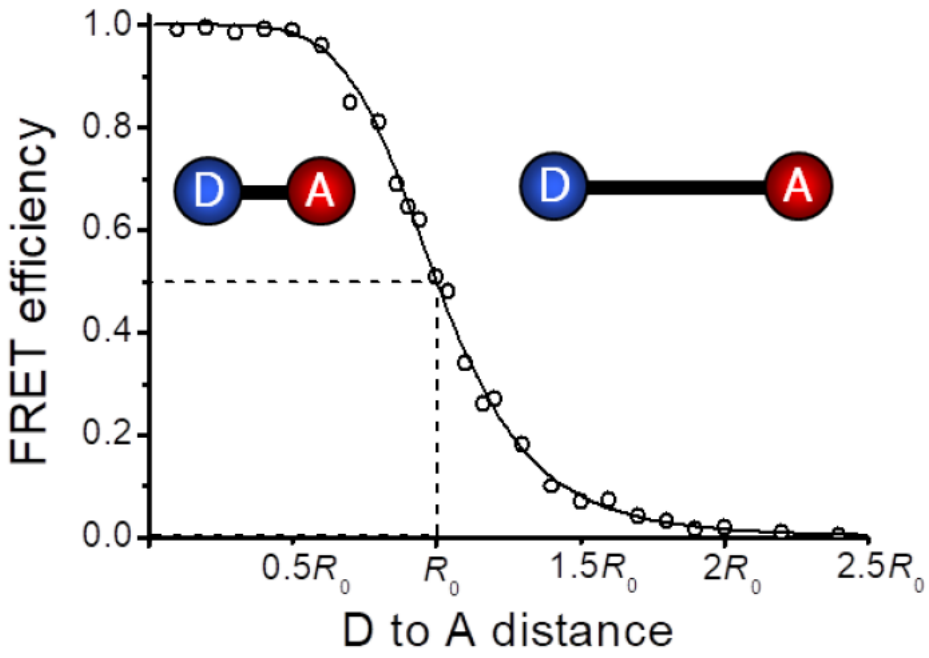

Figure 2.14 FRET efficiency as a function of D-A distance

2.3.1.4 FRET Measurement

Measurable photophysical properties such as intensity (I), litetime (τ) and quantum yield (Φ) can also be used to calculate FRET efficiency. Equation 5 utilizes the spectroscopic data of the donor by itself (subscript D) and when the acceptor is present (subscript DA) to calculate the FRET efficiency. By combining Equation 2 with Equation 6, it is possible to estimate the distance between the donor and acceptor molecules (r)

$$\eta_{FRET} = 1 - \frac{I_{DA}}{I_D} = 1 - \frac{\tau_{DA}}{\tau_D} = 1 - \frac{\Phi_{DA}}{\Phi_D} \qquad (6)$$

In most applications using biosensors, the primary goal is to quantitatively detect the analytes. By utilizing the ratiometric method to calculate the FRET ratio (F_R) through concurrently measuring the donor (I_D) and acceptor (I_A) intensities (Equation 7), we can determine the

analyte concentration. This approach can be very beneficial for analytical applications since it can inherently account for medium interferences and excitation energy variations.

$$F_R = \frac{I_A}{I_D} \quad (7)$$

2.3.2 Advantages and Limitations of Traditional FRET

FRET is generally applied in target sensing and structural analysis across scientific fields. FRET is measured by covalently labelling the FRET pair (donor and acceptor molecules) on the system of interest provided it avails the distance within the FRET range. Then the sensitization and quenching of the acceptor and donor respectively are measured simultaneously in individual detector channels.

From protein structural conformation and interaction analysis in biology, to the sensing of cancer biomarkers in medicine and to pollutant sensing, FRET stands as versatile tool for achieving unprecedented sensitivities and resolutions when combined with spectroscopy and microscopy.[174,175] FRET offers numerous advantages for biosensing and bioimaging applications due to its dependence on distance. FRET is in fact a "spectroscopic ruler" used in the study of the structure and interactions of biomolecules.[176–178]

For instance in microscopy, the resolution of conventional widefield fluorescence microscopy is limited to around 200 nm[179] whereas the typical protein interactions in biological process occurs at distances of units to tens of nanometres (1-10 nm). Therefore, to obtain meaningful information about such biological interactions, a more powerful technique is required. The energy transfer efficiency of FRET is within the range of 1 – 10 nm and can be extended to 20 nm depending on the choice of fluorophore, hence FRET provides high resolutions for microscopy applications.[180–182] FRET microscopy allows the imaging of the FRET pair colocalization in single living or fixed cell as well as the verification of molecular associations

at close distance. FRET can be applied in several microscopy techniques like simple wide-field microscopy, confocal FRET imaging, fluorescence lifetime imaging (FLIM), fluorescence loss in photobleaching (FLIP) and fluorescence recovery after photobleaching (FRAP).[183]

FRET application in biosensing takes advantage of the specificity of molecular interactions. Several FRET studies use the specific interaction of streptavidin-biotin, antibody-antigen, aptamer-analyte and oligonucleotide interactions to bring FRET pairs into reasonable distances for FRET to occur. For example, in this thesis, I used biotin-streptavidin interaction and antibody-antigen interactions for FRET biosensing. FRET biosensors are highly sensitive and specific and they can detect a wide range of biomolecules and slight changes in the FRET system environment. FRET biosensors have been applied in detecting protein-protein interactions, monitoring pH changes, measuring enzyme activities, detecting disease biomarkers and toxins in food.[182,184–188]

2.3.3 Limitations of Traditional FRET

FRET like any other fluorescence techniques suffers from drawbacks like autofluorescence, detector noise, optical noise and photobleaching. In addition, spectral bleed through and spectra crosstalk are FRET specific limitations that need to be considered when treating FRET data. Both of them are commonly reported as spectral crosstalk because their signals are almost inseparable are responsible for the low signal to noise ratio common with FRET experiments. Spectral bleed through occurs when unwanted emission signal of the donor contributes to the signal in the acceptor channel and vice versa. Spectral crosstalk involves cross excitation of the donor and acceptor; therefore, the acceptor is directly excited rather than sensitized through FRET. [183,189,190] These fluorescence intensity-based limitations of FRET measurements are mostly dependent on the probe and the measurement set up. Thus, to overcome these

limitations, we must know the fluorophores and understand the pros and cons of choosing a suitable fluorophore for FRET experiment.

2.3.4 The Probes

Organic dyes and fluorescent proteins are the classical probes for FRET experiments.

2.3.4.1 Organic dyes

Organic dyes are commonly used as donors or acceptors due to their versatility, good biocompatibility, trackable metabolic pathways, high quantum yield and well-defined and tuneable optical properties. Cyanine dyes are the most common dyes in FRET experiments.[191,192] The small size of organic dyes prevents steric hinderance which can interfere with biomolecule function and also allows the conjugation of several fluorophores with the biomolecule. However, organic dyes are susceptible to photobleaching and photodegradation. FRET can help prevent the direct excitation of an acceptor dye by the transfer of energy from a donor fluorophore. They often require high-energy UV-Vis excitation and emit in the Vis region short luminescence lifetimes in units of nanoseconds. Organic dyes have broad absorption and emission bands with low Stokes shift.[193]

2.3.4.2 Fluorescent proteins

Intrinsically fluorescent proteins are naturally present in living organisms and are very useful for FRET applications. They can easily be genetically engineered into the FRET system without the need for chemical labelling. Researchers have developed and applied many bright and photostable fluorescent proteins that have large Stoke's shift for FRET applications. This has enabled the tailoring of fluorescent proteins for FRET pairs with high FRET efficiency and develop highly sensitive FRET biosensors.[194] However, like any other protein, their (in this case photophysical) functions are dependent pH of their environment and their conformation. Such

that a fluorescent protein FRET pair optimised for a particular FRET system may not be applicable for another.[195,196]

New probes such as luminescent lanthanides and optical nanomaterials help to break the limitations of the FRET measurements.

2.3.5 Optical Nanomaterials

Optical nanomaterials are ideal FRET probes due to their tuneable size and luminescence, broad absorption and long luminescence lifetimes. Nanomaterials used for FRET measurements include, QDs, AuNPs, terbium nanoparticles (TbNPs), upconversion nanoparticles (UCNPs), graphene oxides, and so on.[197] The spectral properties of these new probes in combination with time-resolved measurements are crucial for augmenting the signal to noise ratio of FRET measurements. The large surface area of nanomaterials provides ample room for immobilizing biomolecules enabling efficient interactions between target and analytes. Their large surface-to-volume ratio enhances sensitivity, making them well-suited for ultra-sensitive biosensing applications.[198] Large single fluorescent nanomaterials like QDs can also act as multiple energy donors or acceptors (multiple emitters) thereby increasing sensitivity of FRET measurements.[199,200] However, the large surface of nanomaterials can promote steric hinderance which can lead to non-specific interactions thereby giving rise to false positives. This problem can be solved by optimizing the sensor design and using specific binding motifs.[201,202]

2.3.5.1 Quantum Dots

QDs are luminescent inorganic semiconductor nanoparticles that are primarily composed of groups II-VI (CdS, CdSe, CdTe, ZnS, ZnSe, ZnTe), III-V (GaAs, GaN, GaP, InAs, InP), IV-VI (PbS, PbSe), I-VI (Ag_2S, Ag_2Se, Ag_2Te), and I-III-VI (AgInS, AgInSe, CuInSe, CuInSe) of the periodic table. These materials are combined as alloyed structures, core/shell structures, and

doped structures. QD sizes usually range between 1-10 nm and as a result, they exhibit quantum mechanical behaviour whereby their PL emission wavelengths can be tuned by varying their core sizes (Figure 2.15). Efros *et al.,* 1982 and Ekimov *et al.,* 1982, showed the effect of the ultra-small size of particle on its optical and electrical properties. Brus and his colleagues at Bell Labs were first to report colloidal quantum dots 1983. Then, Bawendi *et al.*,1993, synthesized nearly monodisperse QDs in high-temperature organic solutions.[203–206] Alexi Ekimov, Moungi Bawendi and Louis Brus jointly won the Nobel prize in Chemistry in the year 2023 for their seminal works on quantum dots.[39] In 1998, Chan *et al.,* and Bruchez *et al.,* proved that the attachment of thioglycolic acid or coating a hydroxyl-functionalized SiO_2 shell on the surface of QDs made them to become more water soluble and biocompatible. Their findings opened up the frontiers for the application of QDs in life sciences.[207,208]

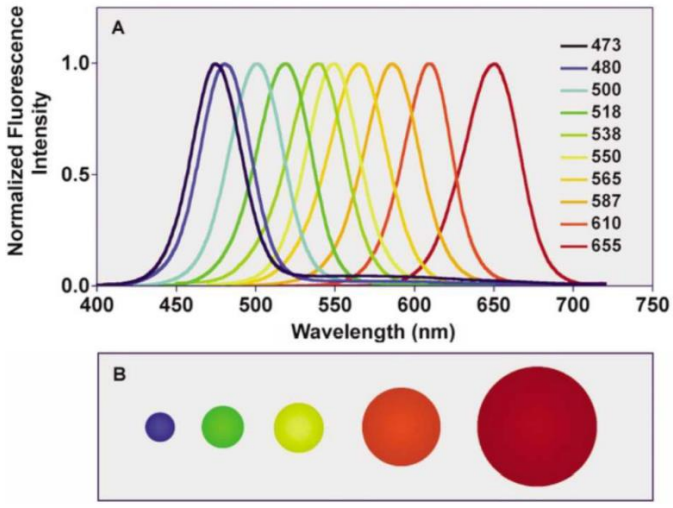

Figure 2.15 (A) Size dependent fluorescence spectra of quantum dots, (B) Different relative particle sizes with diameters between 2.1 - 7.5 nm [209]

QDs are attractive probes well suited for fluorescent labelling due to the quality of their photophysical properties. They are very bright because of their high quantum yield (up to 100%) and high extinction coefficient (~10-100 fold higher than organic dyes). The absorption spectra of QDs are very broad, which provides several photo-excitation wavelength options. They have narrow, size-dependent emission spectra spanning from the UV to NIR region,

which is ideal for multicolour and multiplexing applications. QDs have large Stokes shift that separates the excitation from emission effectively. They are resistant to photobleaching and chemical degradation and therefore suitable for real-time bioimaging. The PL lifetimes of QDs is tens to hundreds of ns, which is 10-100 times longer than organic dyes.[201]

Apart from the general limitations of using nanoparticles for fluorescent applications mentioned before, QDs have some limitations in their use. One limitation is that QDs emit from the core and not from their surface, very large QDs can limit the useable distance range because other molecules can only be attached at the surface. QDs are not ideal for single molecule measurements as they are prone to photo-blinking. Though researchers have developed and applied properly coated and biocompatible QDs in many in vivo and in vitro imaging studies, the toxicity of QDs remains an important subject matter.[201,210]

2.4 AuNPs Quenchers (NSET and FRET)

AuNPs are one of the most stable nanoparticles. AuNPs are excellent energy acceptors due to their unique SPR, which overlaps with the emission of many fluorescent donors in the visible range.[211] AuNPs have large SPR-dominated absorption bands, they emit negligible photons but rather generate heat due to the degenerate state of their conduction band. Dulkeith *et al.,* 2004, demonstrated that the PLQY of AuNPs to be around 0.0001%.[212] The optical properties of AuNPs can be tuned by tuning their size, shape and surrounding environment like ligand and electrolyte ions.[213]

The SPR arises from the collective oscillation of conduction electrons across the nanoparticles due to their resonance with the excitation photons. The surface plasmon band (SPB) continues to decrease with decreasing AuNP size until it becomes non-existent around a 2 nm AuNP

diameter where the AuNP is considered as AuNC. In addition to size and ligand, the SPR of AuNPs is also sensitive to the solvent, interparticle distance and temperature.[214,215]

2.4.1 NSET and FRET

Metal nanoparticles are strong quenchers for dyes, QDs, fluorescent proteins and lanthanide complexes[216] because their SPB overlaps well with the emission band of the fluorophores. FRET was commonly thought to be the mechanism by which AuNPs quench fluorescent probes[217–219] but the energy transfer range doubled that of FRET. Hence NSET, first theorised by Persson and Lang,[214] is a better explanation to the quenching mechanism of metallic nanoparticles (like AuNP) in place of FRET. Chen *et al.,* 2018, proved that Terbium luminescence was indeed quenched by NSET and not FRET.[216] Nanosurface Resonance Energy Transfer (NSET) like FRET, is a distance dependent dipole-dipole non-radiative energy process. But unlike FRET, the acceptor is a nanometric surface modelled as a collection of many dipoles.[216] Persson and Lang, 1982, calculated the rate of energy transfer by using Fermi's Golden Rule.[214] Persson and Lang's approximation relates the energy transfer rate to the product of the interaction between the donor and the acceptor such that $k_{ET} \sim F_D F_A$. For point dipole like organic dyes and metal complexes $F \sim 1/R^3$ while in the case of 2D dipole surfaces presented by nanomaterials like AuNPs, $F \sim 1/R$ where R is the distance between the dipoles. Therefore, in the case of FRET, $k_{FRET} \sim F_D F_A \sim (1/R^3)\ (1/R^3) = 1/R^6$, whereas $k_{NSET} \sim F_D F_A \sim (1/R^3)\ (1/R) = 1/R^4$. NSET can therefore measure long range distance of up to 50 nm which is more than double that of FRET.

The NSET efficiency is thus inversely proportional to the fourth power of the distance between the donor and the surface of the metallic nanoparticle. The Förster distance equivalent for NSET (R_0) which is the distance for 50% energy transfer efficiency is calculated by:

$$R_0^{NSET} = \left[0.225 \frac{\Phi_D}{\omega_D} \frac{1}{\omega_F \omega_F} C^3\right]^{\frac{1}{4}} \qquad (8)$$

where ω_D is the angular frequency resonant with the donor electronic transition, ω_f and k_f are the angular frequency and the Fermi vector for bulk gold, respectively, and c is the speed of light.

Asides distance dependence, NSET is also dependent on the size of the AuNP. Since, the optical properties of the AuNPs can be tuned by adjusting the particle sizes, it makes sense that NSET efficiency can be tuned by nanoparticle size as demonstrated by several studies.[220–223] There are several studies and applications of AuNP NSET with organic dyes and QDs. Though mostly used for fluorescence quenching in biosensing ang bioimaging, Hildebrandt *et al.* 2023, detailed the intricacies of finding a sweet spot for applying AuNPs in plasmon enhance fluorescence (PEF) with QDs.[224]

In this thesis work, I demonstrated the quenching of Tb luminescence by AuNP via NSET.

2.5 Luminescent Lanthanides

Lanthanides are a group of 15 elements (La, Ce, Pr, Nd, Pm, Sm, Eu, Gd, Tb, Dy, Ho, Er, Tm, Yb, and Lu) at the sixth period and IIIB group in the periodic table of elements. Lanthanides with Scandium and Yttrium are classified as rare-earth metals. “Rare” not in the sense of scarcity (as they were once thought to be) but rather due to the difficulty in producing them in their pure forms.[225,226] The first rare earth metals were discovered in 1787 as a mineral called Ytterbite, which name after the village where it was found Ytterby (Sweden). A Finnish chemist - John Gadolin studied the mineral and found an unknown oxide, which he named yttria. Elemental lanthanides are highly unstable and are often found as oxides and fluorides in rocks, ores and minerals. Thus, it took over 100 years to discover all the lanthanides that we use today. Cerium (Ce), was the first lanthanide discovered in 1803 in a mineral form called Cerite and the last lanthanide is to be discovered was promethium (Pr) which was discovered

in 1938. As extraction and separation methods began to improve, lanthanides became one of the corner stones of our modern technology, playing important role in anticounterfeiting,[227] optical device technologies,[228] medical imaging[229] and biological assays.[230]

The general electronic configuration of lanthanide atoms is $[Xe]4f^n5d^m6s^2$, where [Xe] represents the electronic configuration of Xenon (with its own electronic configuration of $1s^2$ $2s^2$ $2p^6$ $3s^2$ $3p^6$ $4s^2$ $3d^{10}$ $4p^6$ $5s^2$ $4d^{10}$ $5p^6$) and n is the number of electrons ranging from 0 -14 while m could be 0 or 1. Lanthanide ions in aqueous solution are most stable in the +3-oxidation state (Ln^{3+}). Ln have similar chemical and physical properties as a result of their specific electronic configurations. They vary slightly from one another as a result of decrease in ionic radii with increasing nuclear charge. This phenomenon is called lanthanide Contraction. Lanthanide contraction results in diffuse localization of electrons in the f orbitals and low shielding of the outer electrons from the increasing nuclear charge. An interesting property of Ln is that the electrons in the f orbitals are shielded by the filled 6s and 5p orbitals which prevents strong perturbations of the spectroscopic properties of Ln by the surrounding environment (solvent molecules, ligands and anions). This results in sharp and narrow emission bands. This shielding effect makes the Ln ion to form electrostatic interactions with ligands and not as covalent. The coordination of ligands to a central Ln^{3+} depends on the strength of the electrostatic interaction and the steric demand of the ligand. The coordination number of a Ln^{3+} in solution is usually between 8 to 10 depending on their ionic radii. For example, Tb^{3+} has a coordination number of 9 in CoraFluor and Lumiphore complexes. However, this number can change depending on the oxidation state of the Tb ion, the coordinating ligand, and the structure of the crystal in which Tb is incorporated. The f-f transition of Ln is forbidden by the spin and Laporte rule and this leads to very low extinction coefficient and long excited-state lifetimes of several milliseconds. [231–235]

Lanthanide luminescence is due to the large number of energy levels involved in electron redistribution of the 4f orbitals. The energy levels are determined by the Columbic interactions and spin-orbit coupling between the f orbital electrons. The Columbic interaction (mutual electron repulsion) generates a total spin angular momentum (S), and the total orbit angular momentum (L), with the spin-orbit coupling defining the total angular momentum (J) of the f electrons. These form the quantum numbers that determines the distribution and energy levels of 4f electrons. The quantum numbers L, S, and J can further be split by weak field effects as shown in Figure 2.16.[234,236,237]

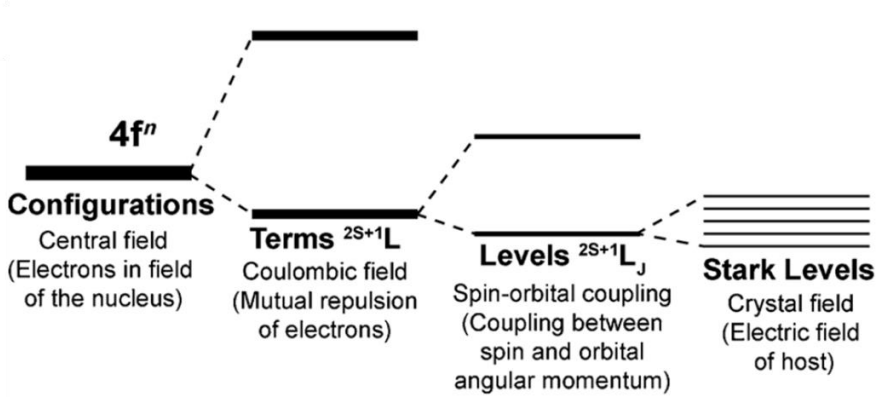

Figure 2.16 Simplified representation of the effect of Coulombic field, spin-orbit coupling, and crystal-field interaction on the [Xe]$4f^n$ configuration.[236]

2.5.1 Luminescent Lanthanide Complexes

Since the 4f transitions of Ln violates Laporte rule and results in very low absorption coefficients, Ln usually require sensitizers. A sensitizer is a compound that absorbs light efficiently and transfers the energy to the Ln^{3+}. This phenomenon was first observed by Weissman in 1942. He observed that the PL of Eu^{3+} could be increased in the presence of some aromatic organic ligands.[238] This formed the basis for the "antennae effect" (Figure 2.17A), in which heteroaromatic ligands are designed to coordinate strongly to the Ln^{3+} emitters, thereby functioning as sensitizers through their aromatic moieties. The antennae usually absorb in the UV while the Ln^{3+} emits in the Vis or NIR region thereby providing large Stokes shift between the excitation and emission spectra. Having overcome the absorbance limitation, the f-f

transition still remains forbidden and the probability of relaxation from the excited state remains low (Figure 2.17B). This prolongs the excited-state lifetime of Ln to milliseconds range. Tb and Eu have a few ms lifetime and NIR emitting Yb can reach up to tens of milliseconds.[239] The long ms lifetime of Ln and the short ns lifetime of most fluorophores create the possibility for time-resolved and time-gated photoluminescence measurements.[240,241]

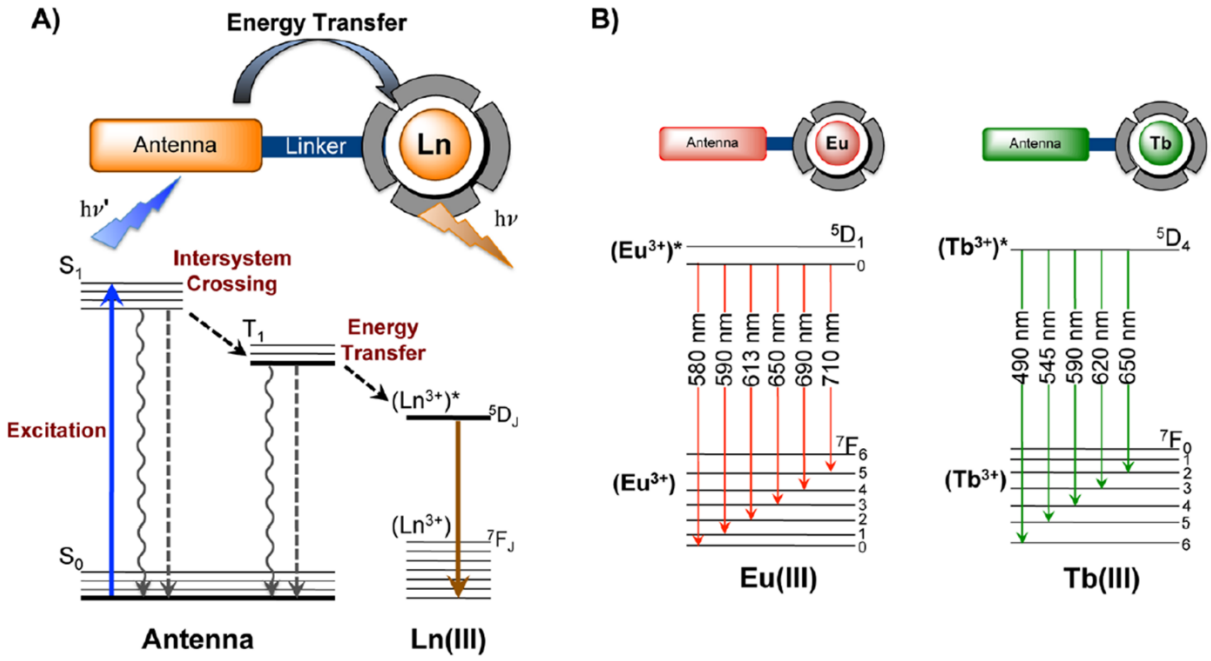

Figure 2.17 (A) Simplified Jablonski diagram for the antenna effect and the scheme of lanthanide complexes (the Ln center surrounded by a chelate and equipped with a sensitizing antenna). (B) Commonly observed emission wavelengths of europium (red) and terbium (green) complexes.[241]

The general structure of a luminescent lanthanide complex is a Ln^{3+} centre surrounded by coordinating atoms (chelate) and equipped with a sensitizer (antennae ligand). The chelates prevent the release of free Ln^{3+} and also prevents the quenching from vibrational oscillators like O-H of water. It also serves as a scaffold for the conjugation of biomolecules as applied in this work.

Over the years, researchers have found several ways to exploit the unique optical properties of luminescent lanthanides. Luminescent lanthanide complexes (LLCs) and lanthanide-based nanoparticles play essential roles in many photoluminescence applications such as electronic

display, optical data storage, biological labelling and bioimaging. LLCs like Tb complexes are essential energy donors for the development of very sensitive FRET biosensors. A good LLC for FRET applications must meet certain criteria. They must be highly stable in biological buffers, insensitive to the assay environment and they must have long luminescence lifetimes that facilitates the time-resolved and time-gated measurements. Some examples of ligands that have been developed for lanthanide chelation with are shown in Figure 2.18 (top).[242–244] Another good example of such LLC is the lumiphore Tb complex (L4Tb) shown in Figure 2.18 (bottom) which was developed by Raymond and his team. L4Tb is a commercial luminescent Tb complex made of a highly-preorganized macrocyclic ligand (1,4,7,10-tetraazaacycliododecane). It has high extinction coefficient of 26,000 $M^{-1}cm^{-1}$ at 340 nm.[245] Our team has applied L4Tb complex for many FRET applications with quality results. The advantage of a commercial ligand like this is that it relieves the burden of synthesising the Tb complex and allows us to focus on the different applications of the probe.

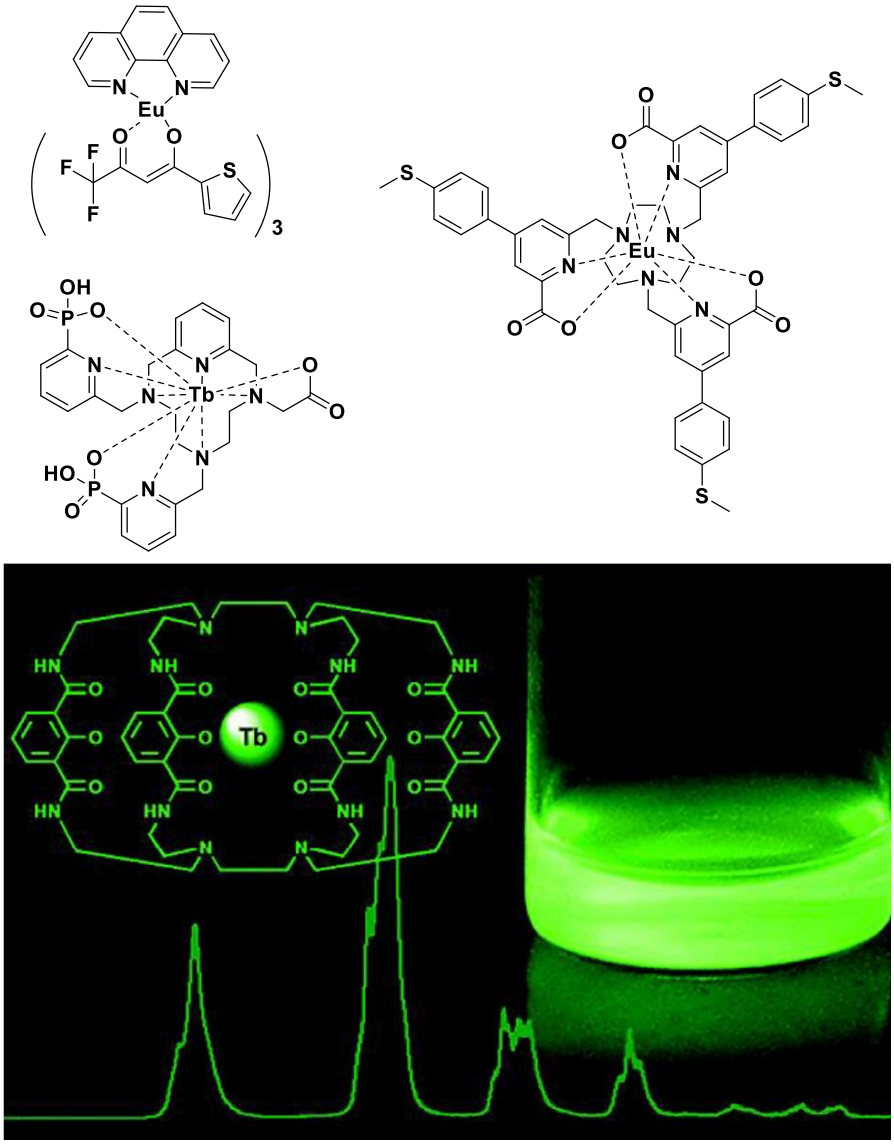

Figure 2.18 Structure of other LLC (Top).[242–244] Bottom Cage-like structure of the ligand for photon harvesting of the Lumi4-Tb complex (Bottom)[245]

Despite all the advantages that commercial luminescent Tb complexes provide, there are not many options of such complexes to choose from. Chapter 4 of this thesis investigates the properties of a new commercial Tb complex – Corafluor Tb (CRF) and the chance that it is a good option for FRET applications.

2.6 Measurement Techniques

Fluorescence spectroscopy frequently employs time-resolved (TR) observations because they provide complementary information to steady-state data, especially in the study of biological macromolecules and cellular imaging.[49] Time-resolved measurement is a powerful spectroscopic technique that helps to break the aforementioned FRET limitations that are based on fluorescence intensity measurements at steady state. Steady-state measurements are affected by probe concentration and excitation light power while fluorescence lifetime is independent of probe concentration.[246] While steady-state measurements measure the wavelengths and intensity of emission at a given time, time-resolved measurements measure the luminescence decay rate (duration of luminescence) of a probe at a particular wavelength. With time-resolved measurements, it is easy to distinguish between autofluorescence, cross-talk and the desired measurement (FRET) signals due to the evident differences in their decay rates.[247] Luminescent probes with long lifetime are required for obtaining high quality data bioimaging (high resolution) and biosensing (high sensitivity) in the autofluorescence dominated UV-Vis region. Lanthanide complexes and nanoparticles are well coveted for their long luminescence lifetimes (up to ms) and have been describe well above (***section 2.5***). QDs and AuNCs also have long luminesce lifetimes that are suitable for time-resolved measurements. Below is a table of different classes of fluorophores with their luminescent lifetimes.

Table 1 Fluorophores and their Luminescent lifetimes

Luminophore	Maximum Lifetimes
Lanthanide chelates[22,237,245]	µs-ms
Lanthanide-doped nanoparticles[248,249]	µs-ms
Transition-metal complexes[250] and transition metal doped-QDs[251–253]	Hundreds of ns-µs
Lattice-straned QDs[254]	Hundreds of ns
Carbon dots[255]	~s
Metal nanoclusters[130,256]	~µs
Persistent nanoparticles[257]	~days

2.6.1 Time-gated Measurements

As shown in Figure 2.19, in a typical TG measurement, the luminescent probe is excited by a pulsed light, and exhibits relatively long decay time. The detector starts to measure (acquisition) after a delay time in which short-lived autofluorescence (ns lifetime) fades. Thus, only long-lived ms emissions will be detected in the signal collection window (time-gate) before the next measurement. The integrated area of the decay curve that falls within the time-gate (area of the green curve within the time-gate) is recorded as the true intensity of the signal. These signals can be distinguished from short-lived background even if they are low intensity, which significantly enhances the detection sensitivity.[247] The application of long lifetime LLC donors in FRET systems (mentioned in ***section 2.4***) enables time-gated measurements that efficiently suppresses spectral crosstalk (mentioned in ***section 2.6***).

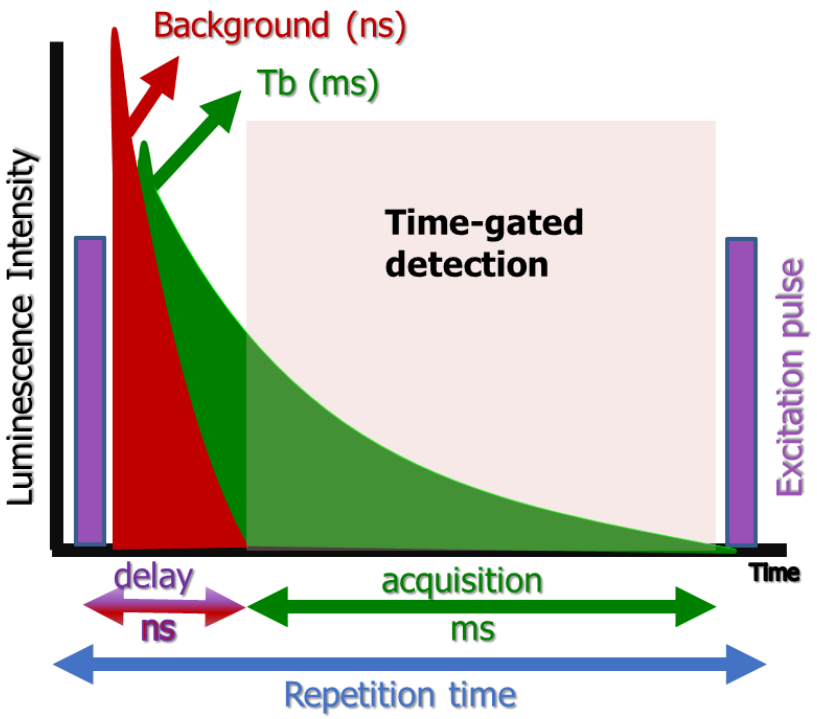

Figure 2.19 Principle of TG measurement

2.6.2 Time Resolved Measurement

The luminescence lifetimes of fluorophore represent the average time for a molecule to remain in the excited state before emission of a photon. Luminescent lifetime can be measured in the time domain and the frequency domain. The method employed in this thesis is the time-domain method. When measuring in the time domain, time-dependent intensities are measured after a short pulse excitation of light. The pulse widths are very short, and depending on the lifetime of the sample, the excitation pulse can range from nanoseconds (ns) for lasers to microseconds (μs) for flash lamps. Single or multiple luminescence decay times τ_i are determined by exponential fitting of photoluminescence decay curves based on the equation

$$I = \sum_i A_i e^{\frac{-t}{\tau_i}} \qquad (9)$$

Where I is the luminescence intensity;
A_i is the amplitude for different τ_i;
τ_i is the different decay times

When the luminescence decay is multi-exponential, each decay time is weighted in terms of fractional intensity or amplitude and is called the intensity-average or amplitude-average lifetime, respectively. Depending on the phenomenon being studied, the intensity-average lifetime $<\tau>_{Int}$ is used to calculate the mean collisional quenching constant while amplitude weighted average lifetime $<\tau>_{Amp}$ is used for calculation of FRET efficiency in FRET experiments.

$$\langle\tau\rangle_{int} = \frac{\sum A_i \tau_i^2}{\sum A_i} \qquad (10)$$

$$\langle\tau\rangle_{Amp} = \frac{\sum A_i \tau_i}{\sum A_i} \qquad (11)$$

Decay curves generated for the time-domain measurements are fitted using the least-square method by varying the fitting parameters Ai, αi and τ_i in Equations 9-11 until a best fit is obtained between the experimental data and the mathematical fit values. Fluorophores with short lifetimes (ns range) require the deconvolution of the instrument response function (IRF) from the measured fluorescent decay to obtain the actual lifetime. This is because the measured decay is a convolution of the true signal and the IRF. The IRF depends on the optical set up of the instrument and the shape/ pulse width of the pulse. It is a convolution of the pulse duration, detector response and the electronic time response of the acquisition system. The IRF is measured under the same conditions as the sample using non-fluorescent, light scattering colloidal samples like Ludox which is a colloidal silica solution.[49]

$$I(t) = \int_{-\infty}^{t} IRF\ (t') \sum_i A_i e^{-\frac{t-t'}{\tau_i} dt'} \qquad (12)$$

Where t' is the fitting starting point

Figure 2.20 shows a typical short lifetime decay curve in the time-domain with the IRF function. Lumiphores with long lifetimes (ms) range are not affected by the IRF and so do not require deconvolution. The decay curves are acquired by exciting a fluorophore with a pulsed laser as represented in Figure 2.19 above, while observing its emission intensity at a fixed wavelength over an acquisition time frame. Then depending on the luminescence lifetime of the fluorophore, the photons arriving at the detector can be counted by time correlated single photon counting (TCSPC) or multichannel scalers (MCS). Other photon counting techniques are steady-state or gated photon counting. In this thesis, I have used time-domain for all luminescence lifetime measurements.

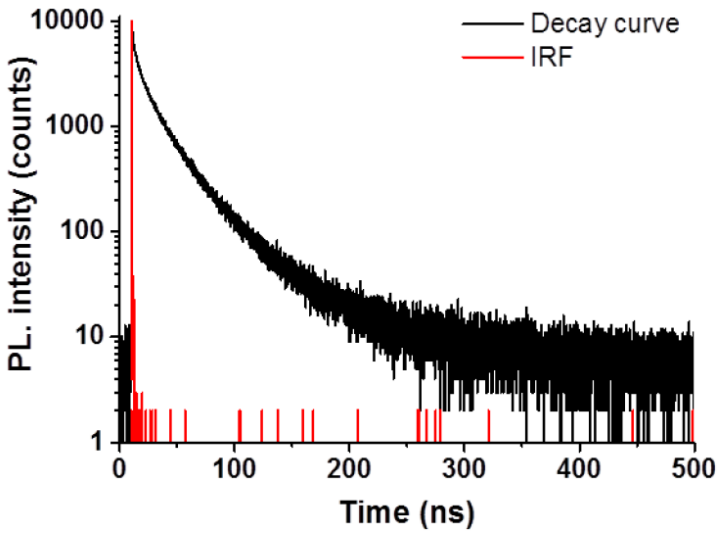

Figure 2.20 (Black) Multi-exponential decay curve of a QD sample emitting at 605 nm when excited by a pulsed laser at 405 nm. (Red) Instrument response function (IRF) measured at excitation wavelength of 405 nm. "Deconvolution" of the 2 curves resulted in a typical lifetime of QDs with $<\tau>_{amp}$ = 4.8 ns.

2.7 Ultrasensitive FRET Based Immunoassays

Antigen-antibody interaction is a well understood and widely applied technique in medicine and life-sciences. Immunoassays use antigen-antibody interactions to detect and quantify an analyte in complex biological samples such as serum, plasma, saliva and blood. Owing to the specificity, sensitivity and versatility of antibodies, immunoassays are the most preferred method for full automation and high-throughput measurement of heterogeneous molecules in

complex biological samples. Immunoassays can be classified into homogenous and heterogeneous assays. Heterogeneous assays requires several washing steps to separate unbound components while the antigen-antibody is bound to the solid phase while homogenous assays generate signals upon binding in situ.[258,259]

Immunoassay measurements can be setup as competitive or non-competitive assays. In competitive assays fluorescence labelled analytes are set up to compete with the analytes of interest for limited amount of antibody. Therefore, the detected signal is indirectly proportional to the analyte concentration (Figure 2.21 right). In non-competitive immunoassays, two antibodies bind two different epitopes of the same analyte of interest. One of the antibodies is labelled with a fluorophore and signal is detected only when the sandwich is formed. In this case, the signal intensity is directly proportional to the analyte concentration (Figure 2.21 left).

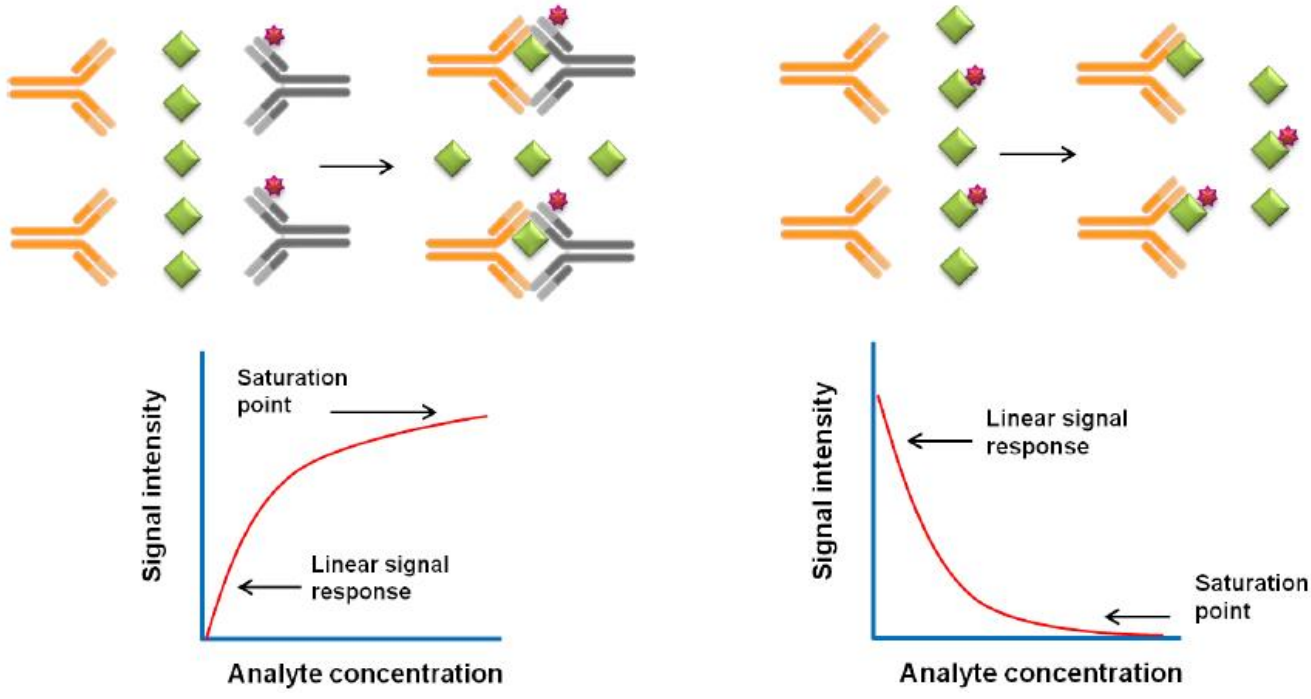

Figure 2.21 Left. Non-competitive immunoassay (sandwich format) Right. Competitive immunoassay (orange: capture antibody, grey with red star: labelled detection antibody, green: antigen)

2.7.1 FRET Based Immunoassays

FRET-based immunoassays have greatly improved since the first demonstration by Ullman *et al.,* in 1976.[260] The combination of FRET with immunoassays provide higher sensitivity and selectivity. In competitive FRET immunoassay, the two antibodies are labelled with either the donor or acceptor probe. FRET signal is only produced when they form a sandwich with the analyte as previously described. Since FRET is distance dependent, the choice of FRET pairs (probes), the size of antibodies and the probe distances should be carefully considered so as to achieve optimal energy transfer between FRET pairs. As proteins provide many functional groups for probe bioconjugation, the number and position of the probes on the antibodies are important for reproducibility of the assay.[176] The relatively large sandwich complex can limit FRET efficiency with conventional probes such as dyes. As mentioned in section 2.3.4, nanomaterials like QDs and luminescent lanthanides help to provide solutions to such limitations. Nchimi-Nono *et al.,* 2013, carried out time-resolved immunoassay using Tb complex and dyes for the detection of total prostate specific antigen (TPSA).[261]

The use of Tb complex and QDs as donor and acceptor for time-resolved FRET was first reported by Hildebrandt and Charbonnière. In their work, they used streptavidin conjugates of Eu^{3+} and Tb^{3+} complexes as donors and titrated against CdSe/ZnS QDs. They realised a large Förster distance of R_0 ~7-11 nm due to the large molar absorption and broad absorption spectra of QDs. The large R_0 led to more efficient FRET and higher sensitivity. The narrow emission bands of the QDs reduced the cross talk and the long PL lifetime of the Tb complex enable time-gating to eliminate background sign. This further contributed to the high sensitivity realised by Tb-QD FRET.[262–264] This concept was translated to immunoassays and used to detects sub nanomolar concentrations of various cancer biomarkers like Epidermal Growth Factor (EGFR), prostate-specific antigen (PSA), neuron-specific enolase (NSE),

carcinoembryonic antigen (CEA). Bhuckory *et al*., 2016, reported a multiplexed sensing of CEA, NSE and PSA using Tb-QD FRET immunoassay. The narrow emission bands of QDs and the multiple sharp peaks of the Tb emission allowed the possibility for the multiplexed assay of different biomarkers in a sample. The large size of antibodies, their stoichiometry and position on the QD surface was a challenge to their use in immunoassay. Hence nanobodies which are smaller than antibodies were introduced in place of antibodies. This reduced the FRET distance and further improved the sensitivity of the assay. [17,265–267]

Su *et al.*,2022 reported a new system of nanobody immunoassay where the Tb labelled nanobody on QD is displaced by the analyte (EGFR) leading to the switch off the FRET signal. They attained 80 nM limits of EGFR detection which was 3-fold lower than the cut-off concentration.[268]

In this thesis, I used in a new Tb complex (CRF) for Tb-QD FRET immunoassay with nanobodies.

Chapter Three

3.1 Enhancing Near Infrared II Emission of Gold Nanoclusters via Encapsulation in Small Polymer Nanoparticles

Optical biosensing and imaging have played a vital role in biological and medical studies over the years. The challenges of dealing with biological materials such as tissues and cells are strong autofluorescence across the UV-Vis and NIR I region, light scattering at μm depths, high absorption in the UV and increased sensitivity to long UV exposure.[269–272] Because of this, developing new luminescent systems that absorb and emit at higher wavelengths is highly important.

The AuNCs described in this project absorb in the UV-Vis region and emit in the second near-infrared (NIR-II) window between 1000 and 1700 nm, where there is deeper light penetration of tissues, less light scattering, and negligible autofluorescence.[52,273] These compounds are very interesting for in-vivo imaging as they allow high-resolution image acquisition in deep living tissues. Despite the advantages mentioned above of AuNCs, their low brightness level hinders their application in tissue imaging.[29] The brightness of a fluorophore is the product of its extinction coefficient (ε) and quantum yield (QY); therefore, increasing the extinction coefficient of the AuNCs should increase their brightness.[274] Accumulating many fluorophores in a small space produces NPs with the summation of the ε of the individual fluorophores (e.g., $\varepsilon > 10^7\ M^{-1}\ cm^{-1}$ for 100 dyes with $\varepsilon > 10^5\ M^{-1}\ cm^{-1}$ each) and, by implication, higher levels of brightness.[32,275] The AuNCs were thus encapsulated in polymer nanoparticles to form AuNC-NPs containing different concentrations of AuNC per NP. Dodecanethiol-coated AuNCs were chosen because this coating makes AuNCs very hydrophobic, favouring their encapsulation inside polymer nanoparticles. Poly(ethyl-methacrylate) with 5% of carboxylate groups was selected because it demonstrated its ability to encapsulate hydrophobic dyes.[276–278] Polymer

NPs loaded with increasing amounts of the AuNCs at loadings up to 50 wt% were prepared through nanoprecipitation to accomplish bright NIR-II fluorescent nanoprobes. The size of the AuNC-NP depended on the AuNCs loading because the increase of AuNCs increased the lipophilicity of this system, making the resulting nanoparticles larger. It is noticeable that this size distribution may impact their biological properties as the biodistribution and bio application of NPs are highly dependent on the size of the NPs.[279–281] It was possible to evaluate the number of AuNCs per NP and to vary the distance between the AuNCs in an AuNC-loaded nanoparticle (AuNC-NP) (Figure 3.0).

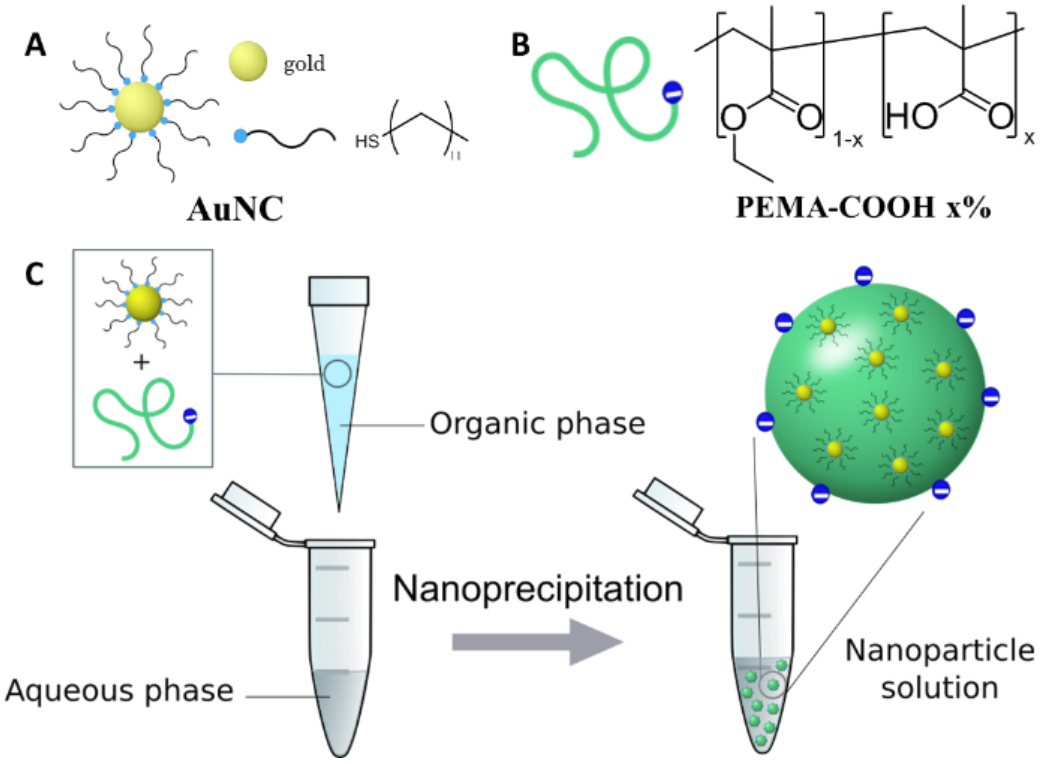

Figure 3.0 (A) Structure and representation of gold nanoclusters stabilised by dodecanethiol (AuNC). B) Structure and representation of the polymer. C) Principle of NP synthesis through nanoprecipitation

Varied AuNC-NP loading created the avenue for studying the influence of the local concentration and distance of NIR-II AuNCs on their photophysical properties. In particular, we observed a progressive shift of the PL emission to longer wavelengths with increased AuNC loading. Multi-wavelength PL lifetime measurements allowed us to assign this redshift to

growing interactions between the AuNCs within the NPs. To quantify the potential sensitivity and resolution of these NIR-II nanohybrids in biological media, we imaged them in capillaries at different depths of biological tissue models. Because of the reduced absorption and scattering in the NIR-II, the high NIR-II PL brightness (up to 3.8 x 10^6 M^{-1} cm^{-1}) of the nanohybrids and their bathochromic shift (>1250 nm) allowed fluorescence images at depths reaching 7 mm, which confirmed the immense potential of these NPs for advanced NIR-II imaging.

This work is a collaboration between the team of Andreas Reisch (Universite de Strasbourg), who prepared polymer nanoparticles, the team of Xavier Le Guevel (Universite de Grenoble), who provided a synthetic method to get NIR-II-emitting AuNCs and the team of Niko Hildebrandt (Universite de Rouen) in charge of optical properties studies.

My primary contribution to this work was the lifetime measurement and analysis of the encapsulated AuNCs. Here, we present spectroscopic and imaging evidence of two lifetimes originating from AuNCs. We assigned one lifetime to the Au^0 in the core of the cluster and the other to Au^1 interacting with S atoms on the shell, as previously stated in literature. We also ascribed the lifetimes and the different emission bands to interacting and non-interacting AuNC species in the AuNC-NPs. We propose that the changes in the emission band and lifetimes of the AuNCs result from homo-FRET between NCs or ligand to metal charge transfer (LMCT) from the S atoms of the dodecanthiol (DDT) ligand on the interacting NCs. Some other parts of the study, like the AuNC-NP imaging, are included in this chapter to give context to my contribution.

3.2 Materials and Methods

D_2O and Ethanol were the two solvents used for the optical characterisation of the samples.

The PL spectra were measured both in the Rouen and in Strasbourg with different spectrophotometers.

EPL 405 (Serial number: 083/405/11/11) with a pulse width of 56.3 ps and emission peak centred at 404.2 nm.

HPL 670 (Serial number: 010/670/04/21) with a pulse width of 104.4 ps and emission peak centred at 675.4 nm.

Fluorolog 3 Spectrometer equipped with UV-Vis 200-980 nm (PMT R13456) and IR (PMT H10330C-75) detectors (Horiba Instruments)

Cary 60 UV-Vis Spectrophotometer 200-1100 nm (Agilent Technologies)

3.2.1 Synthesis of Gold Nanoclusters (AuNCs)

AuNCs, stabilised by dodecanethiol (DDT), were prepared as described elsewhere.[282] Briefly, 46.4 mg (93.75 μmol) $AuClPPh_3$ were dispersed in ethanol, followed by the addition of 81.5 mg (0.94 μmol) tert-butylamineborane and fast stirring for 45 mins. The solution changed from orange-red to black colour after 5 min. Then 12 μL of DDT was added, and the mixture was left to stir for another 3 h. The dark solution was then filtered 3 times with filters at 3 kDa molecular weight cut-off to remove unreactive species and kept refrigerated.

3.2.2 Preparation of Polymer-loaded AuNC NPs

Polyethylmethacrylate (PEMA) bearing 5 mol% of methacrylic acid was synthesised through free radical polymerisation as described previously.[276,283] Stock solutions of PEMA were prepared at a concentration of 10 g L^{-1} in acetonitrile. These solutions were diluted to 2 g L^{-1} in acetonitrile, with 9 to 50 wt% of AuNCs (relative to the total mass of polymer and AuNC). These solutions were quickly added to a nine-fold volume excess of phosphate buffer (20 × 10−3 m, pH 7.4) under shaking (Thermomixer comfort, Eppendorf, 1050 rpm at 21 °C), followed by further dilution to the desired concentration.

3.2.3 Optical Characterisation of AuNC-NPs

The different loadings of AuNC-NPs and AuNC were diluted in D_2O and ethanol, respectively, to 0.1 mg/mL. The AuNC-NPs were vortexed briefly, and the AuNCs' samples were sonicated for 5 minutes before measurement.

3.2.3.1 Absorption Spectra Measurements

Absorption spectra were recorded on a Cary 60 UV-Vis spectrophotometer with a 0.5 cm pathlength quartz cuvette. 400 µL of D_2O was used for baseline and blank measurements when measuring the AuNC-NPs and equal volume of ethanol was used to measure the baseline and the blank when measuring the non-encapsulated AuNCs. 400 µL of 0.1 mg/mL of all samples were across from 190 to 1100 nm at moderate speed on the spectrometer. The absorption spectra were also measured in Strasbourg with Carry 5000 UV-Vis spectrophotometer.

3.2.3.2 Photoluminescence Spectra Measurements

The photoluminescence spectra were recorded on Fluorolog-3 (Horiba Instruments) equipped with an UV through Vis and NIR detectors using a CW 450 W Xenon lamp. The excitation and emission slits were set to 5 nm for Vis detector and 14 nm for NIR detector. The PL spectra was measured separately on the UV-Vis and IR detectors and the spectra were joined to obtain a full PL spectrum. In Strasbourg, the PL spectra was also measured using a WP NIR1 spectrometer (Wasatch Photonics) using 405 or 730 nm lasers from LCC Oxxius as excitation sources.

3.2.3.3 Excitation Spectra Measurements

The excitation spectra of the samples were measured on Fluorolog-3, a spectrophotometer from Horiba. The prepared samples were put in capillary tubes to reduce the pathlength that light has to travel through the sample and in consequence reduce the scattering of light by the samples. The emission spectra were set at 1050 nm and the excitation spectra were measured from 360-

1000 nm on the Infrared (T1) detector. The excitation slit was set at 3nm while the emission slit was set at 8nm. The excitation spectra were corrected by dividing the excitation signal by the corrected lamp signal (T1/R1c). An empty capillary tube was also measured as the blank. T1/R1c of the blank was subtracted from T1/R1c of the sample to obtain the true signal of the samples.

To compare peak ratios (*R*) of excitation and absorption spectra (measured on a Cary 60, Agilent Instruments, in quartz cuvettes with 0.5 cm path length), the average intensities from 404 to 406 nm were divided by the average intensities from 669 to 671 nm:

$$R = \frac{avg\ int.(404-406\ nm)}{avg\ int.(669-671\ nm)} = \frac{A}{B} \qquad (13)$$

Errors were calculated by error propagation:

$$\Delta(R) = \sqrt{\left(\frac{a}{A}\right)^2 + \left(\frac{b}{B}\right)^2} \times R \qquad (14)$$

where a is the standard deviation of A and b is the standard deviation of B.

3.2.3.4 Lifetime Measurements

PL lifetimes were measured on a Fluorolog-3 with 400 µL of samples in quartz cuvettes with a 0.5 cm path length. PL decay curves were measured at three emission wavelengths, namely 950 nm, 1050 nm, and 1200 nm, using two different picoseconds pulsed diode lasers from Edinburgh Instruments: 1. EPL 405 with a pulse width of 56.3 ps and emission peak centred at 404.2 nm; 2. HPL 670 with a pulse width of 104.4 ps and emission peak centred at 675.4 nm. The lasers were set at a repetition rate of 200 kHz (5 µs pulse period). When measuring with EPL 405 nm, the emission slit was set to 30 nm. When measuring with HPL 670, the emission slit was set to 58.8 nm (fully open) because the absorption in the 675 nm spectral region is at least 3 times lower than the one at 404 nm.

In Datastation software (Horiba), time-correlated single-photon counting (TCSPC) was set for 3.34 ns per channel and 1000 channels. The measurement was set to end upon counting 20,000 photons as the maximum value. Decay curves were fit using FAST software (Edinburgh Instruments). The exponential components analysis routine was used to do the biexponential fitting of the curves. The fitting range was from channels 3 to 650 for measurements using EPL 405 and from channels 5 to 650 for measurements using HPL 670. Biexponential fitting (Equation 15) was found sufficient for good fits of the decay curves.

The fitting range did not exceed 650 channels to avoid fitting the background with the decay as the signal to background ratio was low due to the low brightness of the samples in comparison with the thermal signal of the IR detector after channel 650. The biexponential fitting fit the decay curves well and the addition of a 3rd component to the fit provided no new information.

$$I(t) = X_1 e^{\frac{-t}{\tau_1}} + X_2 e^{\frac{-t}{\tau_2}} + C \qquad (15)$$

Relative amplitudes x_1 and x_2 amplitude-averaged lifetimes $\langle\tau\rangle$ were calculated from the resulting exponential data as follows:

$$x_1 = \frac{X_1}{X_1 + X_2} \qquad (16)$$

$$x_2 = \frac{X_2}{X_1 + X_2} \qquad (17)$$

$$\langle\tau\rangle = x_1\tau_1 + x_2\tau_2 \qquad (18)$$

In these equations, X_1 and X_2 are amplitudes of the first and second-lifetime components τ_1 and τ_2, respectively; C is the background intensity, and I(t) is the time-dependent PL intensity. Lifetime errors were estimated as 10 % relative errors.

3.2.3.5 Correction of Decay Curves

For an excitation-independent comparison of the decay curve intensities, the decay curves were normalised to a constant number of excitation pulses and to constant absorbance values of the sample. The pulse number is the product of the measurement runtime and the repetition rate of the laser (200 kHz). The average absorbance between 404 and 406 nm and 669 and 671 nm was normalised to the absorbance of the 9 wt% sample. The pulse numbers were normalised to the pulse number of the 9 wt% sample. The decay curves were then multiplied by the normalised number of pulses and divided by the normalised absorption at the wavelength of interest. The background (last intensity point of the decay curve) was then subtracted to receive background-corrected decay curves. The channel numbers were multiplied by the 3.34 ns to obtain the time scale on the x-axis of the decay curve.

3.3 Results

The first results presented here contains my original findings and contributions to the research. Absorption and Emission spectra that were measured in Strasbourg are also mentioned in these parts.

3.3.1 Spectroscopic Properties

3.3.1.1 Absorption Spectra

The AuNC-NPs showed broad absorption from UV to the NIR with two main peaks around 415 nm and 708 nm, similar to the spectrum of the clusters in organic solvent. While absorbance increased with loading, the shape of the spectra remained the same. The relative absorbance spectra were obtained by normalising the peak at 415 nm for the highest loading (50 wt%) to 1. The absorbance of the AuNCs in ethanol showed slight hypochromic shift of the peak at 708 nm. The absorbance spectra on Carry 5000 in Strasbourg showed similar spectra with only half the intensities. This could be because the NCs were dispersed in phosphate buffer in Strasbourg

while my samples were diluted with deuterated water. This however would require further investigations. (Figure 3.1)

The extinction coefficient of the AuNCs from independent absorption measurements was around 14000 $M^{-1}cm^{-1}$ at 730 nm and a five times higher value of 70000 $M^{-1}cm^{-1}$ at 405 nm. The particle extinction coefficients at the two major absorption wavelengths, around 1×10^9 M^{-1} cm^{-1} (at 405 nm) and 2×10^8 M^{-1} cm^{-1} (at 730 nm), were calculated from the estimated number of AuNCs per NP and the extinction coefficient of the AuNCs alone.

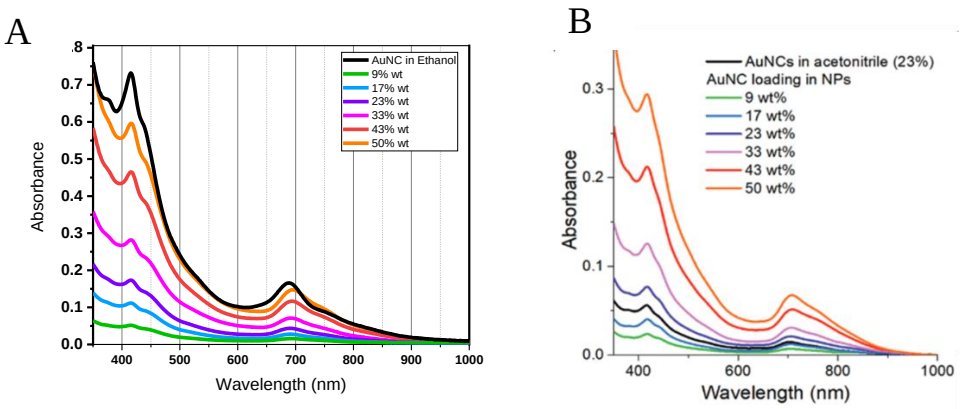

Figure 3.1 Absorbance spectra (A) Cary 60 (B) Cary 5000. Orange: 50 wt%, red: 43 wt%; magenta: 33 wt%; purple: 23 wt%; blue: 17 wt%; green: 9 wt%; black: AuNCs

3.3.1.2 Excitation Spectra

An excitation spectrum is acquired by fixing the detection monochromator at a given wavelength (1050 nm, emission peak) while moving the excitation monochromator. Therefore, this technique allows the determination of the absorption wavelength responsible for the luminescence. However, the absorption spectra measured on the UV-Vis spectrophotometer can combine absorption and scattering. The scattering of nanoparticles can become prominent while measuring the excitation spectra, making choosing an excitation wavelength difficult. Hence, the measured excitation spectra differ greatly from the absorption spectra.

The initial excitation spectra measurement showed no similarities with the absorption spectra due to excessive excitation light scattering from the nanoparticles. The shape of the raw excitation signals was in fact similar with that of the lamp signal (Figure 3.2A & B). The lamp corrected signal in Figure 3.2C showed a small peak around 400 nm which gave the clue of the presence of the excitation band covered by the lamp signal. Hence, the pathlength of light travel through the sample was reduced by putting the samples in capillary tubes as shown in (Figure

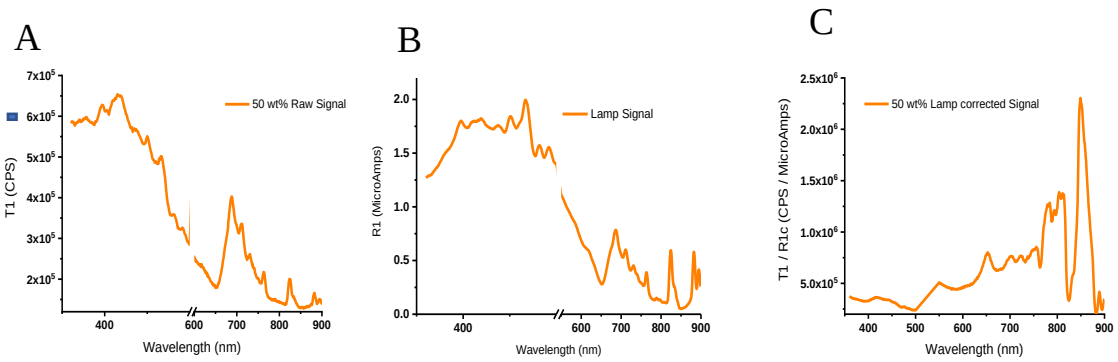

Figure 3.2. Excitation spectra of AuNC-NPs at 50% wt loading (A) Raw uncorrected signal (B) Xenon Lamp signal (C) Lamp corrected signal

The true excitation spectra were measured by subtracting the lamp spectra (equivalent to the scattered light) from the excitation spectra containing both the scattered and excitation spectra (Figure 3.3B & C).

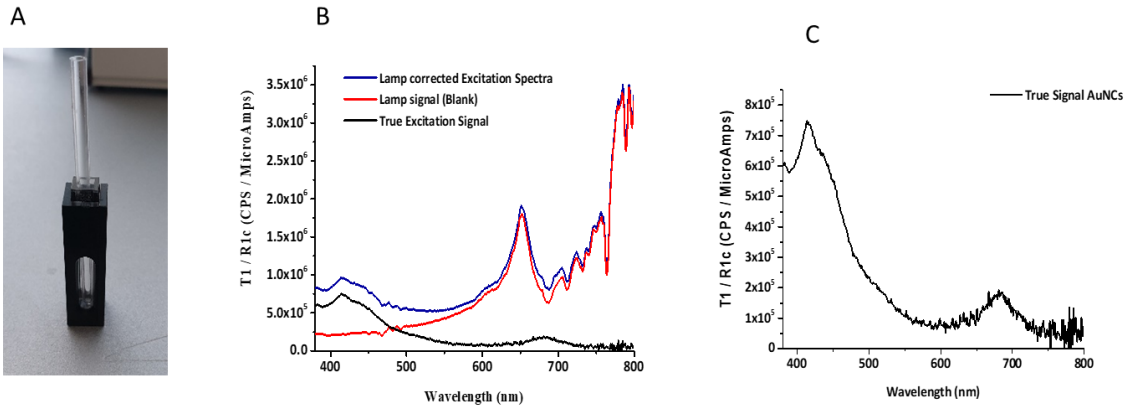

Figure 3.3 (A) Picture of Capillary tube in cuvette set up (B) PL excitation spectra of AuNCs in Ethanol. Blue: AuNC spectra + scattering. Red: Lamp spectra. Black: Difference between Black and Red, true excitation spectra (C) Enlarged PL excitation spectra of AuNC

The new measurements showed lesser scattering and the true excitation spectra which is similar to absorption. The ratio between both peaks was similar for both the absorption and excitation spectra and was quite constant across loading (Figure 3.4), further affirming the similarities between both spectra. It also proves that the absorption peaks are similarly affected by loading and that scattering remains negligible when considering the true excitation spectra.

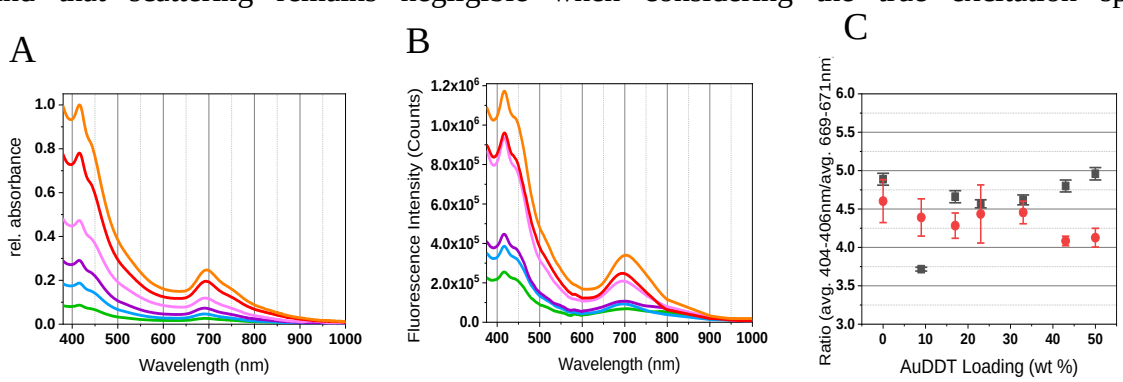

Figure 3.4 (A) Relative absorption spectra of AuNC-NPs. (B) PL excitation spectra of AuNC-NPs. Black: AuNCs Orange: 50 wt%, red: 43 wt%; magenta: 33 wt%; purple: 23 wt%; blue: 17 wt%; green: 9 wt%. (C) Absorption (black) and excitation (red) ratios of the average intensities of 404-406 nm and 669-671 nm as a function of the wt% of AuDDT in NPs

The 700 nm peak is generaly attributed to the AuNC core, while the 400 nm peak can originate from d to s orbitals interband transitions and from AuNC surface via ligand–metal interactions (400 nm excitation).[142,284,285] Thus, PL kinetics were investigated using two different excitation lasers with wavelengths of 404 and 675 nm.

3.3.1.3 Photoluminescence Spectra

The PL spectra of the NPs were measured on a Fluorolog-3 equipped with a NIR detector. Unfortunately, the emission maximum of AuNCs is in the transition region between our UV-Vis detector and our NIR detector in a range in which both detectors feature low sensitivity. Therefore, full spectra were obtained by merging the spectra measured from both detectors (Figure 3.5). Excitation of the core at 670 nm or the shell of the AuNCs at 405 nm did not change the shape of the emission spectra. The PL emission peak of unencapsulated AuNCs in ethanol was around 950 nm.

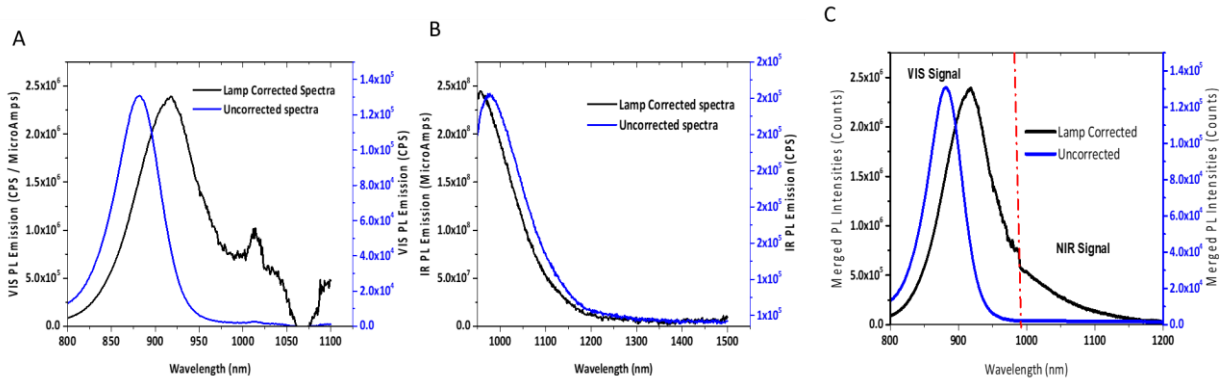

Figure 3.5 PL emission spectra of AuNCs in Ethanol measured on Fluorolog 3. Black: Uncorrected spectra. Blue: Instrument Corrected spectra (A) Spectra on UV-Vis detector (B) NIR detector (C) Merged Vis-NIR spectra

The PL emission of the AuNC-NP with the NIR detector gave a non-gaussian shape with a steep slope at the beginning of the spectra (Figure 3.6A). This gave the clue of the emission in the far-red region of the Vis range and prompted the launch into measurement of the emission in the Vis region. The peak for 50 wt% loading AuNC-NPs was found at 1010 nm after smoothing the spectra with Savitky-Golay method at 200 windows to 2 points on Origin 2018 software (Figure 3.6B). Measurement of the spectra on Fluorolog 3 spectrometer was highly tasking and required a lot of optimisation because the emission spectra were on the limit of the Vis and IR detectors where the correction factors were high and affected the reliability of the measured spectra. Hence, the PL emission from the WP NIR1 spectrophotometer in Strasbourg were preferred as the actual PL spectra of the NPs. The deconvolution of these spectra data from WP NIR1 showed four major peaks of interest (Figure 3.6C). The PL emission and normalised emission from WP NIR 1 also showed that the intensity of the spectra did not change with loading around 900 nm emission but showed a bathochromic increase with loading around 1000 nm (Figure 3.7B). This result initiates the investigation into the possibility of different emitting species. My measurement already showed that unencapsulated non-interacting AuNC in ethanol are responsible for the unchanging peak around 900 nm and by deductive reasoning, the species causing the bathochromic increase are AuNCs interacting in the NP confinement.

Though my spectra were difficult to obtain, they were quite similar with those measured at Strasbourg with an ocean optic USB detector (CCD detector 200-1600 nm) and the extra information from the Vis detector (from 800 – 950 nm) provided evidence for the possible energy transfer between AuNCs implied in the PL lifetime analysis (section 3.3.3.4). PL spectra of the AuNC loaded NPs showed a broad PL emission starting around 850 nm and reaching up to 1500 nm, achieving the objective of synthesising NIR-II-emitting nanohybrids.

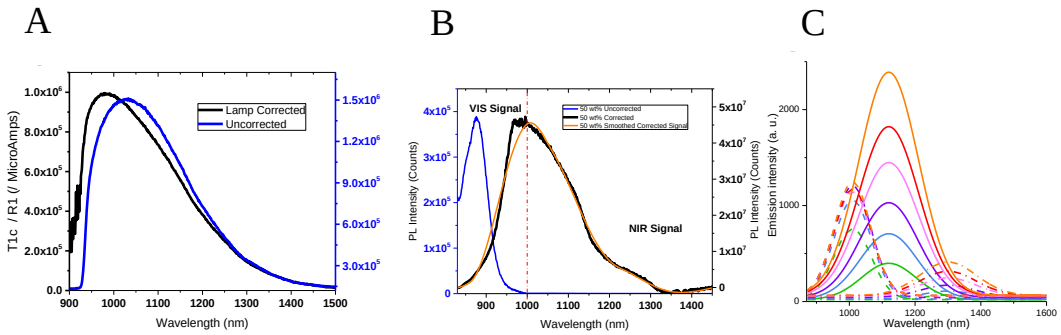

Figure 3.6 PL emission spectra of AuNC-NP 50 wt% in D_2O on Fluorolog 3. Black: Uncorrected spectra. Blue: Instrument Corrected spectra; Orange: smoothed PL emission (A) Spectra on NIR detector (B) Merged Vis-NIR spectra (C) Deconvoluted PL spectra for all loadings (orange: 50 wt%, red: 43 wt%; magenta: 33 wt%; purple: 23 wt%; blue: 17 wt%; green: 9 wt%)

The influence of solvents was considered from the onset of the synthesis in Strasbourg when studying photophysical properties in the NIR-II because H_2O has various absorption peaks in the emission range of the NPs, which are absent for D_2O (Figure 3.7A). Comparison of the absolute PL emission of NPs (Figure 3.7C, inset) revealed that the shape of the PL emission spectrum changes between the two conditions, in particular with a decrease of the measured intensity in H_2O in the regions 930–1050 and 1100–1250 nm, corresponding to the absorption of water (Figure 3.7A). The slight difference observed between the two aqueous media suggests that the clusters are well trapped inside the polymer matrix and have limited contact with the solvent. Together, these results indicated that the differences in the PL spectra stem mainly from the absorption of the emitted PL by H_2O and not from interactions of H_2O with the encapsulated AuNCs. The same results were obtained for NPs prepared in D_2O and

subsequently transferred to H_2O, indicating that preparation in D_2O did not alter the particles. Hence, all experiments were realised in deuterated water to remove solvent bias from the study.

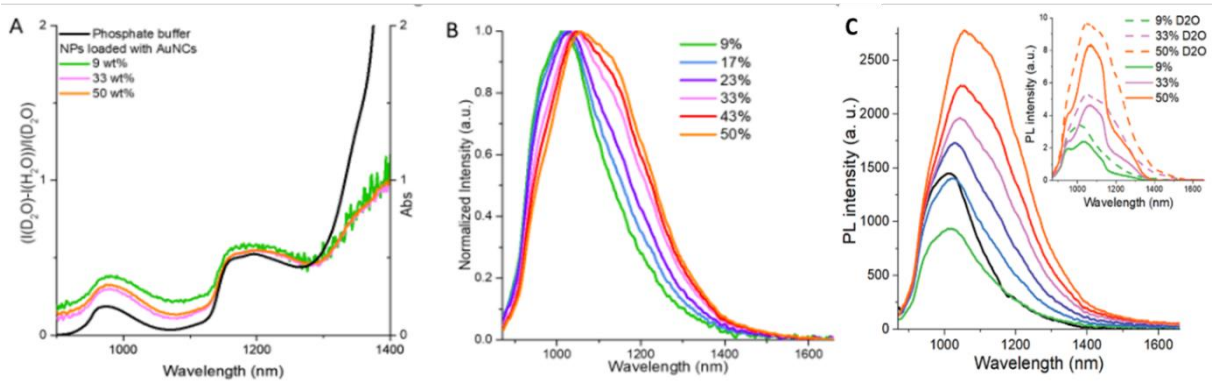

Figure 3.7 (A) In black: absorption spectrum of phosphate buffer in the 900 – 1400 nm range. In colour: Normalised difference between emission spectra recorded in D_2O and H_2O for solutions of NPs loaded with different amounts of AuNCs (λ_{ex} = 730 nm). (B) Normalised PL emission spectra of NPs loaded with different amounts of AuNCs (λ_{ex} = 730 nm). (C) PL spectra of PEMA-COOH 5% NPs loaded with different amounts of AuNCs (λ_{ex} = 730 nm). Inset of (C): Comparison of PL spectra in deuterated and nondeuterated media

3.3.1.4 Lifetime Measurements

PL decay measurements were conducted at 950 and 1050 nm for the short wavelength range and at 1200 nm for the long wavelength range. The wavelength of 1200 nm was chosen because it is significantly separated from the short wavelength peaks and still provides sufficient PL intensity for kinetic analysis. Accordingly, PL kinetics were investigated using two different excitation lasers with wavelengths of 404 nm for the NC shell (Figure 3.8) and 675 nm for the NC core (Figure 3.9). The raw PL decays had to be normalised and corrected to obtain the true PL kinetics of the NPs. It was necessary to remove the thermal background signal by the NIR detector and correct for absorption and excitation backgrounds.

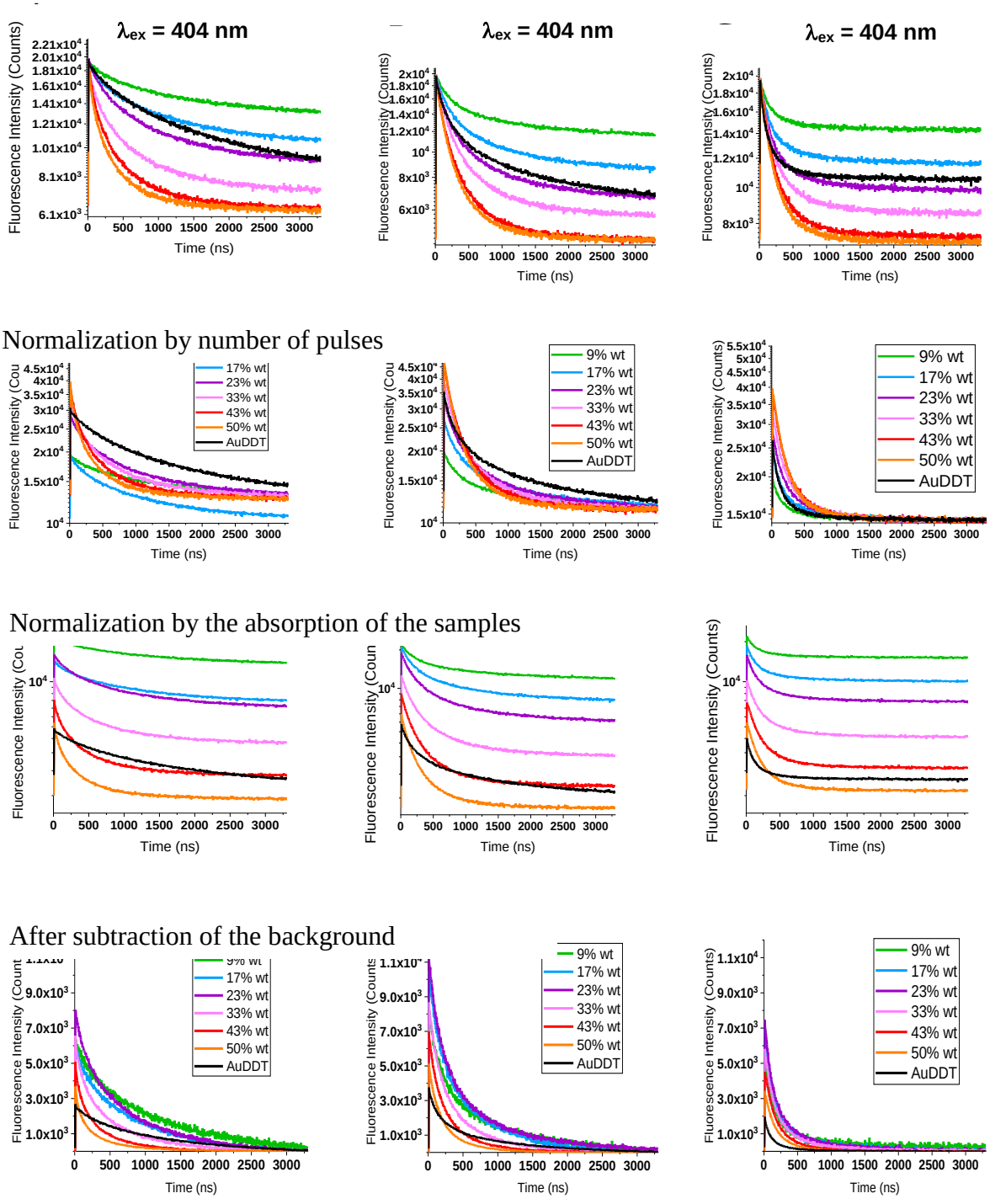

Figure 3.8 Raw PL decays and different normalisation (First row: Raw PL decay; Second row: excitation pulse normalised; Third row: excitation pulse and absorption normalised; Fourth row: excitation pulse and absorption normalised with background subtraction of PL decay curves) of AuNCs (in ethanol) and AuNC-NPs (in D_2O) for excitation (λ_{ex}) at 404 nm and emission (λ_{em}) at different wavelengths (A: 950 nm, B: 1050 nm, and C: 1200 nm) PL decays (black: AuNCs; orange: 50 wt%, red: 43 wt%; magenta: 33 wt%; purple: 23 wt%; blue: 17 wt%; green: 9 wt%).

PL decay from both excitation wavelengths (Fgure 9 & 10) showed similacurve patterns before and after correction proving once again that the excitation wavelength did not affect the PL kinetics.

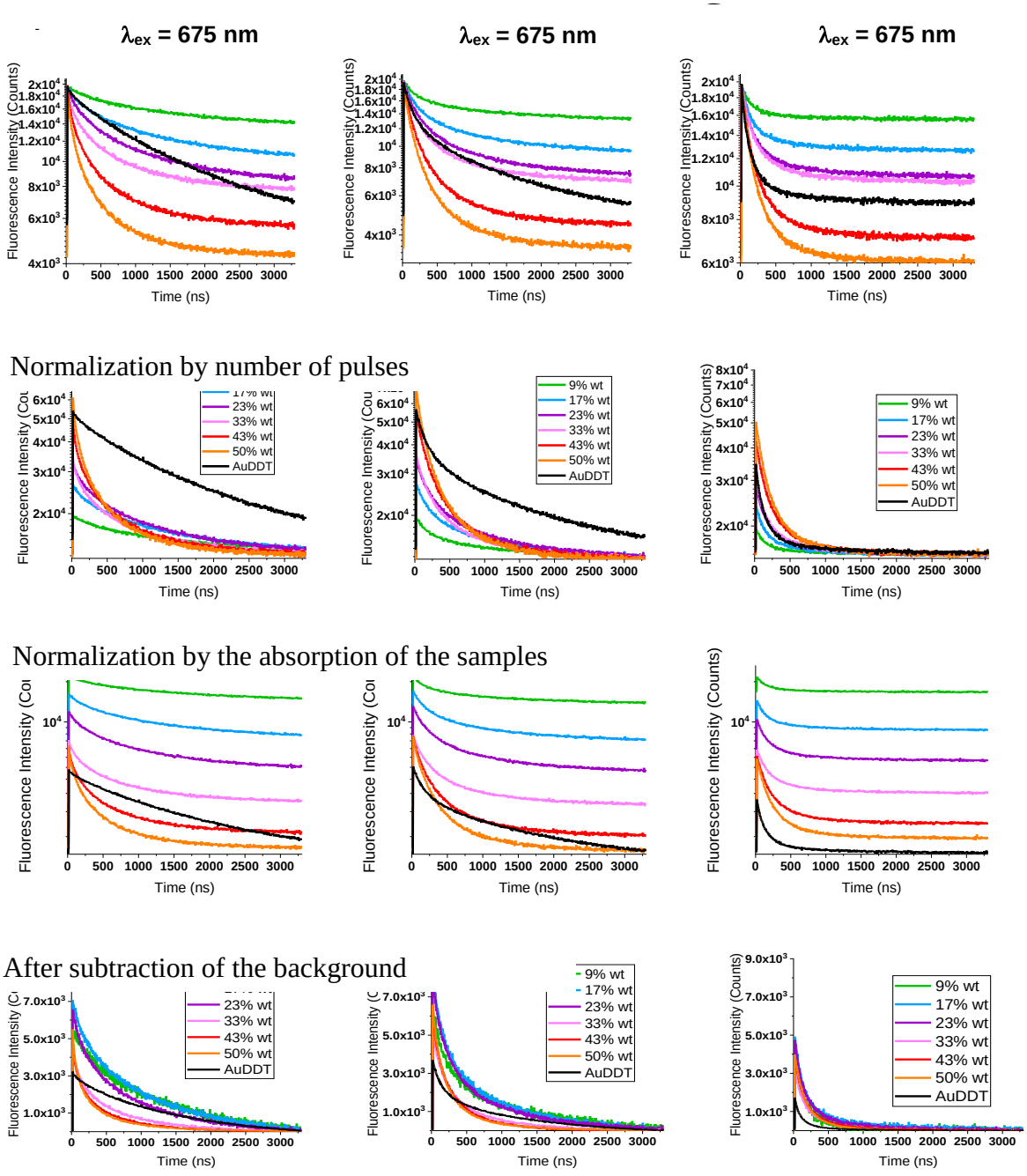

Figure 3.9 Raw PL decays and different normalisation (First row: Raw PL decay; Second row: excitation pulse normalised; Third row: excitation pulse and absorption normalised; Fourth row: excitation pulse and absorption normalised with background subtraction of PL decay curves) of AuNCs (in ethanol) and AuNC-NPs (in D_2O) for excitation (λ_{ex}) at 675 nm and emission (λ_{em}) at different wavelengths (A: 950 nm, B: 1050 nm, and C: 1200 nm) PL decays (black: AuNCs; orange: 50 wt%, red: 43 wt%; magenta: 33 wt%; purple: 23 wt%; blue: 17 wt%; green: 9 wt%).

Each PL decay was found to be multiexponential, modelled with two- very distinct components allowed to describe properly this system. To rationalise these measurements the lifetimes and the contributions of these lifetimes were plotted depending on the loading of AuNC-NP (Figure 11); in this graph we also introduced a 0% loading which corresponds to the decays of AuNC in ethanol without polymer nanoparticles. The multiexponential photoluminescence (PL) decays of AuNC-loaded polymer NPs (Figure 3.10, top) exhibit distinct concentration-dependent behaviours for different emission wavelengths. The 950 nm emission displays a prominently longer decay time component, while the 1200 nm emission primarily shows faster decays, and the 1050 nm emission decay behaviour lies between the two. This phenomenon is very obvious when decay times (Figure 3.10, center) and amplitude fractions (Figure 3.10, bottom) are plotted in function of the loading. The 1200 nm emission remains insensitive to AuNC concentrations, maintaining stable average PL lifetime with two unchanged lifetimes and amplitude fractions. The emission of AuNC at 10% loading is similar to the one of pure AuNCs (0 wt%) measured in ethanol showing that polymer is protecting AuNC from quenching by the solvent while self-quenching is still weak at this loading. The 950 nm and 1050 nm PL decays also exhibit two distinct lifetimes, with the shorter lifetime stable over the entire AuNC concentration range and corresponding well to the one at 1200 nm. However, the longer decay time decreases toward the value at 1200 nm with increasing AuNC loading. The long lifetime component is significantly stronger for the 950 nm decay compared to the 1050 nm, indicating that the influence of AuNC loading is stronger for shorter wavelengths. This trend is evident in the amplitude-averaged PL lifetimes. These results align with steady-state spectroscopy, indicating that the redshift of AuNC NPs with increasing concentration results from a stronger PL decrease at shorter wavelengths.

Notably, at high AuNC loading (50 wt%), single and amplitude-averaged PL lifetimes are similar for all emission wavelengths and the long PL lifetime is quenched by comparison with other loadings. This behaviour is related to a decreasing of the distance between AuNCs with increasing loading. This effect is not observed at the longest PL wavelengths (1200 nm) which exhibits both a long (≈400 ns) and short (≈100 ns) lifetime component remaining unchanged with AuNC loading. Considering the weak PL intensity at 1200 nm for AuNCs in solution and its reduced quenching compared to shorter wavelength PL intensity with increased loading, longer PL wavelengths are attributed to strongly interacting AuNCs. Shorter PL wavelengths (<1200 nm) show a relatively strong long (>1 μs) decay component with a weak short (≈100 ns) component. The very long decay component is longest and strongest for AuNCs in solution. With increased AuNC loading, it is progressively quenched, reaching ≈400 ns, representing strongly interacting AuNCs at 1200 nm. Therefore, shorter wavelengths mainly present non-interacting or weakly interacting AuNCs (as suggested earlier in the PL emission spectra), whose fraction decreases with increasing loading due to shorter inter-AuNC distances within the NPs. The differences in luminescence decays at short (950 and 1050 nm) and long (1200 nm) emission wavelengths for lower AuNC loading (<50 wt%) and the redshift of PL with increasing AuNC concentration can be attributed to increasing AuNC interactions favouring longer wavelength PL emission over shorter wavelength PL emission.

Intriguingly, only the longer PL lifetime component is influenced by AuNC loading, while the shorter component remains more or less constant (≈100 ns) for all emission wavelengths and AuNC loadings (Figure 3.10, center). This specific property of the AuNC NPs may be explained by the different origins of AuNC emission. Considering the weak spectral overlap of AuNC emission and absorption, homo-FRET would require very short donor–acceptor distances (≈1 to 2 nm). With an AuNC radius of approximately 1 nm, FRET from AuNC surfaces would be

favoured over FRET from AuNC cores. At very close distances, other energy transfer mechanisms, such as Dexter or electron transfer, may become more probable than FRET and would only occur between AuNC surfaces. Thus, the constant short PL lifetime component mainly represents PL originating from the AuNC core, while the quenched long component represents the ligand-metal charge-transfer related PL originating from the AuNC surface.

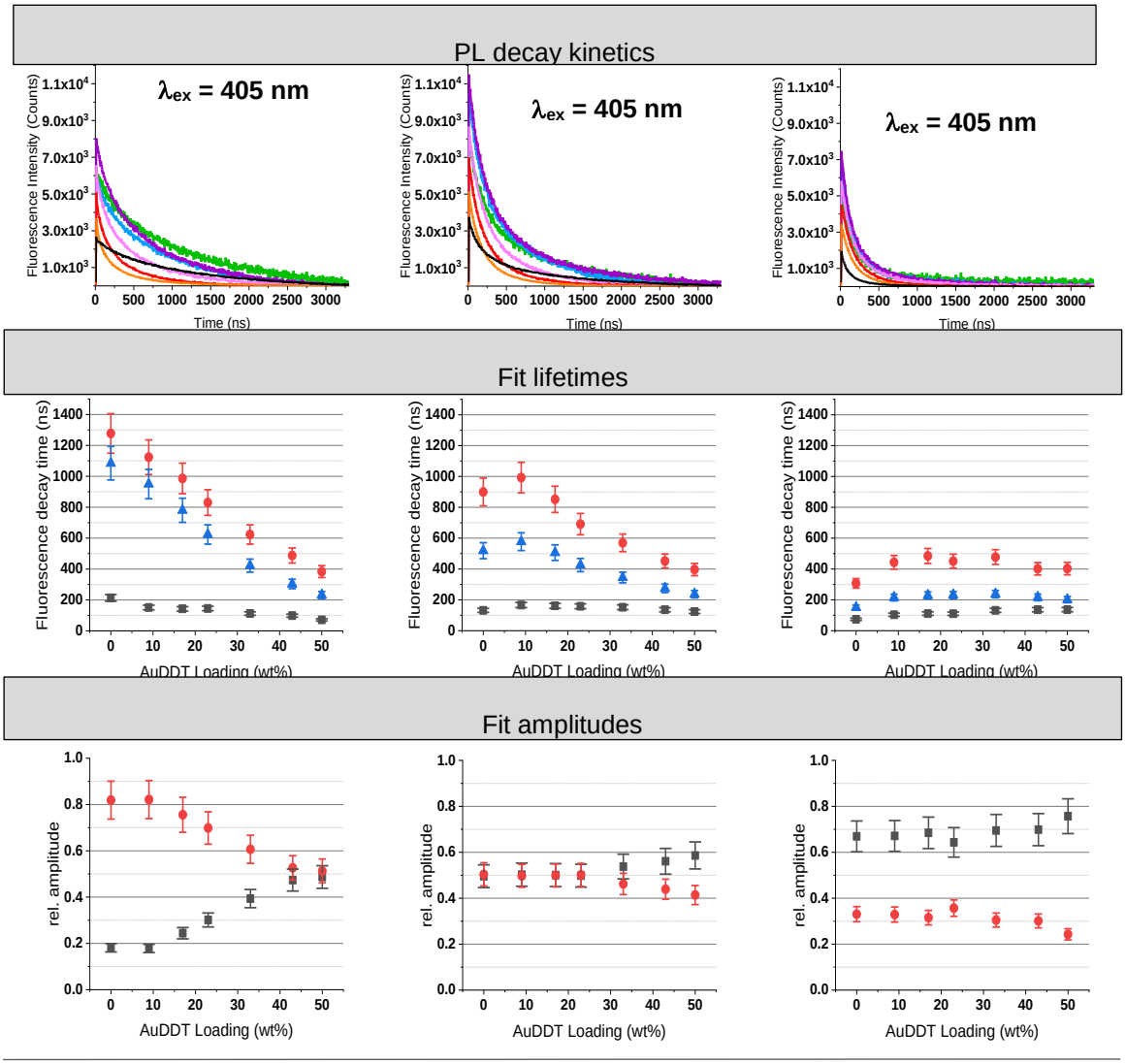

Figure 3.10 Intensity-comparable (the curves from each graph were normalised for similar excitation intensity and similar absorption and background was subtracted) PL decays (top row - black: AuNCs; orange: 50 wt%, red: 43 wt%; magenta: 33 wt%; purple: 23 wt%; blue: 17 wt%; green: 9 wt%), fit PL decay times (black: τ_1; red: τ_2; blue: $<\tau>$), and fit amplitude fractions (black: x_1; red: x_2) of AuNCs (in ethanol) and AuNC-NPs (in D_2O) for excitation (λ_{ex}) at 404 nm and emission (λ_{em}) at different wavelengths (A: 950 nm, B: 1050 nm, and C: 1200 nm). 0 wt% loading corresponds to AuNCs in ethanol.

Table 2 Summary of characteristics of AuNC-loaded polymer NPs

Loading AuDDT (%)	Size in DLS (nm)	Size in TEM (nm)[a]	Number of AuNCs per NP[b]	AuNC distance inside NPs[c] (nm)	ε_{NP} 730nm ($M^{-1}.cm^{-1}$)[d]	ε_{NP} 405nm ($M^{-1}.cm^{-1}$)[d]	Quantum Yield (%)[e]	Brightness 730 nm $M^{-1}.cm^{-1}$[f]	Brightness 405 nm ($M^{-1}.cm^{-1}$)[f]
9	30 ± 3	26 ± 5	120	2.6	1.7×10^6	8.77×10^6	1.3	2.3×10^4	1.1×10^5
33	49 ± 6	41 ± 9	2300	1.4	3.3×10^7	1.68×10^8	0.6	2.0×10^5	9.9×10^5
50	68 ± 6	60 ± 13	14000	1.1	2.0×10^8	1.03×10^9	0.4	7.6×10^5	3.8×10^6

a: Average size of > 200 NPs ± width at half maximum.

b: Estimated based on equation 3.

c: Estimated based on equation 4.

d: Calculated according to ε_{NP} = Number of AuNCs * ε_{AuNC}.

e: Measured using IR1061 as reference.

f: Calculated according to brightness = ε_{NP} x QY.

The cluster concentration in the NP helped us estimate the distances between clusters at different NC loading. These distances were highly linked to the loading and the highest loading 50 wt% was half the estimated distance between clusters in the lowest loading of 9 wt% (Table 1). At 50 wt% loading, an average nearest distance of 1.1 and 2.6 nm at 9 wt% is estimated assuming an isotropic random distribution. Hence, there is more NC cluster interactions due to the short distances between NCs with increased loading.[130]

Interestingly, excitation at 675 nm (instead of 404 nm) results in very similar PL decay kinetics (Figure 3.11), including PL lifetimes and amplitude fractions. These findings indicate no difference in exciting the AuNCs in the short or long wavelength absorption band, and there is no excitation-wavelength dependent emission of the AuNC core or ligand-metal-surface states. While this result contradicts previous studies, it is important to note that size distribution and the nature of the ligand often significantly impact PL emission properties, notably in the NIR region. These results offer a new perspective on interaction-dependent AuNC emission

behaviour, and further studies with detailed and comprehensive AuNC PL characterisation of various AuNCs will be necessary.

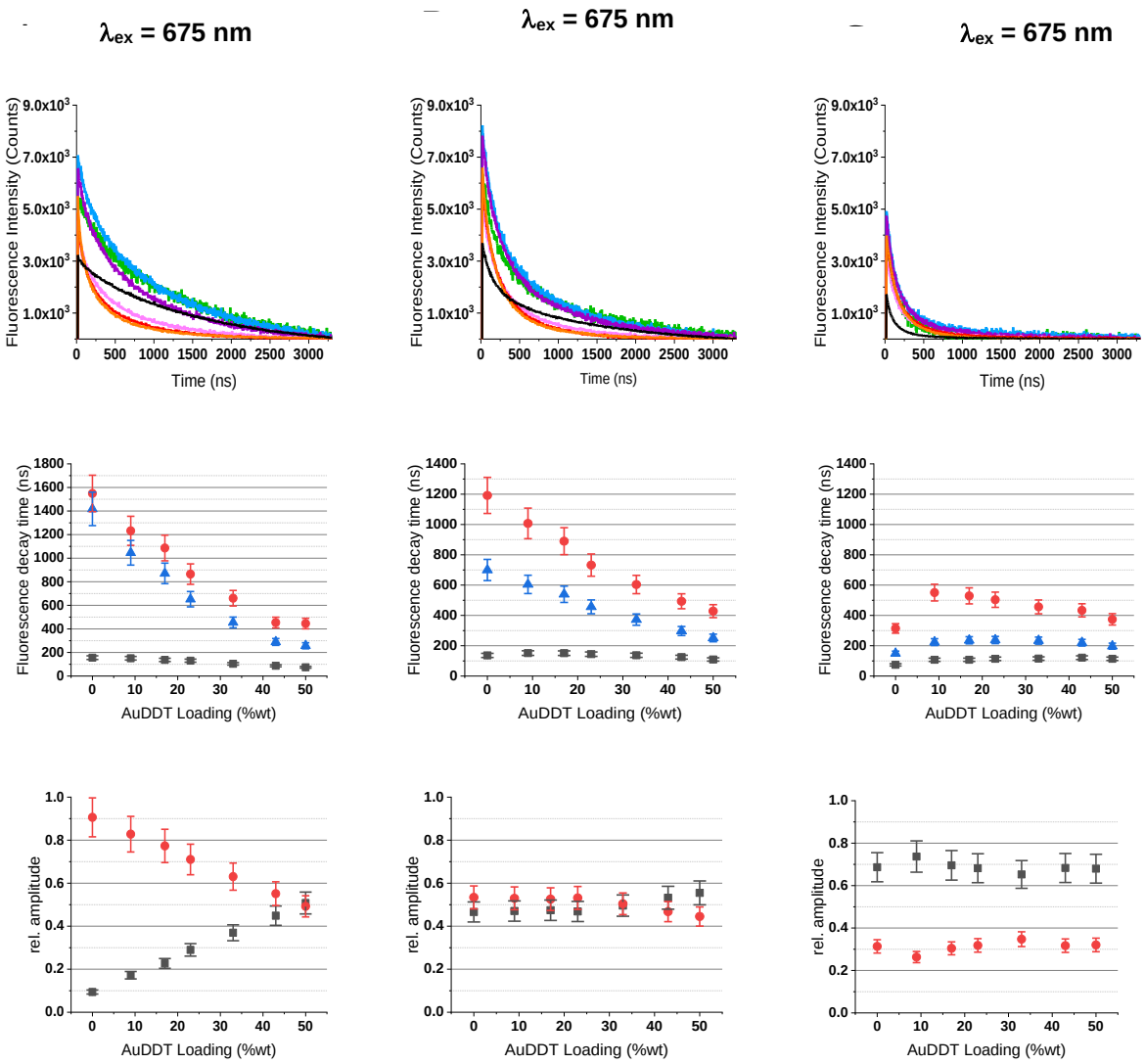

Figure 3.11 . Intensity-comparable (the curves from each graph were normalised for similar excitation intensity and similar absorption and background was subtracted) PL decays (top row - black: AuNCs; orange: 50 wt%, red: 43 wt%; magenta: 33 wt%; purple: 23 wt%; blue: 17 wt%; green: 9 wt%), fit PL decay times (black: τ_1; red: τ_2; blue: $<\tau>$), and fit amplitude fractions (black: x_1; red: x_2) of AuNCs (in ethanol) and AuNC-NPs (in D_2O) for excitation (λ_{ex}) at 675 nm and emission (λ_{em}) at different wavelengths (A: 950 nm, B: 1050 nm, and C: 1200 nm).

3.4 Conclusions

So far, we developed polymer nanoparticles NPs loaded with high concentrations of gold nanoclusters emitting in the NIR-II spectral region. Efficient encapsulation within the polymer matrix allowed the creation of NPs, each containing over 10,000 clusters and measuring about 60 nm. Despite a slight aggregation-caused quenching (ACQ) effect, relatively good quantum yields were achieved even at high AuNC loadings. This resulted in outstanding particle PL brightness for the NIR-II region, reaching approximately 4×10^6 M^{-1} cm^{-1}, positioning our nanohybrids among the brightest NIR-II emitters. The absorption and excitation spectra of both AuNCs in ethanol and AuNC-NPs in D_2O were very similar and showed two peaks of interest, which agrees well with the literature. The similarity also proved that the extinction measured using the UV-Vis spectrometer is mainly absorption and that scattering is negligible in these samples. Both peaks increased with increased loading of AuNCs in AuNC-NP for excitation and absorption spectra. The increased intensity with loading implies that increasing the amount of AuNCs in the AuNC-NPs increases the true absorption coefficient of the NPs.

The ratio between both peaks was similar for both the absorption and excitation spectra and was quite constant across loading, further affirming the similarities between both spectra. It also proves that the absorption peaks are similarly affected by loading and that scattering remains negligible.

The high AuNC concentrations within the particles enabled the study of PL properties at very small intercluster distances. Surprisingly, a bathochromic shift in the PL emission with loading was observed. Spectral deconvolution and time-resolved PL measurements revealed different sensitivities of various emission modes to interactions between clusters. While emission from the Au core was minimally affected by the distance between clusters, emissions involving ligand–metal surface states experienced a relatively strong ACQ effect. The lifetime

measurements further revealed the behaviour of the NIR-II emitting AuNC when encapsulated. We hypothesise that the longer lifetimes (mostly affected by loading and cluster proximity) originate from the surface of the AuNCs. In comparison, the shorter lifetimes (unaffected by loading) originate from the core of the AuNCs as described in Figure 3.12.

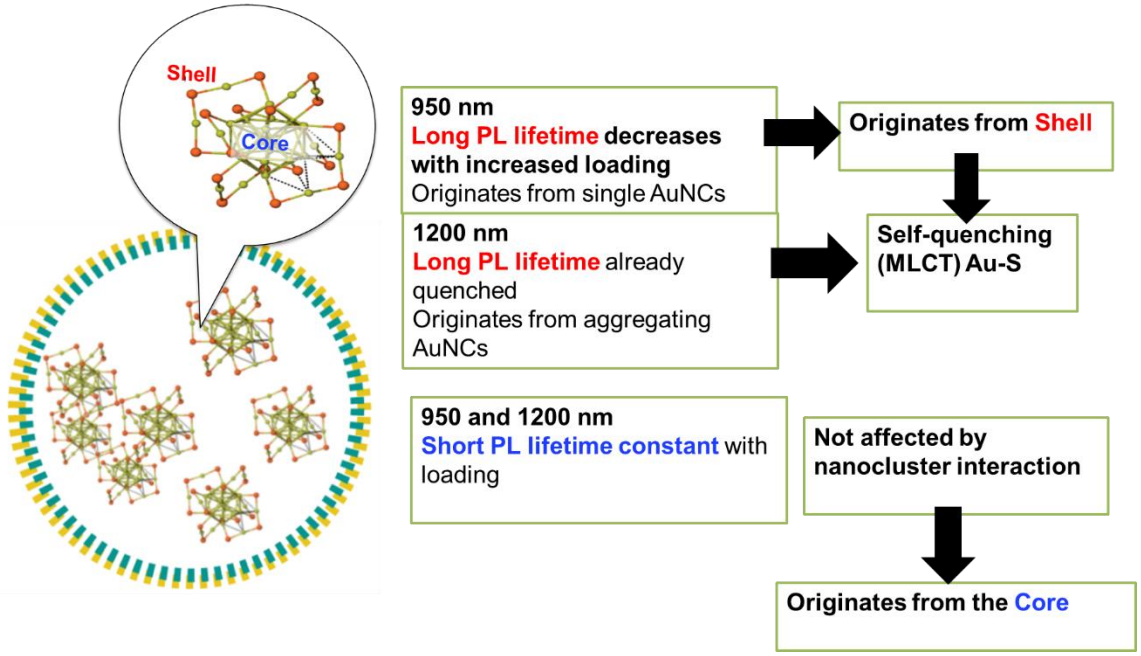

Figure 3.12 Scheme of AuNCs-NP PL Kinetics summary

Consequently, the PL maximum shifted to longer wavelengths at higher loadings, extending further into the NIR-II region. These results indicated that precise engineering of distances and interactions among AuNCs can optimise and tailor their PL properties. The combination of very high PL brightness, well-characterised PL behaviour, and excellent performance in tissue models positions the developed nanohybrids as ideal candidates for advanced in vivo imaging. Future studies will delve into detailed characterisations regarding the biological response to the nanohybrids, their stability under biological conditions, and in vivo imaging.

3.5 HomoFRET Hypothesis

Calculation of the Förster radius was performed for NPs loaded with 50 wt% of AuNCs. In a first step the PL emission spectrum was extrapolated for wavelengths below 873 nm through linear regression (Figure 3.13). The overlap integral was then determined using:

$$J(\lambda) = \int_0^\infty F_D\,(\lambda)\,.\,\lambda^4\,d\lambda \qquad (19)$$

$F_D(\lambda)$ is the PL emission intensity at λ, with the intensity normalised to unity over the whole wavelength range. $\varepsilon_A(\lambda)$ is the absorbance at λ in units of $M^{-1}cm^{-1}$, and λ is in units of nm.

In this case, the overlap integral yields 4.9 ´x 10^{13} $M^{-1}cm^{-1}$ nm^4.

The Förster radius is then obtained in units of Å (Å^6) using: $R_0^6 = 8.79 \,.\, 10^{-5}\,(\kappa^2\,.\,n^{-4}\,.\,QY\,.\,J(\lambda))$
With $k^2 = 2/3$ for dynamically random orientation, n = 1.5 for PEMA, and QY = 0.37% for NPs loaded with 50 wt% of AuNCs, one obtains: $R_0 = 1.2\ nm$

Uncertainty on this value comes from different sources:

(1) Below 873 nm the PL emission spectrum was extrapolated linearly. A slower decay to 0 would lead to an increase in the overlap integral and so of R_0. However, the importance of this error is considered to be less than 10%.

(2) Moreover, the sensitivity of the detector depending on the wavelength can influence the shape of the measured PL emission spectrum. Measurements with other types of spectrometers indicated that the used spectrometer rather underestimates the PL intensity in the lower wavelength region. The error would therefore lead to an underestimation of R_0 and could reach approximately 50%.

(3) The considered refractive index and its wavelength dependence could further influence the obtained value: Here we have taken n = 1.5, which is a rather high estimate (A. R. Katritzky, S.

Sild, M. Karelson, J. Chem. Inf. Comput. Sci. **1998**, 38, 1171). The presence of water and the long wavelengths could further contribute to reduced n values that would increase R_0. The potential error could reach 10% on R_0.

Taken together, we obtain an uncertainty of the order of 1 nm, with R_0 = 1.2 nm being a low estimate.

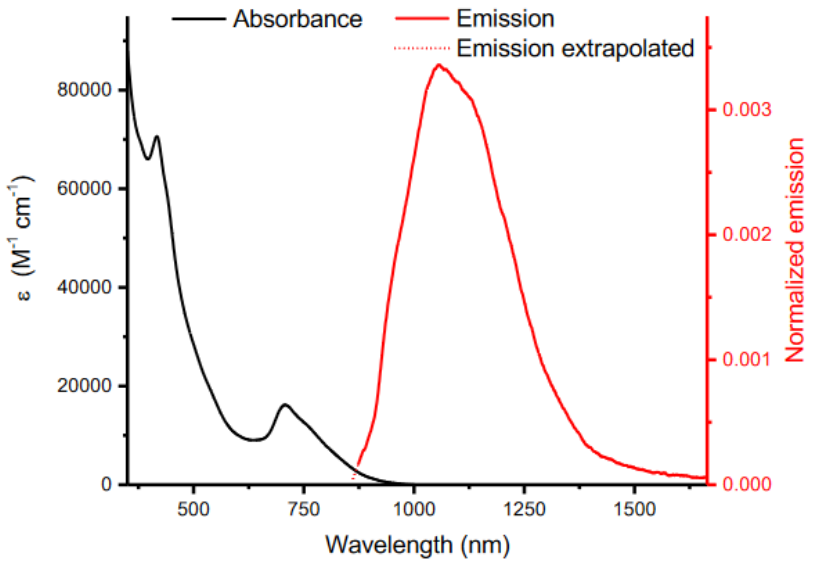

Figure 3.13 Absorbance and PL emission spectra (λ_{ex} = 730 nm) of NPs loaded with 50 wt% of AuNCs used to determine the homo-FRET radius. Below 873 nm the PL spectrum was extrapolated linearly.

Chapter Four

4.1 Tb Complexes as Versatile Energy Donor for Nanoparticle-Based Molecular Diagnostics

High sensitivity and speed are two crucial factors needed for point-of-care testing (POCT). The sensitivity of a probe towards detecting a particular disease is shown in the limit of its detection of minute concentrations of the biomarkers of that disease. Rapidly sensing such low concentrations of biomarkers can help in the early treatment of diseases before the symptoms appear or before they progress into a more aggressive stage particularly in the case of cancers.[286–288] PL based techniques are the most commonly used in biosensing and bioimaging due to their unparalleled level of sensitivity and speed that can be used to reach unprecedented spatial and temporal resolutions for monitoring biological systems.[289,290] Due to their throughput, low cost and versatility, PL-based techniques make POCT and personalized medicine more readily available.[269]

The application of NPs, such as AuNPs, QDs, and lanthanide-doped NPs has significantly improved the sensitivity, the multiplexing capacity and the reproducibly of the biosensors that use them as labelling probes.[291] Lanthanide (Ln) compounds are very effective and versatile luminescence biosensing and bioimaging probes that cover the entire spectra from the UV (Gd^{3+}) through the Vis (Eu^{3+} and Tb^{3+}) to the NIR (Nd^{3+} and Yb^{3+}) regions. Long luminescence lifetimes and narrow emission bands, typical characteristics of Ln elements, make them attractive for TG bioimaging and biosensing. Tb, in particular, have well-separated and narrow emission bands across the visible region (~490 – 670 nm). These unique features, which exist due to the parity (Laporte) and spin-multiplicity forbidden f-f optical transitions, make them attractive for multiplexed TG-FRET biosensing and bioimaging, which we have applied well in our group. [21,35,201,292–296]

FRET helps to eliminate the need for different excitation wavelengths when observing different emission detection channels for PL biosensing. As explained in the second chapter of this thesis, it is only necessary to excite the FRET donor and the energy will be transferred to the acceptor thus making it possible to observe the donor quenching and acceptor sensitisation signal simultaneously. Applying Ln compounds such as Tb to FRET biosensing further improves the detection sensitivity as time-gating helps suppress background fluorescence. Multiple narrow emission bands of Tb make multiplexing possible to detect different acceptor probes with only one donor probe. The combination of Ln complex with NPs for TG-FRET immune-sensing has been demonstrated to produce sub-nanomolar detection limits of several cancer biomarkers, i.e., carcinoembryonic antigen (CEA), prostate-specific antigen (PSA), and neuron-specific enolase (NSE).[17] AuNPs have been applied as a quencher for different biosensing assays. Our group has shown that the mechanism with which AuNPs quench the donor emission is by NSET and not FRET, as is often assumed. The energy transfer efficiency falls with the fourth power of the distance between the donor and acceptor in NSET as opposed to the sixth power as it is in the case of FRET, which enables energy transfer at a greater donor-acceptor distance of up to 40 nm.[223] Nanobodies have been reported to increase sensitivity in FRET biosensing of cancer biomarkers such as EGFR due to their smaller sizes, which significantly reduces the donor-acceptor distances.[297]

Despite the numerous advantages of applying Tb complexes as donors in multiplexed TG-FRET biosensing and imaging, few affordable and suitable commercial Tb complexes are available for such applications. The high cost of optically desirable Tb complexes is because they are challenging to synthesize. In this chapter, I carried out a photophysical characterization of and biosensing with a new family of macrocyclic Tb complex, Corafluor Tb (CRF-Tb). The family consists of CRF-1 (H) ligands and the halogenated derivatives CRF-2 (Cl) and CRF-3

(Br) (Figure 4.0). The macrocyclic cage shields the Tb^{3+} from quenching by surrounding water molecules, increasing its PL lifetime. The ligand also serves as a scaffold for labelling biomolecules. The presence of pentafluorophenyl ester (pfp) creates an avenue for forming amide bonds with the primary amines on proteins or other molecules of interest. The halogens on the derivative ligands CRF-2 and CRF-3 help shift their absorption spectra of the more visible region, which is more tolerable for bioimaging.[22] By enhancing spin orbit coupling, the presence of heavy atoms such as bromine can also favour the formation of triplet state and therefore lanthanide sensitization.[298,299]

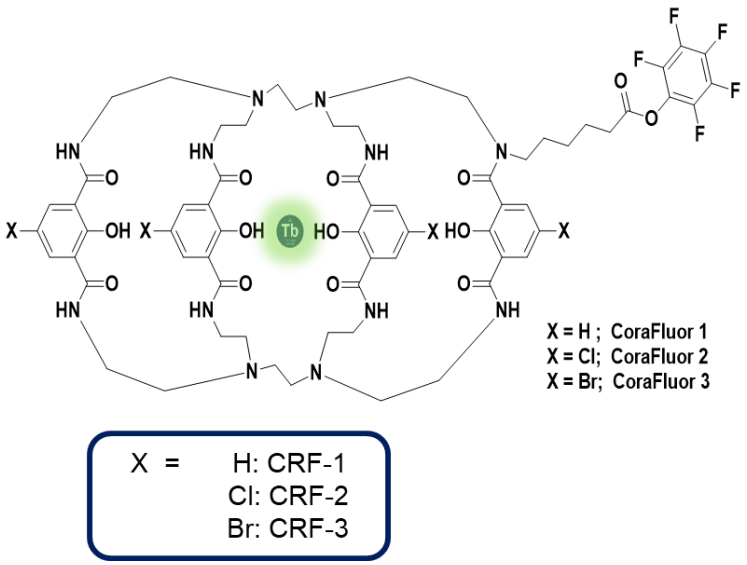

Figure 4.0 Structure of Corafluor Tb ligands (1, 2, 3) with pfp

The objective of this chapter is to study the photophysical properties of a new family of Tb complex and apply the complex as a donor in resonance energy transfer biosensing with nanoparticles (AuNP and QD) and also for sensing of an important cancer biomarker (EGFR).

First, I carried out the photophysical analyses of the CRF; then, I employed biotin-streptavidin interaction to bring AuNP and QD closer to the Tb complex to facilitate for FRET biosensing. Finally, I applied the concept in EGFR biosensing using EgA1 and EgB4 nanobodies.

4.2 Materials and Methods

4.2.1 Materials:

AuNP-Biot (diameter 30 nm), QD 655-Biot and sAv-QD 655 were purchased from Thermo Fischer Scientific. Corafluor supplied the pentafluorophenyl (pfp) activated Tb complexes (CRF-1, CRF-2 and CRF-3). Lumiphore provided N-Hydroxylsuccinimide (NHS) activated Lumi4-Tb complex in lyophilized form. Nanobodies against EGFR (EgA1 and EgB4) were produced as described elsewhere[300] at the Department of Biology Utrecht University, Netherlands. Recombinant human EGFR Fc chimera (#344-ER-050) dimers (MW: ~190 kDa for EGFR dimer and ~195 kDa for HER2 dimer) were purchased from R&D system. Bovine serum albumin (BSA), streptavidin (sAv), tris(hydroxymethyl)-aminomethane (TRIS/Cl), sodium tetraborate (borate), phosphate buffer saline (PBS), sodium carbonate, sodium bicarbonate, and were purchased from Sigma-Aldrich. High-quality Milli-Q water with a resistivity of 18.2 MΩ.cm was used for preparing solutions.

4.2.2 Conjugation of Tb-sAv

Streptavidin was dissolved in water at 1 mg/mL concentration. Pfp-activated CRF-1 dissolved to 2.5 mM in dimethylacetamide (DMAc), and 8 mM of Lumi4-Tb-NHS (L4Tb) in dimethylformamide (DMF) were separately mixed with streptavidin (reaction ratio 5) in 100 mM carbonate buffer (pH 9.0). CRF-1 and L4Tb concentrations were measured at 340 nm using molar absorptivity of 20,000 M^{-1} cm^{-1} and 26000 M^{-1} cm^{-1} respectively as provided by the suppliers. The concentration of streptavidin was measured at 280 nm taking the molar absorptivity of 168,000 M^{-1} cm^{-1}. Incubation was carried out at room temperature while rotating on an ELMI Intelli-Mixer at 30 rpm for 2 hours. The Tb-sAv conjugates were then purified by washing four times with 100 mM Tris-Cl (pH 7.4) using a 7 kDa molecular weight cut-off (MWCO) desalting spin column by spinning at 1500 rpm for 2 minutes to remove unconjugated

Tb complexes. The purified conjugates were stored at 4 °C. The absorbance, emission and luminescence lifetime of conjugated Tb complexes were measured. The conjugation ratios were determined by a linear combination of the respective absorbance values of Tb complexes and streptavidin.

4.2.3 Photostability and Stability of Tb complexes in different buffers

The stability of the Tb complexes in buffer were measured on a Tecan fluorescence plate reader. The measurement was carried out in different buffers; Carbonate buffer (pH 9.0), PBS, TRIS-Cl and HEPES at pH 7.4. Tb complexes were prepared at 100nM, 50nM, 10nM and 2nM concentrations. The Tb complexes were excited at 337 ± 10 nm and the emission intensities were recorded at 550 ± 3.8 nm.

The stability of the Tb complexes and CRF-1-sAv in PBS, TRIS-Cl, HEPES at physiological pH and Carbonate buffers at pH 9.0 was studied over 20 days. Concentrations of 100, 50, 10 and 2 nM of the Tb complexes were prepared in triplicates in three 96 well plates to have 3 storage conditions. The first plate was stored at 4°C in the refrigerator, the second plate was stored in the dark at room temperature while the third plate was stored at room temperature under ambient light. The plates were covered with a thin transparent film cover and stored after each measurement. The intensities were measured daily on Tecan plate reader.

Photostability of Tb complexes were measured in 50 mM TRIS-Cl (pH 7.4) on Fluorolog-3 (Horiba Instruments). 50 uL of 100 nM each Tb complex was put in 50 µL volume cuvette. This way, the entire volume was exposed to the light source at the same time. The Tb complexes were excited at 350 ± 5 nm and the photo luminesce intensity was observed at 550 ± 1 nm for 180 seconds.

4.2.4 CRF-1 Nano-Surface Resonance Energy Transfer to AuNP

CRF-1-sAv (conjugation ratio of 4 Tb to 1 sAv) was diluted to a 2.5 nM sAv (10 nM Tb) concentration in Milli-Q water. Biot-AuNP was dissolved in 2nM TRIS-Cl (pH 8.5) to 29.6 pM. The concentration of CRF-1-sAv was kept constant at 0.8 nM sAv (3 nM Tb) per well while the concentration of biot-AuNP was gradually increased from 0 to 16 pM per well. The mixtures were prepared in 0.5 mL tubes in triplicates and incubated at 37°C for 2 hours after which it was distributed into different wells of a black 96 well plate (KRYPTOR Plate).

The photoluminescence decay of the Tb-AuNP was measured with EI Fluorescence plate reader using multichannel scaler (MCS) of 4000 detection bins and 2 µs integration time. The intensity of the decay curves was integrated from 0.1 to 2 ms. The photoluminescence decay was observed at 490 ± 10 nm after exciting with a 337 nm nitrogen laser (NL 100, SRS) at 20Hz. The intensities of the Tb-AuNP between 0.1 to 2 ms were also recorded on Tecan fluorescence plate reader. The Tb complexes were excited at 337 ± 10 nm and the emission intensities were recorded at 490 ± 10 nm with a delay of 0.1 ms and integration time of 2 ms. Tb-AuNP intensities were also measured on KRYPTOR Compact Plus (Cezanne/ThermoFisher) clinical fluorescence plate reader using a 337 nm nitrogen laser (NL 100, SRS) at 20Hz. The emission decay was observed at 490 ± 10 nm.

4.2.5 Förster Resonance Energy Transfer from CRF-1 to QD-655

CRF-1-sAv was diluted to 14 nM in 10 mM TRIS-Cl (pH 7.4) and biot-QD655 was diluted to 1.1 nM in the same buffer. The Tb-QD system was prepared in the same buffer with 1% BSA. CRF-1-sAv was kept constant in all wells at 1 nM sAv (4 nM Tb) and the concentration of biot-QD655 was gradually increased to 0.5 nM. The mixtures were prepared in 0.5 mL tubes in triplicates and incubated at 37°C for 2 hours after which it was distributed into different wells of a black 96 well plate (KRYPTOR Plate)

The photoluminescence decay was measured on 3 commercial plate readers as described above with the QD emission recorded at 660 ± 6.5 nm on the EI Fluorescence plate reader. On the KRYPTOR, the QD was observed at 640 ± 6.5 nm and on the Tecan plate reader at 660 ± 10 nm.

4.2.6 EGFR Immunoassay

4.2.6.1 CoraFluor to Nanobody Conjugation

CRF-1 dissolved in 2.5 mM of DMAc was mixed (the reaction ratio of LTC/VHH = 6) with the nanobodies (EgA1-no tag, EgA1-His6) in 100 mM carbonate buffer (pH 9.0). The mixture was incubated for 2 hours at 25 rpm at room temperature. For CRF-1-NB-conjugate purification, the samples were washed four to six times with 100 mM TRIS-Cl (pH 7.4) using 3 kDa MWCO Amicon spin column at 4000 g. CRF-1 concentration was determined as described above. Nanobodies were quantified by absorbance measurements at 280 nm using an extinction coefficient of 34,505 M^{-1} cm^{-1} (EgA1-no tag). The conjugation ratios were determined by a linear combination of the respective absorbance values of CRF-1 and nanobodies within the CRF-1-nanobody conjugate absorbance.

4.2.6.2 QD to Nanobody Conjugation

EgB4-His6-biotin to the QD655-sAv conjugation was performed in a molar ratio of 20:1 (EgB4-biotin per QD). Thus, 2µL of 150 µM of EgB4-His6-biotin was added to 7.5 µL of 2µM of sAv-QD655 in 100mM Tris-Cl (pH 7.4) and mixed for 30 minutes. The conjugates were freshly prepared before FRET immunoassays. Unbound EgB4 were separated by 100 kDa MWCO spin column by washing four times with 100 mM sodium tetraborate buffer (pH 8.4). Purified conjugates were centrifuged at 4000 g and supernatants were stored at 4°C. QD concentrations were determined by absorbance measurements using a molar extinction coefficient of 8.3 x 10^6 M^{-1} cm^{-1} (at 405 nm) for QD655-sAv as provided by the manufacturer.

EgB4 was quantified by absorbance measurement at 280 nm using an extinction coefficient of 38,055 M^{-1} cm^{-1}.

4.2.6.3 EGFR Biosensing

CRF-1-EgA1 and QD-EgB4 were each dissolved in 50 µL 10 mM TRIS/Cl buffer (pH 7.4) containing 0.05% bovine serum albumin (BSA, Sigma-Aldrich). Homogeneous FRET immunoassay calibration curves against EGFR, where the overall measuring volume of 150 µL contained 100 µL of constant assay solution (50 µL of CRF-1-EgA1 with 6 nM EgA1 and 50 µL of EgB4-QD conjugated with 3 nM QD655-sAv). Optical bandpass filters (Delta and Semrock) for CRF donor and QD acceptor channel were 494±20 nm for LTC and 640±14 nm, respectively. All FRET assays were measured in black 96-well microtiter plates with an optimal working volume of 150 µL. Each sample containing EGFR antigen sample was prepared three times, and the samples without EGFR were prepared 10 times. All samples were measured in triplicates. After sample preparation the microtiter plates were incubated for 180 minutes at 37°C before measurements on Tecan KRYPTOR compact plus (Thermo Fisher) and EI fluorescence plate readers.

4.3 Results and Discussions

4.3.1 Photophysical Characterization (Absorption, Emission, Lifetimes and Quantum Yield)

The absorption peak for CRF-1 is around 340 nm whereas the peak is shifted to around 360 nm for the halogenated derivatives CRF-2 and CRF-3, which hold promises of more tolerable excitation wavelength for live cell analyses (Figure 4.1).

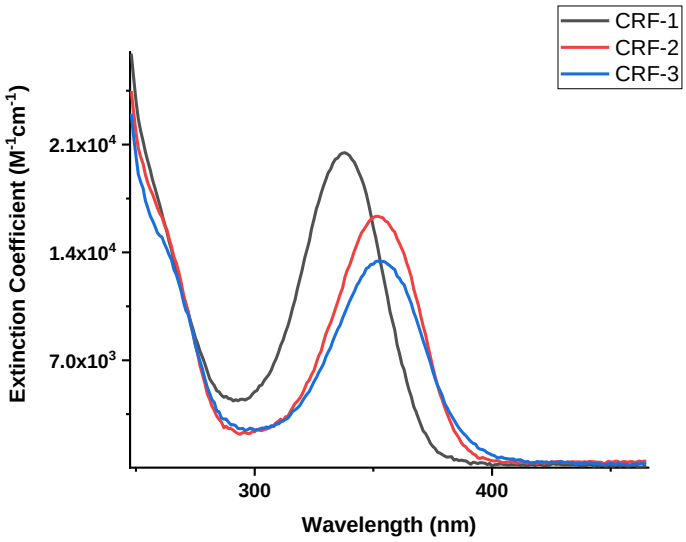

Figure 4.1 Absorption spectra of CRF Tb complexes CRF-1 (Black); CRF-2 (Red) and CRF-3 (Blue) in water.

The emission spectra for the three Tb complexes in this study were similar and gave the characteristic narrow and well separated emission bands across 490 nm to 680 nm. The emission bands arise from the $^5D_4 \rightarrow {}^7F_J$ transitions around 490 (J = 6), 545 (J = 5), 580-590 (J=4), 618 (J = 3), 650 (J = 2), 669 (J = 1), and 678-681 nm (J = 0), respectively of the lanthanide centre.[22,245] The Corafluor Tb complexes have milliseconds lifetimes which is suited for time-gating. The PL decay curves were fitted with a mono-exponential decay equation. CRF-1 has the longest lifetime (2.8 ± 0.3 ms) while CRF-2 (2.0 ± 0.2 ms) & CRF-3 (1.5 ± 0.3 ms) have shorter lifetimes that are still suitable for TG measurements. The halogens on the ligand is responsible for both the bathochromic shift and the reduced PL lifetimes of the Tb complexes (Figure 4.2).

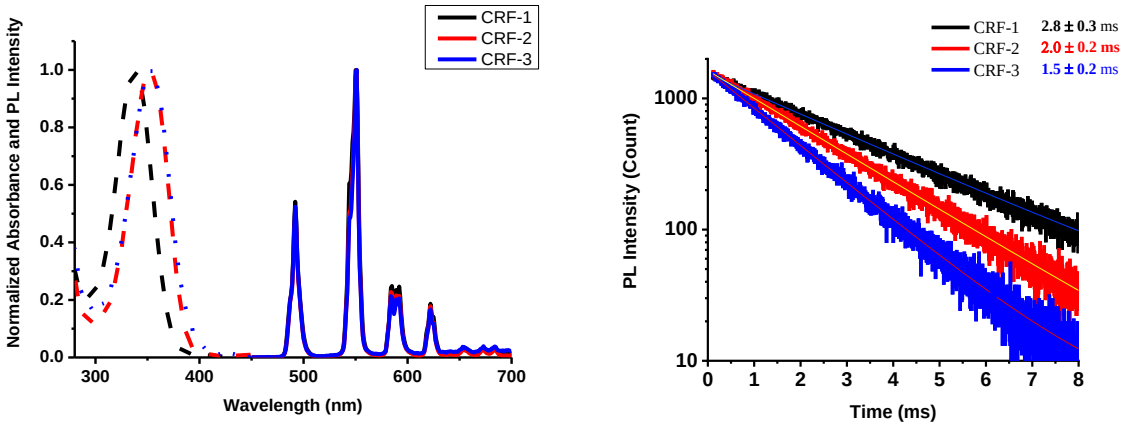

Figure 4.2 Absorption and emission spectra of CRF Tb complexes (Left); PL decay curve of CRF complexes (Right) CRF-1 (Black); CRF-2 (Red) and CRF-3 (Blue)

Hydroxyl bond (O-H) vibrations and high temperature which increases vibrations of the environment are the major contributors to Tb PL quenching. Hence, the O-H vibrations and thermal vibrations are minimised by measuring the PL lifetimes in D_2O and at low temperatures to obtain the unquenched PL lifetimes. It is therefore possible to estimate the QY_{Tb} from the ratio of quenched and unquenched lifetimes of the Tb. The quantum yield (QY) was estimated based on the assumption that the quenching of Tb radiative lifetime (τ_{rad}) was efficiently prevented at 4°C in D_2O. Hence the lifetime at 4°C in D_2O was taken to represent the unquenched lifetime of Tb.

The overall QY of a Tb complex (QY_{ovr}) is a product of the antenna to Tb efficiency and the Tb ion QY (QY_{Tb}). This QY_{Tb} is the ratio of photons that the Tb ion absorbs to the photons that

the Tb ion emits. The QY_{ovr} is considered for Resonance Energy Transfer from Tb to Nanoparticle acceptors.[301]

Figure 4.3 presents the PL decay curves of the complexes in water and in D_2O at different temperatures help to obtain the relative QY of Tb in the complexes. The unquenched lifetime is taken as the standard for calculating the relative QY of Tb in H_2O at room temperature.

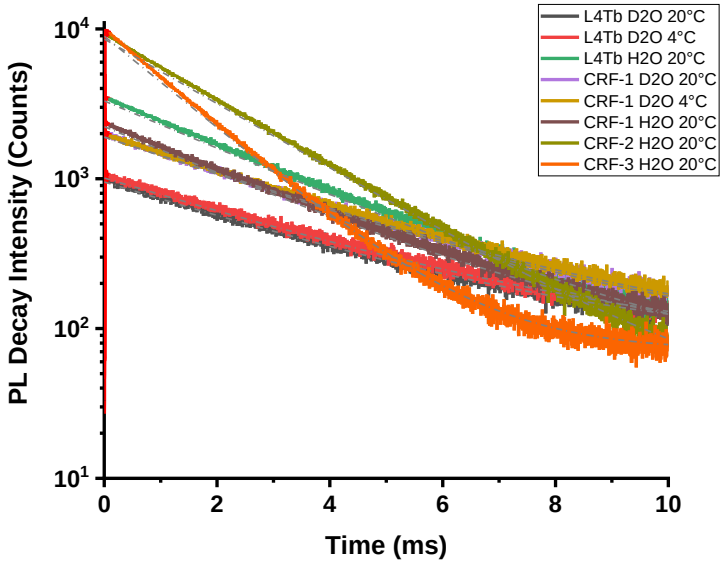

Figure 4.3 PL decay curve of Tb complexes in water and D_2O at different temperature.

The decay curves are mono-exponential fit

$$I(t) = X_1 e^{\frac{-t}{\tau_1}} + C \qquad (20)$$

where X_1 is the lifetime amplitude;
C is the background intensity, and
I(t) is the time-dependent PL intensity.

The least quenched PL, D_2O at 4°C was the reference for measurement and was assumed to provide a QY of 100%. The equation below was used derive the relative QY_{Tb}

$$QY = \left(1 - \left(\frac{\tau_A - \tau_B}{\tau_A}\right)\right) * 100 \qquad (21)$$

Where τ_A is reference unquenched PL lifetime,
τ_B is PL lifetime measured

Table 3 Tb Lifetimes and QYs

	Luminescence lifetime (ms)			
		D_2O	H_2O	% QY
	20°C	4°C	20°C	
L4Tb	3.5	**3.6**	2.7	**76.2**
CRF-1	3.3	**3.4**	2.7	**80.0**
CRF-2	X	X	2.0	**57.6**
CRF-3	X	X	1.4	**39.6**

The QY_{Tb} of L4Tb and CRF-1 are 76 % and 80 % in water respectively. The QY_{Tb} of CRF-2 and CRF-3 are 57 %and 40 % and are lower but can still be sufficient for imaging and biosensing applications. The quenched lifetimes and lower QYs observed for CRF-2 and CRF-3 are attributed to poor antennae sensitization of the halogenated ligand and back energy transfer from the Tb ion excited state to the triplet state of the ligand. The PL lifetimes of CRF-2 and 3 are around 1.4 - 2 ms which is still very sufficient for time-gating applications. CRF-1 and L4Tb have similar range of lifetime and QY in solution. This is not surprising as their chemical structures are very similar.

4.3.2 Streptavidin Conjugation to CRF-1

Conjugation of streptavidin (sAv) or any other protein to CRF-1 is possible due to the abundance of primary amine groups that can react with pentafluorophenyl ester function on CRF complexes to form an amide bond (Figure 4.4A).

The appearance of the double absorption band in the absorbance spectra was the first evidence of a successful conjugation. The absorption band of CRF-1 alone (340 nm) and sAv alone (280 nm) were clearly evident in the absorbance spectra of the Tb-sAv conjugate, hence, the degree of labelling of Tb to sAv was determined by the molar concentration ratio of 2.0 Tb per sAv (Figure 4.4B). While the emission spectra of the Tb complexes remained the same, the PL intensity of the Tb in Tb-sAv conjugates was quenched by about 30% and the lifetime by 10% (from 2.8 ms in CRF-1 to 2.6 ms in CRF-1-sAv) (Figure 4.4C). This quenching is also attributed to back energy transfer from the Tb excited state to the triplet state of the ligand. This implies that the quenching which results due to conjugation still gave the avenue to carry out TG measurements with the conjugated Tb complexes.

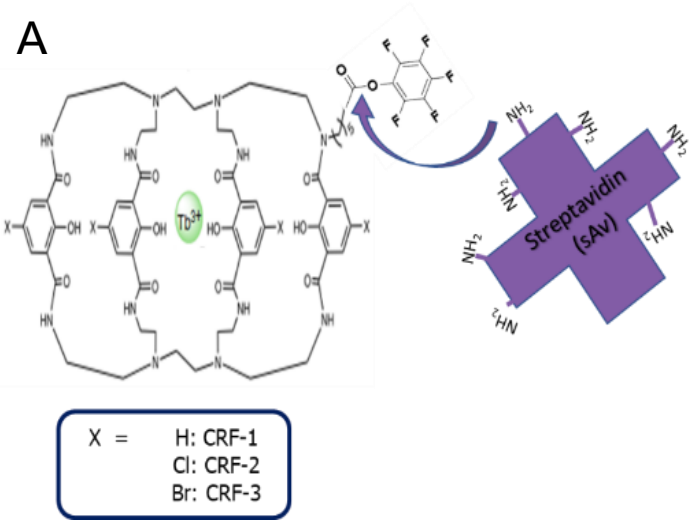

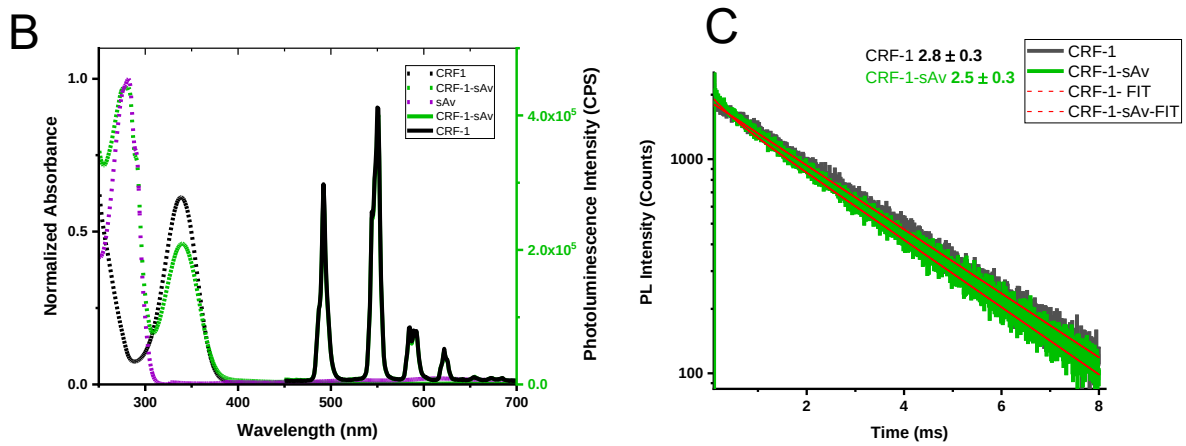

Figure 4.4 (A) sAv conjugation reaction scheme. (B) Absorption and Emission of CRF-1 and CRF-1-sAv; (B) PL decay of CRF-1 and CRF-1-sAv. CRF-1 (Black); sAv (Purple) and CRF-1-sAv (Green)

4.3.3 Stability in different buffers

The stability of these complexes was studied in different conditions, for L4Tb the conjugates with sAv were also tested. The complexes retained 80% of their PL intensities over a period of 20 days at 4 °C in 0.5M TRIS-Cl pH 7.4, which is often used for FRET biosensing with Tb conjugated proteins and QDs (Figure 4.5). The observed quenching can be attributed to gravitational pull of the complexes over these periods as the plates were not agitated to resuspend the complexes. This precipitation was confirmed by an even higher PL loss of CRF-1-sAv, which is significantly heavier due to the sAv protein. The same pattern was followed by the L4Tb complexes.

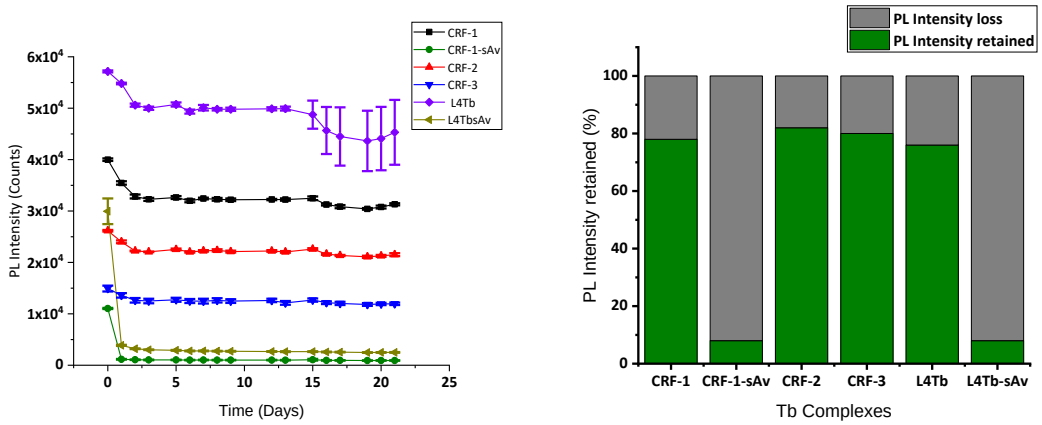

Figure 4.5 PL intensity of 100 nM of CRF complexes in 0.5M Tris-Cl buffer in microplate over 20 days. Excitation 350 ± 5 nm Emission 550 ± 1 nm (left). Bar chart illustration of total intensity loss during the period (right); CRF-1 (black), CRF-1-sAv (green), CRF-2 (red), CRF-3 (blue), L4Tb (purple), L4Tb-sAv (dark yellow)

The complexes showed similar stability patterns at room temperature whether in the dark or under ambient light at different concentrations (Figure 4.6).

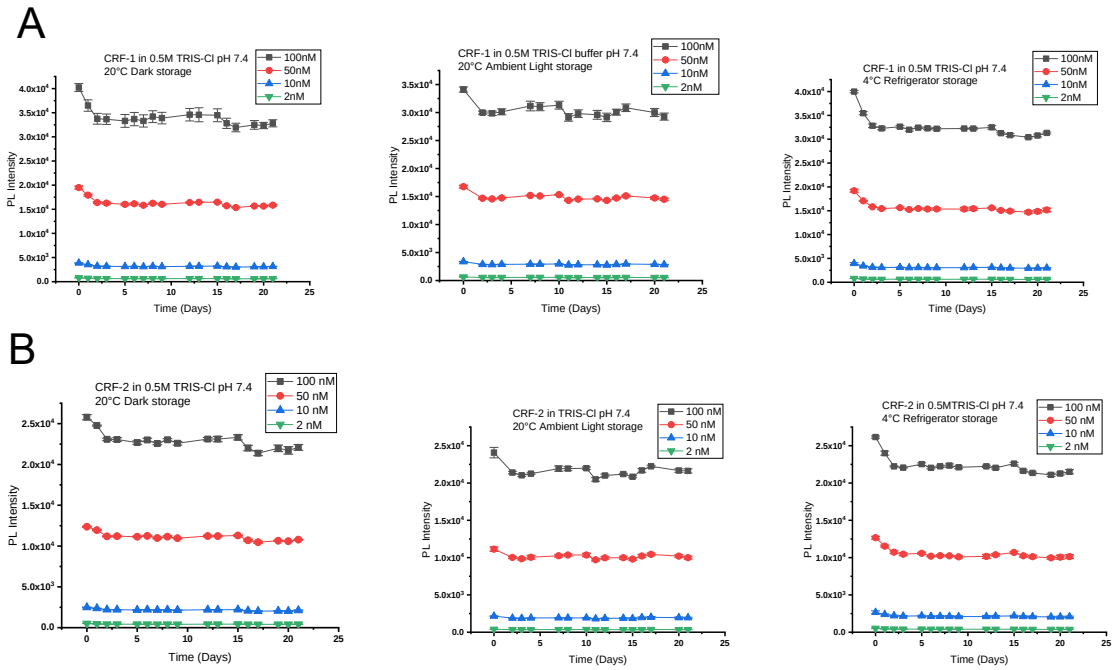

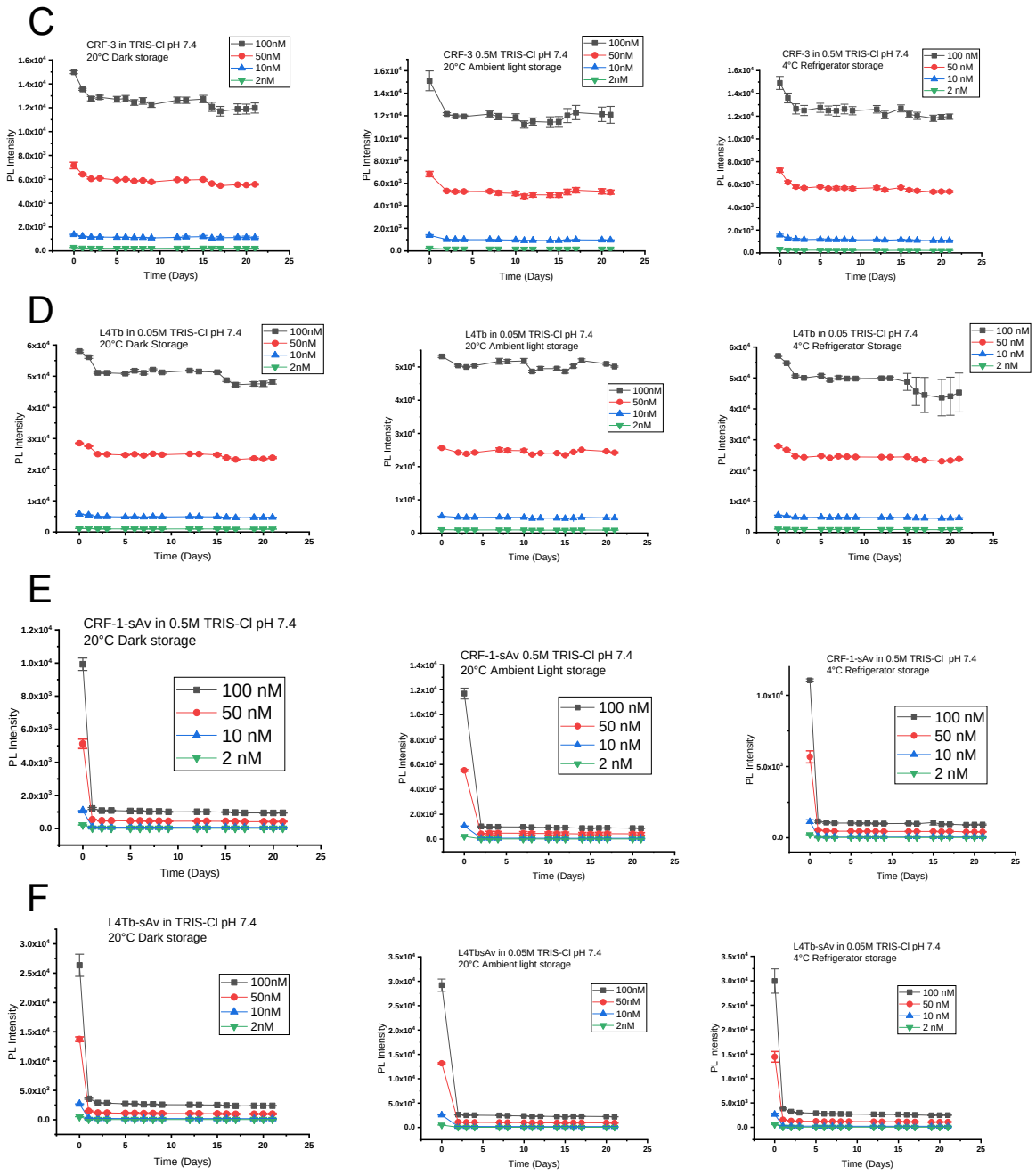

Figure 4.6 PL intensity of CRF complexes in 0.5M Tris-Cl buffer in microplate over 20 days; CRF-1 (Row A) CRF-2 (Row B) CRF-3 (Row C) L4Tb (Row D) CRF-1-sAv (Row E) L4Tb-sAv (Row F) ; Left Column (Dark storage at 20 °C);Middle Column (Storage Ambient Light at 20 °C); Right Column (Storage at 4 °C) Excitation 350 ± 5 nm Emission 550 ± 1 nm (left). Bar chart illustration of total intensity loss during the period (right); CRF-1 (black), CRF-1-sAv (green), CRF-2 (red), CRF-3 (blue), L4Tb (purple), L4Tb-sAv (dark yellow)

The CRF-1 complexes were also stable in PBS and HEPES buffers commonly used for protein and nucleotide storage, respectively. The complexes however were not stable in Carbonate buffer at pH 9.0 and so it is expedient to store the complexes in physiological pH over long period of time (Figure 4.7).

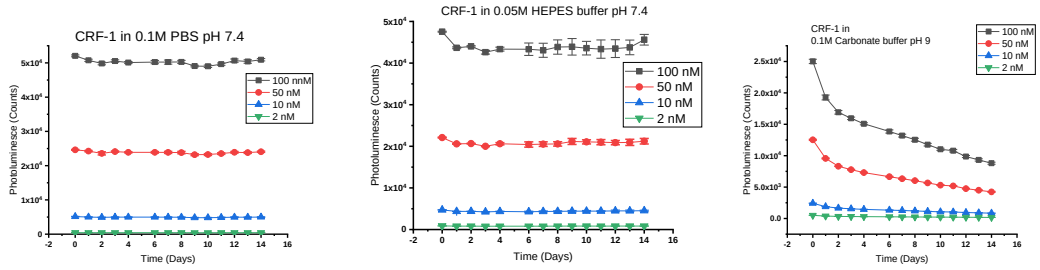

Figure 4.7 Stability of CRF-1 in 0.05M PBS (left) and HEPES (centre) buffer pH 7.4 and 0.1M Carbonate buffer at pH 9.0 under different conditions for 20 days. 100 nM (black); 50 nM (red); 10 nM (blue); 2 nM (green)

The conjugated and unconjugated CRF-1 and L4Tb retained up to 80 % of their intensities after 30 minutes of exposure to high intensities of Xenon Continuous wave lamp on the Fluorolog-3 (Figure 4.8). In spite of these harsh conditions, the complexes still possess sufficient PL intensities for measurements.

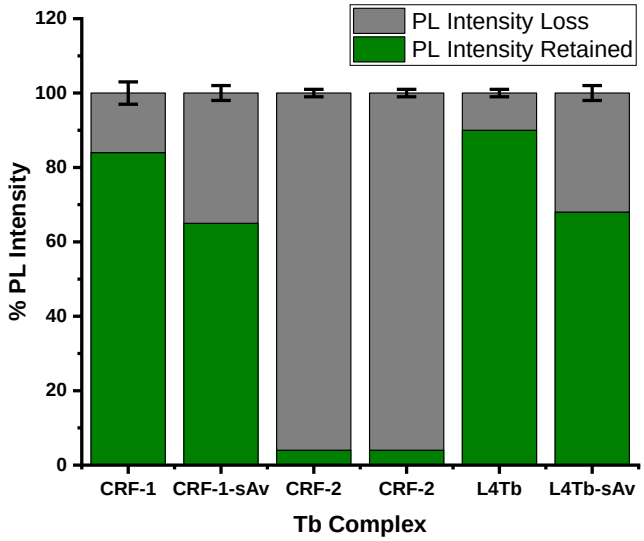

Figure 4.8 Bar chart illustration of total intensity loss during the period

4.3.4 CRF-1 Nanosurface Energy Transfer to AuNP

NSET from CRF-1-sAv to biot-AuNP was made possible first, by the overlap of biot-AuNP absorption and the emission of CRF-1 spectra and secondly by the vicinity of CRF-1 and Au-NP after biot-sAv conjugation of both NSET participants as shown in Figure 4.9.

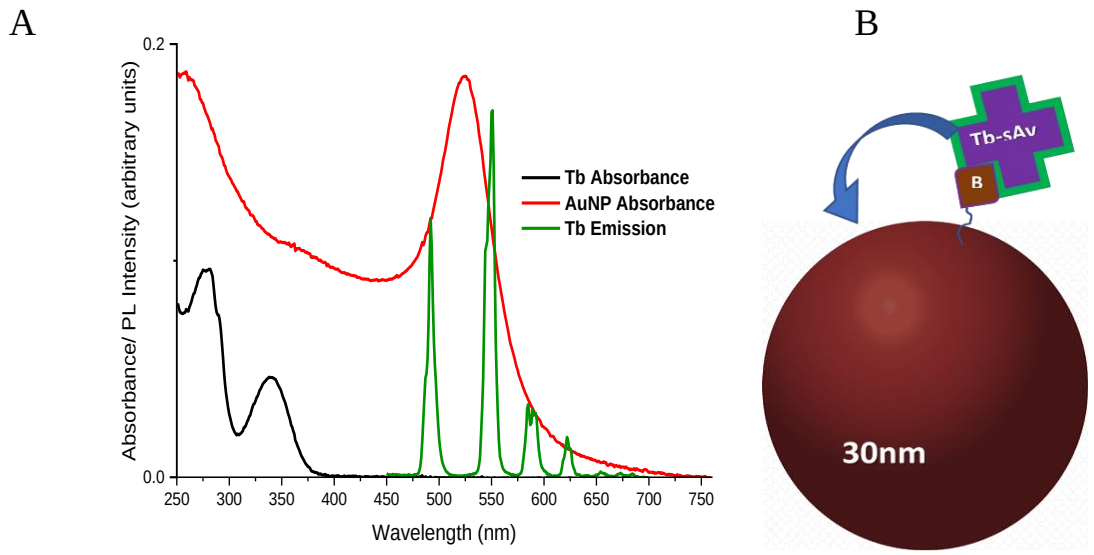

Figure 4.9 CRF-1-sAv absorption (black) and emission (green) overlap with biot-AuNP absorption (red) (left) (b) CRF-1-sAv-biot-AuNP interaction (right)

In Figure 4.10, it is observed that there was a decrease in the photoluminescence intensity with increasing concentration of biot-AuNP. This implies that there was continuous formation of CRF-1-sAv-biot-AuNP until the saturation point around 2 pM concentration of biot-AuNP. The photoluminescence decay curve on Figure 4.10A showed a gradual change in the shape of the decays from single to multiexponential with increasing concentration of biot-AuNP. This means that there is resonance energy transfer from CRF-1 to AuNP via biot-sAv interaction. This was proven by the control experiment where the intensity of unconjugated CRF-1 remained the same with increasing biot-AuNP concentration.

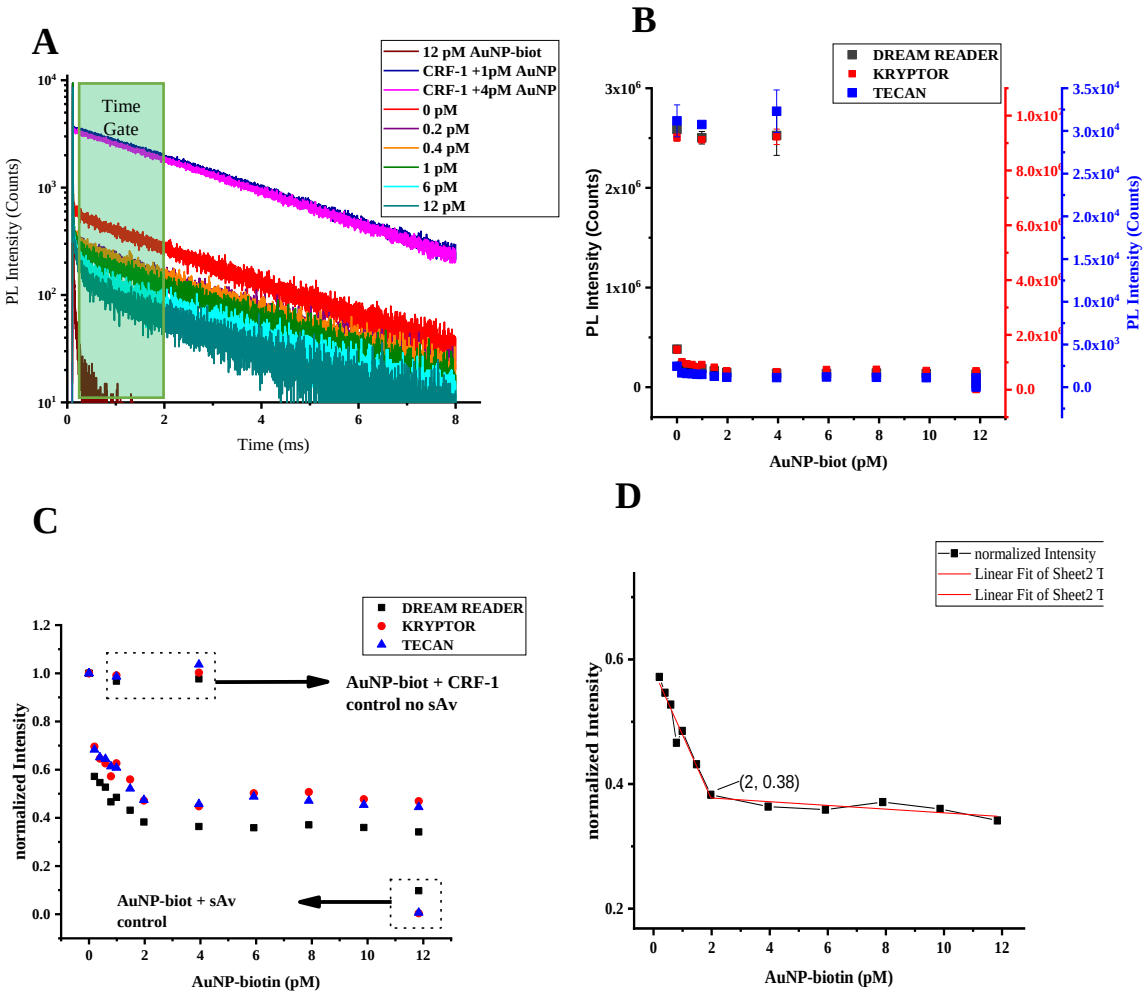

Figure 4.10 (A) PL decay curves of few AuNP concentrations quenching Tb PL on Edinburg plate reader; 12 pM AuNP control (brown); CRF-1 + 1 pM AuNP (blue); CRF-1 + 4 pM AuNP (magenta); CRF-1-sAv +0 pM AuNP (red); 0.2 pM (purple); 0.4 pM (Orange); 1 pM (green); 6 pM (light blue); 12 pM (cyan). (B) Integrated time-gated intensities and; (C) Normalized integrated time-gated intensities between 0.1 and 2 ms plotted against increasing AuNP-biot concentrations; Y axis scale of the different plate readers used; Dream reader (black); Kryptor (red); Tecan (blue) (D) Dream Reader data extracted from (C) to obtain the intersect point.

4.3.5 QD655 Biosensing via Streptavidin – Biotin Interaction Using CRF-1 as Donor

The spectral overlap between the donor (Tb) emission and acceptor (QD) absorbance once again, fulfils one of the major criteria for FRET to take place as described above (NSET). Biotin-sAv interaction is once again utilised to bring the donor and acceptor together for FRET to occur. However, in this case it is possible to observe the emission of the Tb-excited QDs (Figure 4.11). Hence, we can have a ratiometric measurement of the FRET.

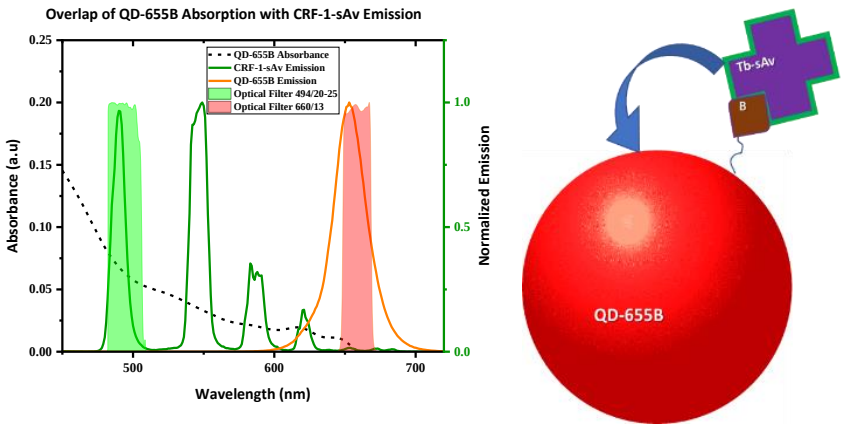

Figure 4.11 Spectral overlap and FRET scheme

The PL decays were studied with increasing concentration of QD from 0 to 0.5 nM at fixed concentration of 4 nM of Tb. The PL decay curves (Figure 4.12) of the experiment show the quenching of the Tb lifetimes in the donor channel and the sensitization of the acceptor lifetimes in the acceptor channel with increasing acceptor concentration and constant donor concentration.

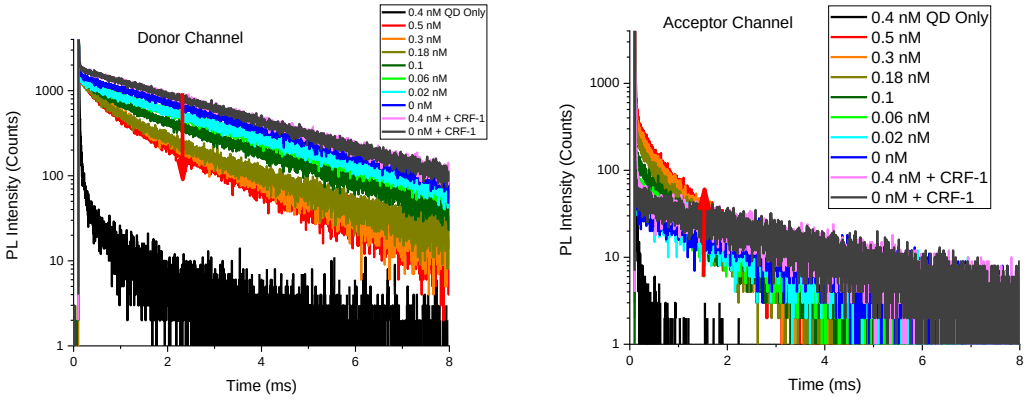

Figure 4.12 PL decay curve of CRF-1-QD FRET. Donor channel (left) Acceptor channel (right).

The sum of the intensities between 0.1 to 2 ms (Dream Reader and Tecan) 0.1 to 0.9 ms (KRYPTOR) was plotted. The Tb quenching and QD sensitization with increasing acceptor concentration is more pronounced in the TG-intensity graph of the donor and acceptor channels

of the three plate readers used (Figure 4.13). The control experiment points also prove that the sAv-biotin interaction was absolutely necessary for the energy transfer to occur.

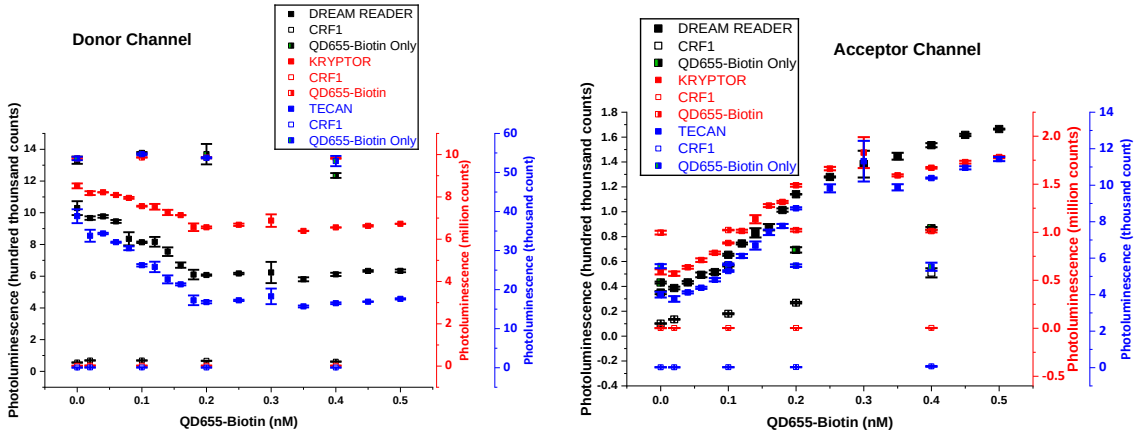

Figure 4.13 TG-PL Intensities. Donor channel (left) Acceptor (right) Edinburg plate reader (black) KRYPTOR Clinical plate reader(red) Tecan (blue)

The relative FRET ratio was obtained by relating the ratio of the acceptor to the donor intensities (FRET ratio) of the experimental points to the FRET ratio of the donor point alone without acceptor. An increase in the relative FRET ratio can be observed with increasing QD concentration until the saturation point is reached. The saturation point is around 0.23 nM of QD. This is the point where all the biot-QD surface is fully covered by Tb-sAv (Figure 4.14).

The linear part of the curve is taken used to calculate the detection limits of the instruments for the sensing. The limits of detections were in sub-nanomolar concentration ranges. The Edinburg Plate Reader (Dream Reader) had the lowest LOD at 1.2 pM. Tecan and Kryptor had 9.7 pM and 14.4 pM LODs respectively. Therefore, these instruments are adapted for sub-nanomolar FRET assays.

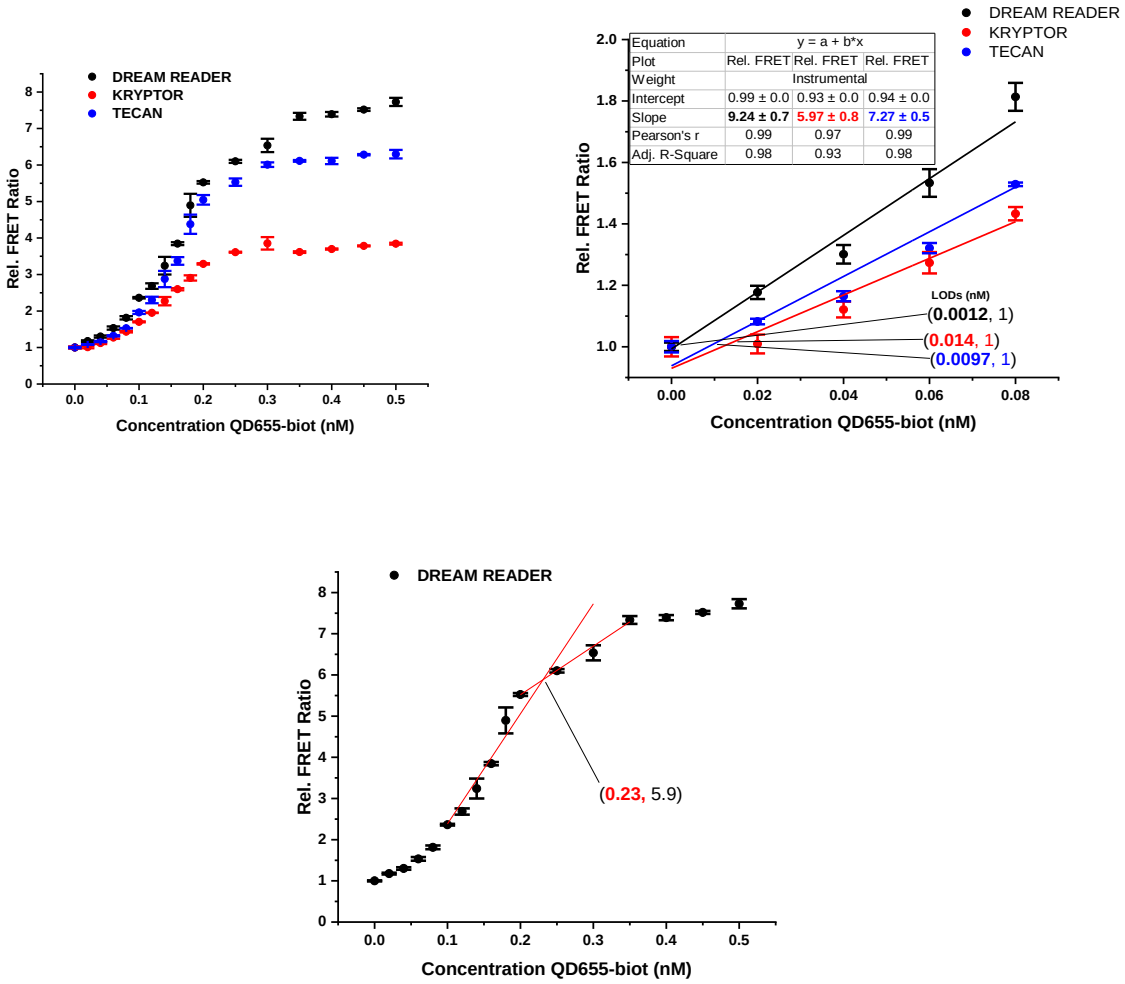

Figure 4.14 Relative FRET Ratio against QD concentration (left). FRET Calibration curve (right). Dream reader (black) KRYPTOR Clinical plate reader(red) Tecan (blue). Dream redear data showing intersect point (bottom)

4.3.6 EGFR Immunoassay Biosensing

EgA1 and EgB4 are nanobodies that bind to different specific domains of EGFR. The advantage of using nanobodies for immunoassays is that their small size reduces the distance (R) between the donor and acceptor and makes FRET to be more efficient and the assay more sensitive. CRF-1 labelled CRF-1 labelled EgA1 is expected to bind EGFR at one end while EgB4 conjugated to the surface of QD bind the same EGFR at the other end making a sandwich (Figure 4.15). This sandwich brings both the donor Tb and acceptor QD into reasonable distance for FRET to occur.

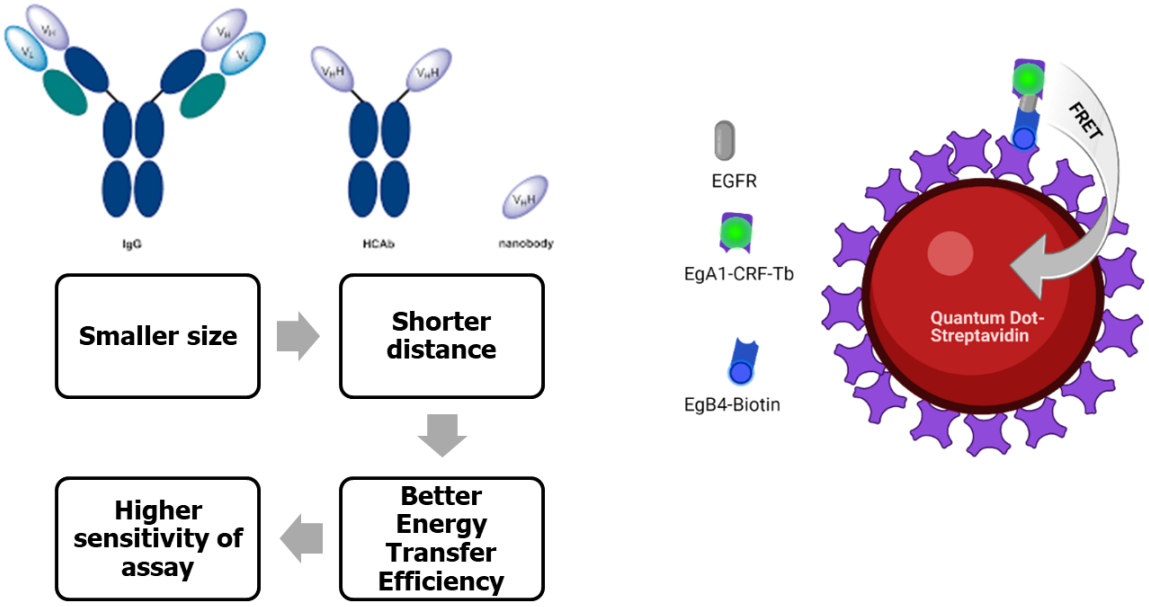

Figure 4.15 Scheme of nanobody for sandwich FRET biosensing

The TG PL intensity measurement did not show significant donor quenching or acceptor sensitization (Figure 4.16). This means that the donor and acceptor are not close enough to achieve the expected FRET. We suspect that this could be an issue with the conjugation of the acceptor and donor to the nanobodies or the formation of a corona on QD surface by BSA which hinders the interaction with EGFR. This experiment is currently being optimised.

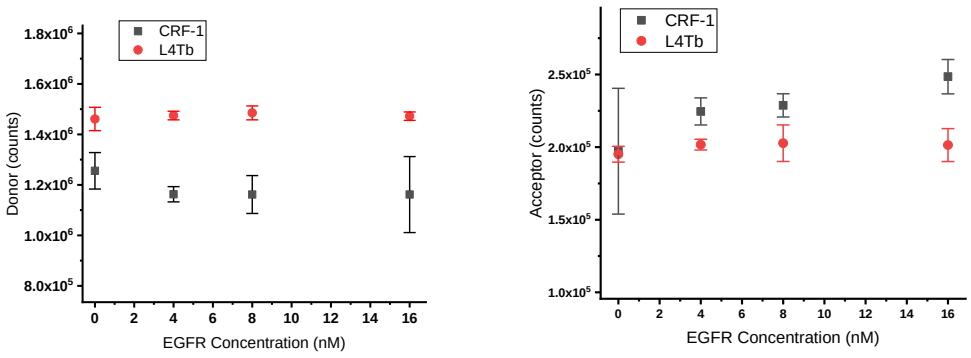

Figure 4.16 TG-PL intensities of donor (left) and acceptor (right)

4.4 Conclusions

Corafluor Tb complexes showed stable photophysical properties in different buffers and under various conditions like the well-studied L4Tb. The bioconjugation CRF-1 to sAv did not significantly reduce its photophysical properties. Thus, it was possible to conjugate CRF-1 to proteins and apply it for the different assays reported in this study. Effective quenching of CRF-1-sAv luminesce by biot-AuNP confirmed the success of the sAv labelling with complex. Sub-nanomolar concentration of QD was detected while applying CRF-1 as donor in biot-QD sensing which agrees with previous studies reported by the group whilst using other commercial luminescent Tb complex.

CRF-1 was applied in sandwich immunoassays to detect sub-nanomolar concentrations of EGFR on 3 commercial plate readers. This application is currently been optimized and hold the promise of sub-nanomolar limit of detection as demonstrated by other Tb complexes.

Though this may be a limited field of study, the technologies and the newly developed Tb complex, (Corafluor, CRF) used in this paper show broad applicability of Tb to NPs TG-FRET in different biosensing setups.

Chapter Five

5.0 Conclusions

This thesis highlights the importance of nanomaterials for bioimaging and biosensing applications and the energy transfer mechanisms that gives them such useful optical properties.

The spectroscopic analysis of AuNC-NPs with different loadings of AuNCs has helped us to gain better understanding of the mechanism of luminesce of AuNCs in the SWIR region. Resonance Energy Transfer between encapsulated AuNCs is a plausible explanation for the origins of their photoluminescence quenching. Though this topic is highly debated, we hypothesised the origins AuNC photoluminescence by spectroscopic measurements of their PL lifetimes. With the understanding of the mechanism of energy transfer occurring within a nanoparticle, further studies can be carried out to tune this effect for desired PL properties and SWIR bioimaging.

The findings of the second part of this study showed that Corafluor Tb complexes (CRF) poses desirable photophysical properties to serve as an energy donor to optical nanomaterials for biosensing applications. Sub-nanomolar concentrations of biotinylated-QDs was detected using this new class of macrocyclic Tb complex. Though the immunoassay with nanobodies still require some optimization to detect EGFR. Corafluor Tb complexes have the potential of becoming a formidable FRET donor for several bioassays and for bioimaging applications. Understanding the theory behind resonance energy transfer (FRET or NSET) from lanthanides like CRF will help to develop ultrasensitive biosensors for early detection of diseases.

Optical nanomaterials have a lot of role to play in the future of bioimaging and biosensing, hence it is important to understand how to exploit their optical properties by energy transfer within them or to them as reported in this work.

References

1. Lukaszewski, Z. & Gorodkiewicz, E. Biosensors for the Determination of Protein Biomarkers. *Biosensors* **13**, 112 (2023).
2. Park, E. *et al.* Nanotechnologies for the Diagnosis and Treatment of SARS-CoV-2 and Its Variants. *Small Methods* **2300034**, 1–23 (2023).
3. Sanjay, S. T. *et al.* Biomarker detection for disease diagnosis using cost-effective microfluidic platforms. *Analyst* **140**, 7062–7081 (2015).
4. Park, J. & Ban, C. Development of a one-shot dual aptamer-based fluorescence nanosensor for rapid, sensitive, and label-free detection of periostin. *Sci Rep* **13**, 10224 (2023).
5. Rusling, J. F., Kumar, C. V., Gutkind, J. S. & Patel, V. Measurement of biomarker proteins for point-of-care early detection and monitoring of cancer. *Analyst* **135**, 2496–2511 (2010).
6. Cremer, M. *Über Die Ursache Der Elektromotorischen Eigenschaften Der Gewebe, Zugleich Ein Beitrag Zur Lehre von Den Polyphasischen Elektrolytketten*. (R. Oldenbourg, 1906).
7. Mehrotra, P. Biosensors and their applications – A review. *J Oral Biol Craniofac Res* **6**, 153–159 (2016).
8. Bhalla, N., Jolly, P., Formisano, N. & Estrela, P. Introduction to biosensors. *Essays Biochem* **60**, 1–8 (2016).
9. Das, T. R., Patra, S., Govender, P. P. & Shukla, S. K. Chapter 1 - Biosensors: principle, fundamentals history, recent trends and applications. in *Biosensors for Emerging and Re-Emerging Infectious Diseases* (eds. Das, J., Dave, S., Radhakrishnan, S. & Mohanty, P.) 1–18 (Academic Press, 2022). doi:10.1016/B978-0-323-88464-8.00010-5.
10. Heineman, W. R. & Jensen, W. B. Leland C. Clark Jr. (1918–2005). *Biosensors and Bioelectronics* **21**, 1403–1404 (2006).
11. Thevenot, D. R., Toth, K., Durst, R. A. & Wilson, G. S. Electrochemical biosensors: recommended definitions and classification. *Pure and applied chemistry* **71**, 2333–2348 (1999).

12. Thevenot, D. R., Toth, K., Durst, R. A. & Wilson, G. S. Technical report electrochemical biosensors: recommended definitions and classification. *Biosens. Bioelectron* **16**, 121–131 (2001).
13. Thévenot, D. R., Toth, K., Durst, R. A. & Wilson, G. S. Electrochemical biosensors: recommended definitions and classification. *Analytical Letters* **34**, 635–659 (2001).
14. Han, X., Xu, K., Taratula, O. & Farsad, K. Applications of nanoparticles in biomedical imaging. *Nanoscale* **11**, 799–819 (2019).
15. Croce, A. C. & Bottiroli, G. Autofluorescence Spectroscopy and Imaging: A Tool for Biomedical Research and Diagnosis. *Eur J Histochem* **58**, 2461 (2014).
16. Algar, W. R. *et al.* Quantum dots as simultaneous acceptors and donors in time-gated Förster resonance energy transfer relays: Characterization and biosensing. *Journal of the American Chemical Society* **134**, 1876–1891 (2012).
17. Bhuckory, S. *et al.* Triplexed CEA-NSE-PSA immunoassay using time-gated terbium-to-quantum dot FRET. *Molecules* **25**, (2020).
18. Chen, T. *et al.* Time Gated Luminescence Imaging of Immunolabeled Human Tissues. (2017) doi:10.1021/acs.analchem.7b02734.
19. Lakowicz, J. R. Time-Domain Lifetime Measurements. *Principles of Fluorescence Spectroscopy* 95–140 (1999) doi:10.1007/978-1-4757-3061-6_4.
20. Cardoso, M., Santos, D. & Hildebrandt, N. Trends in Analytical Chemistry Recent developments in lanthanide-to-quantum dot FRET using time-gated fluorescence detection and photon upconversion. *Trends in Analytical Chemistry* **84**, 60–71 (2016).
21. Qiu, X., Xu, J., Cardoso Dos Santos, M. & Hildebrandt, N. Multiplexed Biosensing and Bioimaging Using Lanthanide-Based Time-Gated Förster Resonance Energy Transfer. *Accounts of Chemical Research* (2022) doi:10.1021/acs.accounts.1c00691.

22. Payne, N. C., Kalyakina, A. S., Singh, K., Tye, M. A. & Mazitschek, R. Bright and stable luminescent probes for target engagement profiling in live cells. *Nature Chemical Biology* **17**, 1168–1177 (2021).
23. CAB. What is Bioimaging? https://cab.ku.dk/what_is_bioimaging/ (2011).
24. James, M. L. & Gambhir, S. S. A Molecular Imaging Primer: Modalities, Imaging Agents, and Applications. *Physiological Reviews* **92**, 897–965 (2012).
25. Moseley, M. & Donnan, G. Multimodality Imaging: Introduction. *Stroke* **35**, 2632–2634 (2004).
26. Veiseh, O. *et al.* Optical and MRI Multifunctional Nanoprobe for Targeting Gliomas. *Nano Lett.* **5**, 1003–1008 (2005).
27. Lahoti, H. S. & Jogdand, S. D. Bioimaging: Evolution, Significance, and Deficit. *Cureus* **14**, e28923.
28. Croce, A. C. & Bottiroli, G. Autofluorescence Spectroscopy for Monitoring Metabolism in Animal Cells and Tissues. *Methods Mol Biol* **1560**, 15–43 (2017).
29. Zhu, S., Tian, R., Antaris, A. L., Chen, X. & Dai, H. Near-Infrared-II Molecular Dyes for Cancer Imaging and Surgery. *Advanced Materials* **31**, 1900321 (2019).
30. Hong, G., Antaris, A. L. & Dai, H. Near-infrared fluorophores for biomedical imaging. *Nature Biomedical Engineering* **1**, (2017).
31. Hu, J. Y. *et al.* Highly near-IR emissive ytterbium(iii) complexes with unprecedented quantum yields. *Chemical Science* **8**, 2702–2709 (2017).
32. Reisch, A. & Klymchenko, A. S. Fluorescent Polymer Nanoparticles Based on Dyes: Seeking Brighter Tools for Bioimaging. *Small* **12**, 1968–1992 (2016).
33. Chou, K. F. & Dennis, A. M. Förster Resonance Energy Transfer between Quantum Dot Donors and Quantum Dot Acceptors. *Sensors* **15**, 13288–13325 (2015).
34. Hallaj, T. *et al.* Terbium-to-quantum dot Förster resonance energy transfer for homogeneous and sensitive detection of histone methyltransferase activity. *Nanoscale* **12**, 13719–13730 (2020).

35. Hildebrandt, N. *et al.* Energy Transfer with Semiconductor Quantum Dot Bioconjugates : A Versatile Platform for Biosensing , Energy Harvesting , and Other Developing Applications. (2017) doi:10.1021/acs.chemrev.6b00030.
36. Geissler, D., Hildebrandt, N., Charbonnière, L. J., Ziessel, R. F. & Löhmannsröben, H.-G. Quantum dots as FRET acceptors for highly sensitive multiplexing immunoassays. *Colloidal Quantum Dots for Biomedical Applications IV* **7189**, 71890L (2009).
37. Chen, C. *et al.* Single-Nanoparticle Cell Barcoding by Tunable FRET from Lanthanides to Quantum Dots. *Angewandte Chemie - International Edition* **57**, 13686–13690 (2018).
38. Rees, K. *et al.* Dextran-Functionalized Semiconductor Quantum Dot Bioconjugates for Bioanalysis and Imaging. (2020) doi:10.1021/acs.bioconjchem.0c00019.
39. The Nobel Prize in Chemistry 2023. *NobelPrize.org* https://www.nobelprize.org/prizes/chemistry/2023/popular-information/.
40. Huang, X. & El-sayed, M. A. Gold nanoparticles : Optical properties and implementations in cancer diagnosis and photothermal therapy. 13–28 (2010) doi:10.1016/j.jare.2010.02.002.
41. Baldeck, P. L. *et al.* Ultrabright and bleaching-resistant hybrid gold nanoparticles for confocal and two-photon fluorecence imaging. in (eds. Achilefu, S. & Raghavachari, R.) 89560T (San Francisco, California, United States, 2014). doi:10.1117/12.2039479.
42. Baffou, G. Gold nanoparticles as nanosources of heat. *Photoniques* 42–47 (2018) doi:10.1051/photon/2018S342.
43. António, M. *et al.* Gold nanoparticle probes for colorimetric detection of plasma galectin-3: a simple and rapid approach. *Anal. Methods* **15**, 2905–2914 (2023).
44. Ren, Z. *et al.* A Metal–Polyphenol-Coordinated Nanomedicine for Synergistic Cascade Cancer Chemotherapy and Chemodynamic Therapy. *Advanced Materials* **32**, 1906024 (2020).
45. Naresh, V. & Lee, N. A Review on Biosensors and Recent Development of Nanostructured Materials-Enabled Biosensors. *Sensors* **21**, 1109 (2021).

46. Kumar, V., Bhatt, D., Saruchi & Pandey, S. Luminescence nanomaterials for biosensing applications. *Luminescence* **38**, 1011–1025 (2023).

47. Kumar, S. *et al.* Optically Active Nanomaterials and Its Biosensing Applications—A Review. *Biosensors* **13**, 85 (2023).

48. Prats, M. Fluorescence resonance energy transfer (FRET): theory and experiments. **26**, (1998).

49. Lakowicz, J. R. *Principles of Fluorescence Spectroscopy*. *Principles of Fluorescence Spectroscopy* (2006). doi:10.1007/978-0-387-46312-4.

50. Van Der Meer, B. W. Förster Theory. in *FRET – Förster Resonance Energy Transfer* (eds. Medintz, I. & Hildebrandt, N.) 23–62 (Wiley, 2013). doi:10.1002/9783527656028.ch03.

51. Hildebrandt, N. How to Apply FRET: From Experimental Design to Data Analysis. in *FRET – Förster Resonance Energy Transfer* 105–163 (John Wiley & Sons, Ltd, 2013). doi:10.1002/9783527656028.ch05.

52. Dahal, D., Ray, P. & Pan, D. Unlocking the power of optical imaging in the second biological window: Structuring NEAR-INFRARED II materials from organic molecules to nanoparticles. *WIREs Nanomed Nanobiotechnol* **13**, e1734 (2021).

53. Projekte - SIREN – Development of the next generation of SWIR emitting probes for bioimaging. https://www.bam.de/Content/EN/Projects/SIREN/SIREN.html.

54. Musnier, B. *et al.* Optimization of spatial resolution and scattering effects for biomedical fluorescence imaging by using sub-regions of the shortwave infrared spectrum. *Journal of Biophotonics* **14**, e202000345 (2021).

55. Hong, G. *et al.* Multifunctional in vivo vascular imaging using near-infrared II fluorescence. *Nat Med* **18**, 1841–1846 (2012).

56. Robinson, J. T. *et al.* In Vivo Fluorescence Imaging in the Second Near-Infrared Window with Long Circulating Carbon Nanotubes Capable of Ultrahigh Tumor Uptake. *J. Am. Chem. Soc.* **134**, 10664–10669 (2012).

57. Zhang, Y. *et al.* Biodistribution, pharmacokinetics and toxicology of Ag2S near-infrared quantum dots in mice. *Biomaterials* **34**, 3639–3646 (2013).
58. Hong, G. *et al.* Through-skull fluorescence imaging of the brain in a new near-infrared window. *Nature Photon* **8**, 723–730 (2014).
59. Kang, S. S. *et al.* InAs on GaAs Photodetectors Using Thin InAlAs Graded Buffers and Their Application to Exceeding Short-Wave Infrared Imaging at 300 K. *Sci Rep* **9**, 12875 (2019).
60. Yang, Q. *et al.* Rational Design of Molecular Fluorophores for Biological Imaging in the NIR-II Window. *Adv Mater* **29**, (2017).
61. Zhang, M. *et al.* Bright quantum dots emitting at ∼1,600 nm in the NIR-IIb window for deep tissue fluorescence imaging. *Proc Natl Acad Sci U S A* **115**, 6590–6595 (2018).
62. Fan, Y. & Zhang, F. A New Generation of NIR-II Probes: Lanthanide-Based Nanocrystals for Bioimaging and Biosensing. *Advanced Optical Materials* **7**, 1801417 (2019).
63. Vardaki, M. Z. & Kourkoumelis, N. Tissue Phantoms for Biomedical Applications in Raman Spectroscopy: A Review. *Biomed Eng Comput Biol* **11**, 1179597220948100 (2020).
64. Water absorption spectrum. https://water.lsbu.ac.uk/water/water_vibrational_spectrum.html.
65. Wo'zniak, B. & Dera, J. *Light Absorption in Sea Water*. *Light Absorption in Sea Water* vol. 33 (2007).
66. Hong, G., Diao, S., Antaris, A. L. & Dai, H. Carbon Nanomaterials for Biological Imaging and Nanomedicinal Therapy. *Chem. Rev.* **115**, 10816–10906 (2015).
67. European Commission. Directorate General for Health and Consumers. *Health Effects of Artificial Light.* (Publications Office, LU, 2012).
68. WEBB, A. R., DECOSTA, B. R. & HOLICK, M. F. Sunlight Regulates the Cutaneous Production of Vitamin D3 by Causing Its Photodegradation*. *The Journal of Clinical Endocrinology & Metabolism* **68**, 882–887 (1989).

69. Hori, M., Shibuya, K., Sato, M. & Saito, Y. Lethal effects of short-wavelength visible light on insects. *Sci Rep* **4**, 7383 (2014).

70. Chen, G., Qiu, H., Prasad, P. N. & Chen, X. Upconversion Nanoparticles: Design, Nanochemistry, and Applications in Theranostics. *Chem. Rev.* **114**, 5161–5214 (2014).

71. Chen, G. *et al.* Advanced Near-Infrared Light for Monitoring and Modulating the Spatiotemporal Dynamics of Cell Functions in Living Systems. *Adv Sci (Weinh)* **7**, 1903783 (2020).

72. Ntziachristos, V., Ripoll, J., Wang, L. V. & Weissleder, R. Looking and listening to light: the evolution of whole-body photonic imaging. *Nat Biotechnol* **23**, 313–320 (2005).

73. Naumova, A. V., Modo, M., Moore, A., Murry, C. E. & Frank, J. A. Clinical imaging in regenerative medicine. *Nat Biotechnol* **32**, 804–818 (2014).

74. Smith, A. M., Mancini, M. C. & Nie, S. Second window for in vivo imaging. *Nature Nanotech* **4**, 710–711 (2009).

75. Welsher, K. *et al.* A route to brightly fluorescent carbon nanotubes for near-infrared imaging in mice. *Nature Nanotech* **4**, 773–780 (2009).

76. *Fluorescence Spectroscopy in Biology: Advanced Methods and Their Applications to Membranes, Proteins, DNA, and Cells*. vol. 3 (Springer, Berlin, Heidelberg, 2005).

77. Antaris, A. L. *et al.* A high quantum yield molecule-protein complex fluorophore for near-infrared II imaging. *Nat Commun* **8**, 15269 (2017).

78. Kobayashi, H., Ogawa, M., Alford, R., Choyke, P. L. & Urano, Y. New Strategies for Fluorescent Probe Design in Medical Diagnostic Imaging. *Chem. Rev.* **110**, 2620–2640 (2010).

79. Cao, J. *et al.* Recent Progress in NIR-II Contrast Agent for Biological Imaging. **7**, 1–21 (2020).

80. Cao, J. *et al.* Recent Progress in NIR-II Contrast Agent for Biological Imaging. *Frontiers in Bioengineering and Biotechnology* **7**, (2020).

81. Lei, Z. *et al.* Stable, Wavelength-Tunable Fluorescent Dyes in the NIR-II Region for In Vivo High-Contrast Bioimaging and Multiplexed Biosensing. *Angewandte Chemie International Edition* **58**, 8166–8171 (2019).

82. Zhao, M. *et al.* NIR-II pH Sensor with a FRET Adjustable Transition Point for In Situ Dynamic Tumor Microenvironment Visualization. *Angewandte Chemie International Edition* **60**, 5091–5095 (2021).

83. David, S. *et al.* Benzothiadiazole-Substituted Aza-BODIPY Dyes: Two-Photon Absorption Enhancement for Improved Optical Limiting Performances in the Short-Wave IR Range. *Chemistry – A European Journal* **27**, 3517–3525 (2021).

84. Louie, A. Multimodality Imaging Probes: Design and Challenges. *Chem. Rev.* **110**, 3146–3195 (2010).

85. Semonin, O. E. *et al.* Absolute Photoluminescence Quantum Yields of IR-26 Dye, PbS, and PbSe Quantum Dots. *J. Phys. Chem. Lett.* **1**, 2445–2450 (2010).

86. Sun, Y. *et al.* Strained Cyclooctyne as a Molecular Platform for Construction of Multimodal Imaging Probes. *Angew Chem Int Ed* **54**, 5981–5984 (2015).

87. Thimsen, E., Sadtler, B. & Berezin, M. Y. Shortwave-infrared (SWIR) emitters for biological imaging: a review of challenges and opportunities. *Nanophotonics* **6**, 1043–1054 (2017).

88. Davis, N. K. S., Thompson, A. L. & Anderson, H. L. A Porphyrin Fused to Four Anthracenes. *J. Am. Chem. Soc.* **133**, 30–31 (2011).

89. Piwoński, H., Nozue, S. & Habuchi, S. The Pursuit of Shortwave Infrared-Emitting Nanoparticles with Bright Fluorescence through Molecular Design and Excited-State Engineering of Molecular Aggregates. *ACS Nanosci. Au* **2**, 253–283 (2022).

90. Carr, J. A. *et al.* Shortwave infrared fluorescence imaging with the clinically approved near-infrared dye indocyanine green. *Proceedings of the National Academy of Sciences* **115**, 4465–4470 (2018).

91. Tao, Z. *et al.* Biological Imaging Using Nanoparticles of Small Organic Molecules with Fluorescence Emission at Wavelengths Longer than 1000 nm. *Angewandte Chemie International Edition* **52**, 13002–13006 (2013).

92. Hong, G. *et al.* Ultrafast fluorescence imaging in vivo with conjugated polymer fluorophores in the second near-infrared window. *Nat Commun* **5**, 4206 (2014).

93. Bünzli, J.-C. G. Lanthanide Luminescence for Biomedical Analyses and Imaging. *Chem. Rev.* **110**, 2729–2755 (2010).

94. Naczynski, D. J. *et al.* Rare-earth-doped biological composites as in vivo shortwave infrared reporters. *Nat Commun* **4**, 2199 (2013).

95. Zhang, T. *et al.* Water-Soluble Mitochondria-Specific Ytterbium Complex with Impressive NIR Emission. *J. Am. Chem. Soc.* **133**, 20120–20122 (2011).

96. Trivedi, E. R. *et al.* Highly Emitting Near-Infrared Lanthanide "Encapsulated Sandwich" Metallacrown Complexes with Excitation Shifted Toward Lower Energy. *J. Am. Chem. Soc.* **136**, 1526–1534 (2014).

97. Chow, C. Y. *et al.* Ga3+/Ln3+ Metallacrowns: A Promising Family of Highly Luminescent Lanthanide Complexes That Covers Visible and Near-Infrared Domains. *J. Am. Chem. Soc.* **138**, 5100–5109 (2016).

98. Martinić, I., Eliseeva, S. V., Nguyen, T. N., Pecoraro, V. L. & Petoud, S. Near-Infrared Optical Imaging of Necrotic Cells by Photostable Lanthanide-Based Metallacrowns. *J. Am. Chem. Soc.* **139**, 8388–8391 (2017).

99. Peng, X.-X., Zhu, X.-F. & Zhang, J.-L. Near Infrared (NIR) imaging: Exploring biologically relevant chemical space for lanthanide complexes. *Journal of Inorganic Biochemistry* **209**, 111118 (2020).

100. Sahoo, S., Mondal, S. & Sarma, D. Luminescent Lanthanide Metal Organic Frameworks (LnMOFs): A Versatile Platform towards Organomolecule Sensing. *Coordination Chemistry Reviews* **470**, 214707 (2022).

101. Zhang, R., Zhu, L. & Yue, B. Luminescent properties and recent progress in applications of lanthanide metal-organic frameworks. *Chinese Chemical Letters* **34**, 108009 (2023).

102. Sark, W. G. J. H. M. van *et al.* Solar Spectrum Conversion for Photovoltaics Using Nanoparticles. in *Third Generation Photovoltaics* (IntechOpen, 2012). doi:10.5772/39213.

103. Liang, Y. *et al.* Extending the applications for lanthanide ions: efficient emitters in short-wave infrared persistent luminescence. *J. Mater. Chem. C* **5**, 6488–6492 (2017).

104. Pini, F., Francés-Soriano, L., Andrigo, V., Natile, M. M. & Hildebrandt, N. Optimizing Upconversion Nanoparticles for FRET Biosensing. *ACS Nano* **17**, 4971–4984 (2023).

105. Ema, M., Gamo, M. & Honda, K. A review of toxicity studies of single-walled carbon nanotubes in laboratory animals. *Regulatory Toxicology and Pharmacology* **74**, 42–63 (2016).

106. Jin, T. Critical Review—Recent Progress in NIR Fluorophores Emitting over 1000 nm for Bioimaging. *ECS J. Solid State Sci. Technol.* **8**, R9 (2019).

107. Kam, N. W. S., O'Connell, M., Wisdom, J. A. & Dai, H. Carbon nanotubes as multifunctional biological transporters and near-infrared agents for selective cancer cell destruction. *Proceedings of the National Academy of Sciences* **102**, 11600–11605 (2005).

108. Prencipe, G. *et al.* PEG Branched Polymer for Functionalization of Nanomaterials with Ultralong Blood Circulation. *J. Am. Chem. Soc.* **131**, 4783–4787 (2009).

109. O'Connell, M. J. *et al.* Band Gap Fluorescence from Individual Single-Walled Carbon Nanotubes. *Science* **297**, 593–596 (2002).

110. Crochet, J., Clemens, M. & Hertel, T. Quantum Yield Heterogeneities of Aqueous Single-Wall Carbon Nanotube Suspensions. *J. Am. Chem. Soc.* **129**, 8058–8059 (2007).

111. Avouris, P., Freitag, M. & Perebeinos, V. Carbon-nanotube photonics and optoelectronics. *Nature Photon* **2**, 341–350 (2008).

112. Zhang, Y. *et al.* Ag2S Quantum Dot: A Bright and Biocompatible Fluorescent Nanoprobe in the Second Near-Infrared Window. *ACS Nano* **6**, 3695–3702 (2012).

113. Hong, G. *et al.* In vivo fluorescence imaging with Ag2S quantum dots in the second near-infrared region. *Angew Chem Int Ed Engl* **51**, 9818–9821 (2012).

114. Bruns, O. T. *et al.* Next-generation in vivo optical imaging with short-wave infrared quantum dots. *Nat Biomed Eng* **1**, 1–11 (2017).

115. Jin, R., Li, G., Sharma, S., Li, Y. & Du, X. Toward Active-Site Tailoring in Heterogeneous Catalysis by Atomically Precise Metal Nanoclusters with Crystallographic Structures. *Chem. Rev.* **121**, 567–648 (2021).

116. Omoda, T., Takano, S. & Tsukuda, T. Toward Controlling the Electronic Structures of Chemically Modified Superatoms of Gold and Silver. *Small* **17**, 2001439 (2021).

117. Xia, N. & Wu, Z. Controlling ultrasmall gold nanoparticles with atomic precision. *Chem. Sci.* **12**, 2368–2380 (2021).

118. Ni, S., Liu, Y., Tong, S., Li, S. & Song, X. Emerging NIR-II Luminescent Gold Nanoclusters for In Vivo Bioimaging. *J. Anal. Test.* **7**, 260–271 (2023).

119. Liu, Z., Luo, L. & Jin, R. Visible to NIR-II Photoluminescence of Atomically Precise Gold Nanoclusters. *Advanced Materials* **n/a**, 2309073.

120. Jin, R. Quantum sized, thiolate-protected gold nanoclusters. *Nanoscale* **2**, 343–362 (2010).

121. Chen, Y. *et al.* Shortwave Infrared in Vivo Imaging with Gold Nanoclusters. *Nano Lett.* **17**, 6330–6334 (2017).

122. Yu, Q. *et al.* Luminescent gold nanocluster-based sensing platform for accurate H2S detection in vitro and in vivo with improved anti-interference. *Light Sci Appl* **6**, e17107–e17107 (2017).

123. Hembury, M. *et al.* Luminescent Gold Nanocluster-Decorated Polymeric Hybrid Particles with Assembly-Induced Emission. *Biomacromolecules* **19**, 2841–2848 (2018).

124. Li, H., Li, H. & Wan, A. Luminescent gold nanoclusters for in vivo tumor imaging. *Analyst* **145**, 348–363 (2020).

125. Yang, T.-Q. *et al.* Origin of the Photoluminescence of Metal Nanoclusters: From Metal-Centered Emission to Ligand-Centered Emission. *Nanomaterials* **10**, 261 (2020).

126. Yu, Z. *et al.* High-Resolution Shortwave Infrared Imaging of Vascular Disorders Using Gold Nanoclusters. *ACS nano* **14**, 4973–4981 (2020).

127. Tahir *et al.* Quenching of the Photoluminescence of Gold Nanoclusters Synthesized by Pulsed Laser Ablation in Water upon Interaction with Toxic Metal Species in Aqueous Solution. *Chemosensors* **11**, 118 (2023).

128. Link, S. *et al.* Visible to Infrared Luminescence from a 28-Atom Gold Cluster. *J. Phys. Chem. B* **106**, 3410–3415 (2002).

129. Kang, X., Chong, H. & Zhu, M. Au25(SR)18: the captain of the great nanocluster ship. *Nanoscale* **10**, 10758–10834 (2018).

130. Haye, L. *et al.* Enhancing Near Infrared II Emission of Gold Nanoclusters via Encapsulation in Small Polymer Nanoparticles. (2022) doi:10.1002/adom.202201474.

131. Kelkar, S. S. & Reineke, T. M. Theranostics: Combining Imaging and Therapy. *Bioconjugate Chem.* **22**, 1879–1903 (2011).

132. Dan, Q. *et al.* Gold Nanoclusters-Based NIR-II Photosensitizers with Catalase-like Activity for Boosted Photodynamic Therapy. *Pharmaceutics* **14**, 1645 (2022).

133. Chen, S. *et al.* Gold Nanoclusters for Tumor Diagnosis and Treatment. *Advanced NanoBiomed Research* **3**, 2300082 (2023).

134. Porret, E., Guével, X. L. & Coll, J.-L. Gold nanoclusters for biomedical applications: toward in vivo studies. *J. Mater. Chem. B* **8**, 2216–2232 (2020).

135. Mussa Farkhani, S. *et al.* Tailoring gold nanocluster properties for biomedical applications: From sensing to bioimaging and theranostics. *Progress in Materials Science* **142**, 101229 (2024).

136. Mordini, D. *et al.* Luminescent Gold Nanoclusters for Bioimaging: Increasing the Ligand Complexity. *Nanomaterials* **13**, 648 (2023).

137. Xie, J., Zheng, Y. & Ying, J. Y. Protein-Directed Synthesis of Highly Fluorescent Gold Nanoclusters. *J. Am. Chem. Soc.* **131**, 888–889 (2009).

138. Shang, L. *et al.* One-Pot Synthesis of Near-Infrared Fluorescent Gold Clusters for Cellular Fluorescence Lifetime Imaging. *Small* **7**, 2614–2620 (2011).

139. Zheng, J., Zhou, C., Yu, M. & Liu, J. Different sized luminescent gold nanoparticles. *Nanoscale* **4**, 4073–4083 (2012).

140. Luo, Z. *et al.* From Aggregation-Induced Emission of Au(I)–Thiolate Complexes to Ultrabright Au(0)@Au(I)–Thiolate Core–Shell Nanoclusters. *J. Am. Chem. Soc.* **134**, 16662–16670 (2012).

141. Zhou, R., Shi, M., Chen, X., Wang, M. & Chen, H. Atomically Monodispersed and Fluorescent Sub-Nanometer Gold Clusters Created by Biomolecule-Assisted Etching of Nanometer-Sized Gold Particles and Rods. *Chemistry – A European Journal* **15**, 4944–4951 (2009).

142. Jin, R., Zeng, C., Zhou, M. & Chen, Y. Atomically Precise Colloidal Metal Nanoclusters and Nanoparticles: Fundamentals and Opportunities. *Chem. Rev.* **116**, 10346–10413 (2016).

143. Zhang, C. *et al.* Advances of gold nanoclusters for bioimaging. *iScience* **25**, (2022).

144. Zhu, M., Aikens, C. M., Hollander, F. J., Schatz, G. C. & Jin, R. Correlating the Crystal Structure of A Thiol-Protected Au_{25} Cluster and Optical Properties. *J. Am. Chem. Soc.* **130**, 5883–5885 (2008).

145. Heaven, M. W., Dass, A., White, P. S., Holt, K. M. & Murray, R. W. Crystal structure of the gold nanoparticle $[N(C_8H_{17})_4][Au_{25}(SCH_2CH_2Ph)_{18}]$. *Journal of the American Chemical Society* **130**, 3754–3755 (2008).

146. Zheng, J., Nicovich, P. R. & Dickson, R. M. Highly Fluorescent Noble-Metal Quantum Dots. *Annual Review of Physical Chemistry* **58**, 409–431 (2007).

147. Jiang, D.-E., Kühn, M., Tang, Q. & Weigend, F. Superatomic Orbitals under Spin-Orbit Coupling. *J Phys Chem Lett* **5**, 3286–3289 (2014).

148. Zhou, M. *et al.* Three-Stage Evolution from Nonscalable to Scalable Optical Properties of Thiolate-Protected Gold Nanoclusters. *J. Am. Chem. Soc.* **141**, 19754–19764 (2019).

149. Zhou, M., Zeng, C., Li, Q., Higaki, T. & Jin, R. Gold Nanoclusters: Bridging Gold Complexes and Plasmonic Nanoparticles in Photophysical Properties. *Nanomaterials* **9**, 933 (2019).

150. Noginov, M. A., Zhu, G. & Gavrilenko, V. I. Sensitized nonlinear emission of gold nanoparticles. *Opt. Express, OE* **15**, 15648–15655 (2007).

151. Lin, C.-A. J., Lee, C.-H., Yeh, H.-I. & Chang, W. H. Fluorescent Gold Nanoclusters for Biomedical Applications. in *World Congress on Medical Physics and Biomedical Engineering, September 7 - 12, 2009, Munich, Germany* (eds. Dössel, O. & Schlegel, W. C.) 108–111 (Springer, Berlin, Heidelberg, 2010). doi:10.1007/978-3-642-03887-7_30.

152. Valeur, B. Molecular Fluorescence Principles and Applications. *Molecular Fluorescence* (2001).

153. Lin, C.-A. J. *et al.* Synthesis, characterization, and bioconjugation of fluorescent gold nanoclusters toward biological labeling applications. *ACS Nano* **3**, 395–401 (2009).

154. Baryshnikov, G., Minaev, B. & Ågren, H. Theory and Calculation of the Phosphorescence Phenomenon. *Chem. Rev.* **117**, 6500–6537 (2017).

155. Xie, X.-Y. *et al.* Near-Infrared Dual-Emission of a Thiolate-Protected Au42 Nanocluster: Excited States, Nonradiative Rates, and Mechanism. *J. Phys. Chem. Lett.* **14**, 10025–10031 (2023).

156. Zhang, Q. *et al.* Efficient blue organic light-emitting diodes employing thermally activated delayed fluorescence. *Nature Photon* **8**, 326–332 (2014).

157. Ravinson, D. S. M. & Thompson, M. E. Thermally assisted delayed fluorescence (TADF): fluorescence delayed is fluorescence denied. *Mater. Horiz.* **7**, 1210–1217 (2020).

158. Yonemoto, D. T., Papa, C. M., Mongin, C. & Castellano, F. N. Thermally Activated Delayed Photoluminescence: Deterministic Control of Excited-State Decay. *J. Am. Chem. Soc.* **142**, 10883–10893 (2020).

159. Kitagawa, Y. *et al.* Thermally-assisted photosensitized emission in a trivalent terbium complex. *Commun Chem* **6**, 1–5 (2023).

160. Eng, M. P., Ljungdahl, T., Andréasson, J., Mårtensson, J. & Albinsson, B. Triplet Photophysics of Gold(III) Porphyrins. *J. Phys. Chem. A* **109**, 1776–1784 (2005).

161. Shafikov, M. Z., Daniels, R. & Kozhevnikov, V. N. Unusually Fast Phosphorescence from Ir(III) Complexes via Dinuclear Molecular Design. *J Phys Chem Lett* **10**, 7015–7024 (2019).

162. Mitsui, M. *et al.* Charge-Transfer-Mediated Mechanism Dominates Oxygen Quenching of Ligand-Protected Noble-Metal Cluster Photoluminescence. *J. Phys. Chem. Lett.* **13**, 9272–9278 (2022).

163. Chen, L.-Y., Wang, C.-W., Yuan, Z. & Chang, H.-T. Fluorescent Gold Nanoclusters: Recent Advances in Sensing and Imaging. *Anal. Chem.* **87**, 216–229 (2015).

164. Zhou, M. & Song, Y. Origins of Visible and Near-Infrared Emissions in [Au25(SR)18]− Nanoclusters. *J. Phys. Chem. Lett.* **12**, 1514–1519 (2021).

165. Li, Q. *et al.* Structural distortion and electron redistribution in dual-emitting gold nanoclusters. *Nat Commun* **11**, 2897 (2020).

166. Si, W.-D. *et al.* Two triplet emitting states in one emitter: Near-infrared dual-phosphorescent Au20 nanocluster. *Science Advances* **9**, eadg3587 (2023).

167. Pyo, K. *et al.* Ultrabright Luminescence from Gold Nanoclusters: Rigidifying the Au(I)–Thiolate Shell. *J. Am. Chem. Soc.* **137**, 8244–8250 (2015).

168. Huang, Y., Fuksman, L. & Zheng, J. Luminescence mechanisms of ultrasmall gold nanoparticles. doi:10.1039/c8dt00420j.

169. Guével, X. L. *et al.* Tailoring the SWIR emission of gold nanoclusters by surface ligand rigidification and their application in 3D bioimaging. *Chem. Commun.* **58**, 2967–2970 (2022).

170. Le Guével, X. *et al.* High photostability and enhanced fluorescence of gold nanoclusters by silver doping. *Nanoscale* **4**, 7624 (2012).

171. Forster, Th. Energiewanderung und Fluoreszenz. *Naturwissenschaften* **33**, 166–175 (1946).

172. Förster, Th. Zwischenmolekulare Energiewanderung und Fluoreszenz. *Annalen der Physik* **437**, 55–75 (1948).

173. Clegg, R. M. The History of Fret. in *Reviews in Fluorescence 2006* (eds. Geddes, C. D. & Lakowicz, J. R.) 1–45 (Springer US, Boston, MA, 2006). doi:10.1007/0-387-33016-X_1.

174. Kong, Y., Liu, D., Guo, X. & Chen, X. Fluorescence detection of three types of pollutants based on fluorescence resonance energy transfer and its comparison with colorimetric detection. *RSC Advances* **13**, 22043–22053 (2023).

175. Hildebrandt, N., Charbonnière, L. J. & Löhmannsröben, H.-G. Time-Resolved Analysis of a Highly Sensitive Förster Resonance Energy Transfer Immunoassay Using Terbium Complexes as Donors and Quantum Dots as Acceptors. *Journal of Biomedicine and Biotechnology* **2007**, 079169 (2007).

176. Sapsford, K. E., Berti, L. & Medintz, I. L. Materials for Fluorescence Resonance Energy Transfer Analysis: Beyond Traditional Donor–Acceptor Combinations. *Angewandte Chemie International Edition* **45**, 4562–4589 (2006).

177. David Wegner, K. *et al.* Influence of Luminescence Quantum Yield, Surface Coating, and Functionalization of Quantum Dots on the Sensitivity of Time-Resolved FRET Bioassays. *ACS Applied Materials & Interfaces* **5**, 2881–2892 (2013).

178. Qiao, Y., Luo, Y., Long, N., Xing, Y. & Tu, J. Single-molecular förster resonance energy transfer measurement on structures and interactions of biomolecules. *Micromachines* **12**, 1–22 (2021).

179. Luo, H. *et al.* Correlative super-resolution bright-field and fluorescence imaging by microsphere assisted microscopy. *Nanoscale* (2023) doi:10.1039/D3NR04096H.

180. Selvin, P. R. [13] Fluorescence resonance energy transfer. in *Methods in Enzymology* vol. 246 300–334 (Elsevier, 1995).

181. Fluorescence Resonance Energy Transfer (FRET) Microscopy - Introductory Concepts | Olympus LS. https://www.olympus-lifescience.com/en/microscope-resource/primer/techniques/fluorescence/fret/fretintro/.

182. Szalai, A. M. *et al.* Super-resolution Imaging of Energy Transfer by Intensity-Based STED-FRET. *Nano Lett.* **21**, 2296–2303 (2021).

183. Sekar, R. B. & Periasamy, A. Fluorescence resonance energy transfer (FRET) microscopy imaging of live cell protein localizations. *Journal of Cell Biology* **160**, 629–633 (2003).

184. Ahmad, A. I. & Ghasemi, J. B. New FRET primers for quantitative real-time PCR. *Anal Bioanal Chem* **387**, 2737–2743 (2007).

185. Nath-Chowdhury, M. *et al.* Real-time PCR using FRET technology for Old World cutaneous leishmaniasis species differentiation. *Parasites & Vectors* **9**, 255 (2016).

186. Rudkouskaya, A. *et al.* Multiplexed non-invasive tumor imaging of glucose metabolism and receptor-ligand engagement using dark quencher FRET acceptor. *Theranostics* **10**, 10309–10325 (2020).

187. Fu, H.-J. *et al.* Enzyme-Induced Silver Deposition on Gold Nanorods for Naked-Eye and Smartphone Detection of Acrylamide in Food. *ACS Appl. Nano Mater.* **5**, 12915–12925 (2022).

188. Zhang, Q. *et al.* An AIEgen/graphene oxide nanocomposite (AIEgen@GO)-based two-stage “turn-on” nucleic acid biosensor for rapid detection of SARS-CoV-2 viral sequence. *Aggregate* **4**, e195 (2023).

189. Berney, C. & Danuser, G. FRET or No FRET: A Quantitative Comparison. *Biophysical Journal* **84**, 3992–4010 (2003).

190. Arppe, R., Carro-Temboury, M. R., Hempel, C., Vosch, T. & Just Sørensen, T. Investigating dye performance and crosstalk in fluorescence enabled bioimaging using a model system. *PLoS One* **12**, e0188359 (2017).

191. Wang, Q. *et al.* Proximity-Dependent Switchable ATP Aptasensors Utilizing a High-Performance FRET Reporter. *ACS Appl. Mater. Interfaces* **13**, 9359–9368 (2021).

192. Liang, Z. *et al.* Ratiometric FRET Encoded Hierarchical ZrMOF @ Au Cluster for Ultrasensitive Quantifying MicroRNA In Vivo. *Adv Mater* **34**, e2107449 (2022).

193. Resch-Genger, U., Grabolle, M., Cavaliere-Jaricot, S., Nitschke, R. & Nann, T. Quantum dots versus organic dyes as fluorescent labels. *Nat Methods* **5**, 763–775 (2008).

194. Tian, F., Xu, G., Zhou, S., Chen, S. & He, D. Principles and applications of green fluorescent protein-based biosensors: a mini-review. *Analyst* **148**, 2882–2891 (2023).

195. Palmer, A. E., Qin, Y., Park, J. G. & McCombs, J. E. Design and application of genetically encoded biosensors. *Trends in Biotechnology* **29**, 144–152 (2011).

196. Bajar, B. T., Wang, E. S., Zhang, S., Lin, M. Z. & Chu, J. A Guide to Fluorescent Protein FRET Pairs. *Sensors (Basel)* **16**, 1488 (2016).

197. Shen, X., Xu, W., Ouyang, J. & Na, N. Fluorescence resonance energy transfer-based nanomaterials for the sensing in biological systems. *Chinese Chemical Letters* **33**, 4505–4516 (2022).

198. Malik, S. *et al.* Nanomaterials-based biosensor and their applications: A review. *Heliyon* **9**, e19929 (2023).

199. Yun, C. S. *et al.* Nanometal Surface Energy Transfer in Optical Rulers, Breaking the FRET Barrier. *J. Am. Chem. Soc.* **127**, 3115–3119 (2005).

200. Pons, T. *et al.* On the Quenching of Semiconductor Quantum Dot Photoluminescence by Proximal Gold Nanoparticles. *Nano Lett.* **7**, 3157–3164 (2007).

201. Cardoso Dos Santos, M., Algar, W. R., Medintz, I. L. & Hildebrandt, N. Quantum dots for Förster Resonance Energy Transfer (FRET). *TrAC - Trends in Analytical Chemistry* **125**, 115819 (2020).

202. Verma, A. K., Noumani, A., Yadav, A. K. & Solanki, P. R. FRET Based Biosensor: Principle Applications Recent Advances and Challenges. *Diagnostics* **13**, 1375 (2023).

203. Efros, Al. L. & Efros, A. Interband Light Absorption in Semiconductor Spheres. *Soviet physics. Semiconductors* **16**, 772–775 (1982).

204. Ekimov, A. I., Efros, L. & Onushchenko, A. A. QUANTUM SIZE EFFECT IN SEMICONDUCTOR MICROCRYSTALS.

205. Rossetti, R., Nakahara, S. & Brus, L. E. Quantum size effects in the redox potentials, resonance Raman spectra, and electronic spectra of CdS crystallites in aqueous solution. *The Journal of Chemical Physics* **79**, 1086–1088 (1983).

206. Murray, C. B., Norris, D. J. & Bawendi, M. G. Synthesis and characterization of nearly monodisperse CdE (E = sulfur, selenium, tellurium) semiconductor nanocrystallites. *J. Am. Chem. Soc.* **115**, 8706–8715 (1993).

207. Chan, W. C. W. & Nie, S. Quantum Dot Bioconjugates for Ultrasensitive Nonisotopic Detection. *Science* **281**, 2016–2018 (1998).

208. Bruchez, M., Moronne, M., Gin, P., Weiss, S. & Alivisatos, A. P. Semiconductor Nanocrystals as Fluorescent Biological Labels. *Science* **281**, 2013–2016 (1998).

209. Girma, W., Fahmi, Z., Permadi, A., Abate, M. & Chang, J.-Y. Synthetic strategies and biomedical applications of I-III-VI ternary quantum dots. *J. Mater. Chem. B* **5**, (2017).

210. Li, L. *et al.* A review of nanomaterials for biosensing applications. *J. Mater. Chem. B* 10.1039.D3TB02648E (2024) doi:10.1039/D3TB02648E.

211. Saha, K., Agasti, S. S., Kim, C., Li, X. & Rotello, V. M. Gold Nanoparticles in Chemical and Biological Sensing. *Chem. Rev.* **112**, 2739–2779 (2012).

212. Dulkeith, E. *et al.* Plasmon emission in photoexcited gold nanoparticles. *Phys. Rev. B* **70**, 205424 (2004).

213. Deader, F. A. *et al.* Electric Field-Driven Self-Assembly of Gold Nanoparticle Monolayers on Silicon Substrates. *Langmuir* **39**, 15766–15772 (2023).

214. Persson, B. N. J. & Lang, N. D. Electron-hole-pair quenching of excited states near a metal. *Phys. Rev. B* **26**, 5409–5415 (1982).

215. Samani, M. T. & Hashemianzadeh, S. M. The effect of temperature and ligand structure on the solubility of gold nanoparticles. *Mater. Res. Express* **8**, 065009 (2021).

216. Chen, C., Midelet, C., Bhuckory, S., Hildebrandt, N. & Werts, M. H. V. Nanosurface Energy Transfer from Long-Lifetime Terbium Donors to Gold Nanoparticles. *Journal of Physical Chemistry C* **122**, 17566–17574 (2018).

217. Li, M. *et al.* Size-Dependent Energy Transfer between CdSe/ZnS Quantum Dots and Gold Nanoparticles. *J. Phys. Chem. Lett.* **2**, 2125–2129 (2011).

218. Deng, D., Zhang, D., Li, Y., Achilefu, S. & Gu, Y. Gold nanoparticles based molecular beacons for in vitro and in vivo detection of the matriptase expression on tumor. *Biosens Bioelectron* **49**, 216–221 (2013).

219. Guo, W. *et al.* Nanostructure and Corresponding Quenching Efficiency of Fluorescent DNA Probes. *Materials* **11**, 272 (2018).

220. Griffin, J. *et al.* Size- and Distance-Dependent Nanoparticle Surface-Energy Transfer (NSET) Method for Selective Sensing of Hepatitis C Virus RNA. *Chemistry – A European Journal* **15**, 342–351 (2009).

221. Breshike, C. J., Riskowski, R. A. & Strouse, G. F. Leaving Förster Resonance Energy Transfer Behind: Nanometal Surface Energy Transfer Predicts the Size-Enhanced Energy Coupling between a Metal Nanoparticle and an Emitting Dipole. *J. Phys. Chem. C* **117**, 23942–23949 (2013).

222. Liu, Y., Yehl, K., Narui, Y. & Salaita, K. Tension Sensing Nanoparticles for Mechano-Imaging at the Living/Nonliving Interface. *J. Am. Chem. Soc.* **135**, 5320–5323 (2013).

223. Chen, C. & Hildebrandt, N. Trends in Analytical Chemistry Resonance energy transfer to gold nanoparticles : NSET defeats FRET. *Trends in Analytical Chemistry* **123**, 115748 (2020).

224. Hildebrandt, N., Lim, M., Kim, N., Choi, D. Y. & Nam, J.-M. Plasmonic quenching and enhancement: metal–quantum dot nanohybrids for fluorescence biosensing. *Chem. Commun.* **59**, 2352–2380 (2023).

225. Jørgensen, C. B. The inner mechanism of rare earths elucidated by photo-electron spectra. in *Rare Earths* 199–253 (Springer, Berlin, Heidelberg, 1973). doi:10.1007/3-540-06125-8_4.

226. Jalali, J. & Lebeau, T. The Role of Microorganisms in Mobilization and Phytoextraction of Rare Earth Elements: A Review. *Front. Environ. Sci.* **9**, 688430 (2021).

227. Gao, M. *et al.* Lanthanides-based security inks with reversible luminescent switching and self-healing properties for advanced anti-counterfeiting. *Journal of Molecular Liquids* **350**, 118559 (2022).

228. Miluski, P., Kochanowicz, M., Zmojda, J., Ragin, T. & Dorosz, D. Spectroscopic investigation of Tb(tmhd)3 - Eu(tmhd)3 co-doped poly(methyl methacrylate) fibre. *Optical Materials* **87**, 112–116 (2019).

229. D'Aléo, A., Andraud, C. & Maury, O. Two-photon Absorption of Lanthanide Complexes: from Fundamental Aspects to Biphotonic Imaging Applications. in *Luminescence of Lanthanide Ions in Coordination Compounds and Nanomaterials* 197–230 (John Wiley & Sons, Ltd, 2014). doi:10.1002/9781118682760.ch05.

230. Teo, R. D., Termini, J. & Gray, H. B. Lanthanides: Applications in Cancer Diagnosis and Therapy. *J Med Chem* **59**, 6012–6024 (2016).

231. Bünzli, J. C. G. & Piguet, C. Taking advantage of luminescent lanthanide ions. *Chemical Society Reviews* **34**, 1048–1077 (2005).

232. Bünzli, J.-C. G. & Eliseeva, S. V. Basics of Lanthanide Photophysics. 1–45 (2010) doi:10.1007/4243_2010_3.

233. Bünzli, J.-C. G. Review: Lanthanide coordination chemistry: from old concepts to coordination polymers. *Journal of Coordination Chemistry* **67**, 3706–3733 (2014).

234. Sy, M., Nonat, A., Hildebrandt, N. & Charbonnière, L. J. Lanthanide-based luminescence biolabelling. *Chem. Commun.* **52**, 5080–5095 (2016).

235. Nosov, V. G. *et al.* Brightly Luminescent (TbxLu1−x)2bdc3·nH2O MOFs: Effect of Synthesis Conditions on Structure and Luminescent Properties. *Molecules* **28**, 2378 (2023).

236. Han, S., Deng, R., Xie, X. & Liu, X. Enhancing Luminescence in Lanthanide-Doped Upconversion Nanoparticles. *Angew Chem Int Ed* **53**, 11702–11715 (2014).

237. Bünzli, J.-C. G. On the design of highly luminescent lanthanide complexes. *Coordination Chemistry Reviews* **293–294**, 19–47 (2015).

238. Weissman, S. I. Intramolecular Energy Transfer The Fluorescence of Complexes of Europium. *The Journal of Chemical Physics* **10**, 214–217 (1942).

239. Trautnitz, M. F. K., Doffek, C. & Seitz, M. Radiative Lifetime, Non-Radiative Relaxation, and Sensitization Efficiency in Luminescent Europium and Neodymium Cryptates – The Roles of 2,2'-Bipyridine- *N,N'* -dioxide and Deuteration. *ChemPhysChem* **20**, 2179–2186 (2019).

240. Weibel, N., Charbonnière, L. J., Guardigli, M., Roda, A. & Ziessel, R. Engineering of Highly Luminescent Lanthanide Tags Suitable for Protein Labeling and Time-Resolved Luminescence Imaging. *J. Am. Chem. Soc.* **126**, 4888–4896 (2004).

241. Heffern, M. C., Matosziuk, L. M. & Meade, T. J. Lanthanide Probes for Bioresponsive Imaging. *Chem. Rev.* **114**, 4496–4539 (2014).

242. Melby, L. R., Rose, N. J., Abramson, E. & Caris, J. C. Synthesis and Fluorescence of Some Trivalent Lanthanide Complexes. *J. Am. Chem. Soc.* **86**, 5117–5125 (1964).

243. Hamon, N. *et al.* Synthesis and Photophysical Properties of Lanthanide Pyridinylphosphonic Tacn and Pyclen Derivatives: From Mononuclear Complexes to Supramolecular Heteronuclear Assemblies. *Inorg. Chem.* **62**, 18940–18954 (2023).

244. Akl, D. *et al.* Comprehensive Photophysical and nonlinear Spectroscopic Study of Thioanisolyl-Picolinate Triazacyclononane Lanthanide Complexes. *Eur J Inorg Chem* e202300785 (2024) doi:10.1002/ejic.202300785.

245. Xu, J. *et al.* Octadentate Cages of Tb(III) 2-Hydroxyisophthalamides: A New Standard for Luminescent Lanthanide Labels. *J. Am. Chem. Soc.* **133**, 19900–19910 (2011).

246. Becker, W. Fluorescence lifetime imaging – techniques and applications. *Journal of Microscopy* **247**, 119–136 (2012).

247. Zhang, K. Y. *et al.* Long-Lived Emissive Probes for Time-Resolved Photoluminescence Bioimaging and Biosensing. *Chem. Rev.* **118**, 1770–1839 (2018).

248. Lu, Y. *et al.* Tunable lifetime multiplexing using luminescent nanocrystals. *Nature Photon* **8**, 32–36 (2014).

249. Goetz, J. *et al.* Ultrabright Lanthanide Nanoparticles. *Chempluschem* **81**, 497 (2016).

250. Baggaley, E. *et al.* Long-lived metal complexes open up microsecond lifetime imaging microscopy under multiphoton excitation: from FLIM to PLIM and beyond. *Chem. Sci.* **5**, 879–886 (2014).

251. Gan, C., Zhang, Y., Battaglia, D., Peng, X. & Xiao, M. Fluorescence lifetime of Mn-doped ZnSe quantum dots with size dependence. *Applied Physics Letters* **92**, 241111 (2008).

252. Li, C. & Wu, P. Cu-doped quantum dots: a new class of near-infrared emitting fluorophores for bioanalysis and bioimaging. *Luminescence* **34**, 782–789 (2019).

253. Zhang, R. & Yuan, J. Responsive Metal Complex Probes for Time-Gated Luminescence Biosensing and Imaging. *Acc. Chem. Res.* **53**, 1316–1329 (2020).

254. Zhang, L. *et al.* Living Cell Multilifetime Encoding Based on Lifetime-Tunable Lattice-Strained Quantum Dots. *ACS Appl. Mater. Interfaces* **8**, 13187–13191 (2016).

255. Sun, Y. *et al.* Ultralong lifetime and efficient room temperature phosphorescent carbon dots through multi-confinement structure design. *Nat Commun* **11**, 5591 (2020).

256. Chai, O. J. H., Liu, Z., Chen, T. & Xie, J. Engineering ultrasmall metal nanoclusters for photocatalytic and electrocatalytic applications. *Nanoscale* **11**, 20437–20448 (2019).

257. Sun, S.-K., Wang, H.-F. & Yan, X.-P. Engineering Persistent Luminescence Nanoparticles for Biological Applications: From Biosensing/Bioimaging to Theranostics. *Acc. Chem. Res.* **51**, 1131–1143 (2018).

258. Wild, D. Immunoassay for Beginners. in *The Immunoassay Handbook* 7–10 (Elsevier, 2013). doi:10.1016/B978-0-08-097037-0.00002-6.

259. Kinnamon, D. S., Heggestad, J. T., Liu, J. & Chilkoti, A. Technologies for Frugal and Sensitive Point-of-Care Immunoassays. *Annual Review of Analytical Chemistry* **15**, 123–149 (2022).

260. Ullman, E. F., Schwarzberg, M. & Rubenstein, K. E. Fluorescent excitation transfer immunoassay. A general method for determination of antigens. *J Biol Chem* **251**, 4172–4178 (1976).

261. Nchimi-Nono, K. *et al.* Activated phosphonated trifunctional chelates for highly sensitive lanthanide-based FRET immunoassays applied to total prostate specific antigen detection. *Organic and Biomolecular Chemistry* **11**, 6493–6501 (2013).

262. Hildebrandt, N., Charbonnière, L. J., Beck, M., Ziessel, R. F. & Löhmannsröben, H. Quantum Dots as Efficient Energy Acceptors in a Time-Resolved Fluoroimmunoassay. *Angew Chem Int Ed* **44**, 7612–7615 (2005).

263. Charbonnière, L. J., Hildebrandt, N., Ziessel, R. F. & Löhmannsröben, H. G. Lanthanides to quantum dots resonance energy transfer in time-resolved fluoro-immunoassays and luminescence microscopy. *Journal of the American Chemical Society* **128**, 12800–12809 (2006).

264. Algar, W. R., Kim, H., Medintz, I. L. & Hildebrandt, N. Emerging non-traditional Förster resonance energy transfer configurations with semiconductor quantum dots: Investigations and applications. *Coordination Chemistry Reviews* **263–264**, 65–85 (2014).

265. Mattera, L. *et al.* Compact quantum dot-antibody conjugates for FRET immunoassays with subnanomolar detection limits. *Nanoscale* **8**, 11275–11283 (2016).

266. Bhuckory, S. *et al.* Direct conjugation of antibodies to the ZnS shell of quantum dots for FRET immunoassays with low picomolar detection limits. *Chemical Communications* **52**, 14423–14425 (2016).

267. Annio, G., Jennings, T. L., Tagit, O. & Hildebrandt, N. Sensitivity Enhancement of Förster Resonance Energy Transfer Immunoassays by Multiple Antibody Conjugation on Quantum Dots. *Bioconjugate Chemistry* **29**, 2082–2089 (2018).

268. Su, R. *et al.* A Nanobody-on-Quantum Dot Displacement Assay for Rapid and Sensitive Quantification of the Epidermal Growth Factor Receptor (EGFR). (2022) doi:10.1002/anie.202207797.

269. Croce, A. C. & Bottiroli, G. Autofluorescence spectroscopy and imaging: A tool for biomedical research and diagnosis. *European Journal of Histochemistry* **58**, 320–337 (2014).

270. Tuchin, V. Light scattering study of tissues. *Physics-Uspekhi* **40**, 495 (2007).

271. Pattison, D. I. & Davies, M. J. Actions of ultraviolet light on cellular structures. in *Cancer: Cell Structures, Carcinogens and Genomic Instability* vol. 96 131–157 (Birkhäuser-Verlag, Basel, 2006).

272. Yoon, S. *et al.* Deep optical imaging within complex scattering media. *Nat Rev Phys* **2**, 141–158 (2020).

273. Ximendes, E., Benayas, A., Jaque, D. & Marin, R. Quo Vadis, Nanoparticle-Enabled In Vivo Fluorescence Imaging? *ACS Nano* **15**, 1917–1941 (2021).

274. Wong, K., Bünzli, J. G. & Tanner, P. A. Quantum yield and brightness. *Journal of Luminescence* **224**, 117256 (2020).

275. Genovese, D. *et al.* Energy transfer processes in dye-doped nanostructures yield cooperative and versatile fluorescent probes. *Nanoscale* **6**, 3022–3036 (2014).

276. Rosiuk, V., Runser, A., Klymchenko, A. & Reisch, A. Controlling Size and Fluorescence of Dye-Loaded Polymer Nanoparticles through Polymer Design. *Langmuir* **35**, 7009–7017 (2019).

277. Melnychuk, N., Egloff, S., Runser, A., Reisch, A. & Klymchenko, A. S. Light-Harvesting Nanoparticle Probes for FRET-Based Detection of Oligonucleotides with Single-Molecule Sensitivity. *Angewandte Chemie* **132**, 6878–6885 (2020).

278. Melnychuk, N., Egloff, S., Runser, A., Reisch, A. & Klymchenko, A. S. Light-Harvesting Nanoparticle Probes for FRET-Based Detection of Oligonucleotides with Single-Molecule Sensitivity. *Angewandte Chemie International Edition* **59**, 6811–6818 (2020).

279. Barar, J. Bioimpacts of nanoparticle size: why it matters? *Bioimpacts* **5**, 113–115 (2015).

280. Dolai, J., Mandal, K. & Jana, N. R. Nanoparticle Size Effects in Biomedical Applications. *ACS Appl. Nano Mater.* **4**, 6471–6496 (2021).

281. Egloff, S., Runser, A., Klymchenko, A. & Reisch, A. Size-Dependent Electroporation of Dye-Loaded Polymer Nanoparticles for Efficient and Safe Intracellular Delivery. *Small Methods* **5**, 2000947 (2021).

282. Li, Y. *et al.* Controllable synthesis of gold nanoparticles with ultrasmall size and high monodispersity via continuous supplement of precursor. *Dalton Trans.* **41**, 11725 (2012).

283. Combes, A., Tang, K.-N., Klymchenko, A. S. & Reisch, A. Protein-like particles through nanoprecipitation of mixtures of polymers of opposite charge. *Journal of Colloid and Interface Science* **607**, 1786–1795 (2022).

284. Guevel, X. L. *et al.* Ligand effect on the size, valence state and red/near infrared photoluminescence of bidentate thiol gold nanoclusters. *Nanoscale* **6**, 8091–8099 (2014).

285. Huang, Y., Fuksman, L. & Zheng, J. Luminescence mechanisms of ultrasmall gold nanoparticles. *Dalton Trans.* **47**, 6267–6273 (2018).

286. Hildebrandt, N. & Tagit, O. Colloidal Nanoparticles for Signal Enhancement in Optical Diagnostic Assays. *Journal of Nanoscience and Nanotechnology* **18**, 6671–6679 (2018).

287. Mehta, S. *et al.* Predictive and prognostic molecular markers for cancer medicine. *Ther Adv Med Oncol* **2**, 125–148 (2010).

288. Sahu, P. *et al.* Biomarkers: An Emerging Tool for Diagnosis of a Disease and Drug Development. *Asian Journal of Research in Pharmaceutical Sciences* **1**, 09–16 (2011).

289. Camarca, A. *et al.* Emergent Biosensing Technologies Based on Fluorescence Spectroscopy and Surface Plasmon Resonance. *Sensors* **21**, 906 (2021).

290. Horton, S. *et al.* Delivering modern, high-quality, affordable pathology and laboratory medicine to low-income and middle-income countries: a call to action. *The Lancet* **391**, 1953–1964 (2018).

291. Zhao, M.-X. & Zeng, E.-Z. Application of functional quantum dot nanoparticles as fluorescence probes in cell labeling and tumor diagnostic imaging. *Nanoscale Res Lett* **10**, 171 (2015).

292. Hildebrandt, N., Wegner, K. D. & Algar, W. R. Luminescent terbium complexes : Superior Förster resonance energy transfer donors for flexible and sensitive multiplexed biosensing. *Coordination Chemistry Reviews* **273–274**, 125–138 (2014).

293. Cardoso Dos Santos, M. *et al.* Time-Gated FRET Nanoprobes for Autofluorescence-Free Long-Term In Vivo Imaging of Developing Zebrafish. *Advanced Materials* **32**, (2020).

294. Dekaliuk, M., Qiu, X., Troalen, F., Busson, P. & Hildebrandt, N. Discrimination of the V600E Mutation in BRAF by Rolling Circle Amplification and Förster Resonance Energy Transfer. *ACS Sensors* **4**, 2786–2793 (2019).

295. Chen, C. Lanthanide Energy Transfer Donors on Nanoparticles Surfaces : From Fundamental Mechanisms to Multiplexed Biosensing To cite this version : Lanthanide Energy Transfer Donors on Nanoparticles Surfaces : From Fundamental Mechanisms to Multiplexed Biosensing. *Université Paris- Saclay* (2019).

296. Qiu, X., Guo, J., Xu, J. & Hildebrandt, N. Three-Dimensional FRET Multiplexing for DNA Quantification with Attomolar Detection Limits. *Journal of Physical Chemistry Letters* **9**, 4379–4384 (2018).

297. Qiu, X. *et al.* Nanobodies and antibodies for duplexed EGFR/HER2 immunoassays using terbium-to-quantum dot FRET. *Chemistry of Materials* **28**, 8256–8267 (2016).

298. Lanoë, P.-H. *et al.* Influence of bromine substitution pattern on the singlet oxygen generation efficiency of two-photon absorbing chromophores. *Org. Biomol. Chem.* **10**, 6275 (2012).

299. Mettra, B. *et al.* A combined theoretical and experimental investigation on the influence of the bromine substitution pattern on the photophysics of conjugated organic chromophores. *Phys. Chem. Chem. Phys.* **20**, 3768–3783 (2018).

300. Roovers, R. C. *et al.* Efficient inhibition of EGFR signalling and of tumour growth by antagonistic anti-EGFR Nanobodies. *Cancer Immunol Immunother* **56**, 303–317 (2007).

301. Xiao, M. & Selvin, P. R. Quantum yields of luminescent lanthanide chelates and far-red dyes measured by resonance energy transfer. *Journal of the American Chemical Society* **123**, 7067–7073 (2001).